

WL-TR-94-4011

STRUCTURES OF GRAIN BOUNDARIES AND
ASPECTS OF DEFORMATION BEHAVIOR IN Ni_3Al
ALLOYS

AD-A276 646



RONALD J KERANS

CERAMICS GROUP
MATERIALS DEVELOPMENT BRANCH
METALS AND CERAMICS DIVISION
MATERIALS DIRECTORATE

AUGUST 1988

FINAL REPORT FOR 09/01/83-08/01/88

S DTIC ELECTE D
MAR 08 1994
F

APPROVED FOR PUBLIC RELEASE; DISTRIBUTION IS UNLIMITED.

94-07556



17300

DTIC 17300

MATERIALS DIRECTORATE
WRIGHT LABORATORY
AIR FORCE SYSTEMS COMMAND
WRIGHT PATTERSON AFB OH 45433-7734

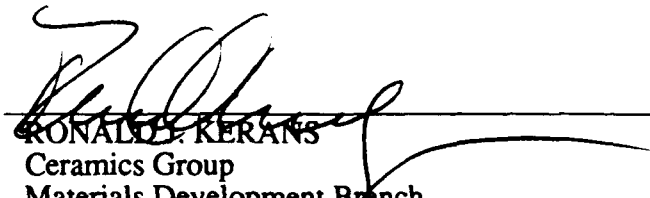
**Best
Available
Copy**


NOTICE

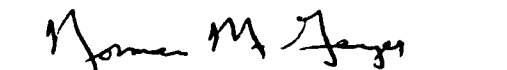
When Government drawings, specifications, or other data are used for any other purpose other than in connection with a definitely Government-related procurement, the United States Government incurs no responsibility or any obligation whatsoever. The fact that the government may have formulated or in any way supplied the said drawings, specifications, or other data, is not to be regarded by implication, or otherwise in any manner construed, as licensing the holder, or any other person or corporation: or as conveying any rights or permission to manufacture, use, or sell any patented invention that may be related thereto.

This report is releasable to the National Technical Information Service (NTIS). At NTIS, it will be available to the general public, including foreign nations.

This technical report has been reviewed and is approved for publication.


RONALD J. KERANS
Ceramics Group
Materials Development Branch
Metals and Ceramics Division


GERALD J. PETRAK, Acting Chief
Materials Development Branch
Metals and Ceramics Division


NORMAN M. GEYER, Acting Chief
Metals and Ceramics Division
Materials Directorate

If your address has changed, if you wish to be removed from our mailing list, or if the addressee is no longer employed by your organization please notify WL/MLLN Bldg 655, 2230 Tenth St Ste 1, WPAFB, OH 45433-7817 to help us maintain a current mailing list.

Copies of this report should not be returned unless return is required by security considerations, contractual obligations, or notice on a specific document.

REPORT DOCUMENTATION PAGE

Form Approved
OMB No. 0704-0188

Public reporting burden for this collection of information is estimated to average 1 hour per response, including the time for reviewing instructions, searching existing data sources, gathering and maintaining the data needed, and completing and reviewing the collection of information. Send comments regarding this burden estimate or any other aspect of this collection of information, including suggestions for reducing this burden, to Washington Headquarters Services, Directorate for Information Operations and Reports, 1215 Jefferson Davis Highway, Suite 1204, Arlington, VA 22202-4302, and to the Office of Management and Budget, Paperwork Reduction Project (0704-0188), Washington, DC 20503

1. AGENCY USE ONLY (Leave blank)		2. REPORT DATE August 1988	3. REPORT TYPE AND DATES COVERED Final 9/83 - 8/88	
4. TITLE AND SUBTITLE Structures of Grain Boundaries and Aspects of Deformation Behavior in Ni ₃ Al ALLOYS			5. FUNDING NUMBERS 2306P801 61102F	
6. AUTHOR(S) Ronald J. Kerans				
7. PERFORMING ORGANIZATION NAME(S) AND ADDRESS(ES) Wright Laboratory Materials Development Branch Ceramic Group, Wright Patterson AFB OH 45433-7817 The Ohio State University 119 W. 19th St. Columbus OH 43210			8. PERFORMING ORGANIZATION REPORT NUMBER WL-TR-94-4011	
9. SPONSORING/MONITORING AGENCY NAME(S) AND ADDRESS(ES) WL/MLLM BLDG 655 2230 Tenth St Ste 1 Wright-Patterson AFB, OH 45433-7817			10. SPONSORING/MONITORING AGENCY REPORT NUMBER WL-TR-94-4011	
11. SUPPLEMENTARY NOTES Dissertation presented in partial fulfillment of the Requirements for the Degree Doctor of Philosophy in the Graduate School of the Ohio State University.				
12a. DISTRIBUTION/AVAILABILITY STATEMENT APPROVED FOR PUBLIC RELEASE: DISTRIBUTION IS UNLIMITED.			12b. DISTRIBUTION CODE	
13. ABSTRACT (Maximum 200 words) The structures of two grain boundaries in Ni ₃ Al were determined using transmission electron microscopy (TEM). The line directions and spacings of secondary grain boundary dislocation (gbds) were calculated for coincidence site lattice (CSL) relationships near the experimentally determined misorientations. The structures of the boundaries were found to be in good agreement with $\Sigma 9$ and $\Sigma 31b$ relationships of the ordered lattice. The grain boundary dislocations were found to be characteristic of the ordered structure. No grouping of partial gbds was observed. Lattice dislocations consisting of pairs of 1/3 [112] superpartials bounding extended superlattice intrinsic stacking faults (SISFs) were observed by TEM. They were found to independently react to APB coupled 1/2 [110] pairs in the commonly observed pure screw orientation. Implications with regard to Kear-Wiltsdorf type locking mechanisms and deformation behavior are discussed. Boron was observed to have strong effects upon the population of boundary types, grain size, and grain growth. In addition, small amounts of B completely eliminate widely extended stacking faults. It is concluded that effects of B other than influencing boundary cohesion are important.				
14. SUBJECT TERMS			15. NUMBER OF PAGES 171	
			16. PRICE CODE	
17. SECURITY CLASSIFICATION OF REPORT UNCLASSIFIED	18. SECURITY CLASSIFICATION OF THIS PAGE UNCLASSIFIED	19. SECURITY CLASSIFICATION OF ABSTRACT UNCLASSIFIED	20. LIMITATION OF ABSTRACT UL	

DEDICATION

To my grandmother, Dorothy A. Moore Hancock, who is a model of stoic determination; and to the memory of my grandfather, James Robertson Kerans, who was poor and uneducated by usual standards, but wealthy and wise in the things that matter most. They have been inspirations to their families and friends.

ACKNOWLEDGMENTS

I extend my appreciation to Dr. John P. Hirth for his guidance and encouragement, and for the example set by his thoughtful and open-minded approach to new ideas. My appreciation also goes to Dr. William A. T. Clark for his advice and guidance in the grain boundary portion of this work. Thanks also to Dr. G. Meyrick for his helpful suggestions. For careful manuscript preparation, the efforts of H. L. Henrich are much appreciated. The technical assistance of G. Cornish, J. Henry, T. Campbell, R. Sweeney, C. Heidenrich and J. Payne are gratefully acknowledged. For support and encouragement during this work, I thank B. E. Kerans, B. L. Kerans and Dr. H. C. Graham. My thanks go to R. M. Hamilton for both support and assistance with the manuscript. Finally, I want to thank my daughter Jessica for her patience, understanding and support throughout this work.

Accession For	
NTIS CRA&I	<input checked="" type="checkbox"/>
DTIC TAB	<input type="checkbox"/>
Unannounced	<input type="checkbox"/>
Justification	
By	
Distribution/	
Availability Codes	
Dist	Avail and/or Special
A-1	

VITA

November 27, 1946..... Born - Paris, Illinois

1966-1969..... US Army, Radar and Computer Technician

1975..... B.S., Physics, Wright State University, Dayton, Ohio

1977..... M.S., Physics, Wright State University, Dayton, Ohio

1977-1986..... Materials Research Engineer, Air Force Wright Aeronautical Materials Laboratory, Wright-Patterson AFB, Ohio

1978-1980..... Adjunct Professor, Wright State University, Dayton, Ohio

1984..... M.S., Metallurgical Engineering, The Ohio State University, Columbus, Ohio

1986-Present..... Group Leader, High Temperature Composites Research Group, Air Force Wright Aeronautical Materials Laboratory, Wright-Patterson AFB, Ohio

PUBLICATIONS

R. J. Kerans, "Amplitude Dependence of Dislocation Damping After Quenching and During Electron Irradiation," M.S. Thesis, Wright State University, 1977.

R. J. Kerans and H. M. Simpson, "Amplitude Dependence of Dislocations Damping in High-Purity Copper after Quenching and During 1-MeV Electron Irradiation," J. Appl. Phys. 50, 4739 (1979).

R. J. Kerans, K. S. Mazdidasni, R. Ruh, and H. A. Lipsitt, "Solubility of Metals in Substoichiometric TiC_{1-x} ," J. Am. Ceram. Soc. 67, 34-38 (1984).

R. J. Kerans, "Deformation in Ti_3Al Fatigued at Room and Elevated Temperatures," Metall. Trans. A, 15A, 1721-29 (1984).

R. J. Kerans and K. T. Faber, "Low Thermal Expansion Coatings for Carbon-Carbon Composites," NASA-CP-2482, 409-25 (1987).

E. E. Hermes and R. J. Kerans, "Degradation of Nonoxide Reinforcement and Oxide Matrix Composites," MRS Symposium Proceedings, 125, Materials Stability and Environmental Degradation, MRS, Pittsburgh, PA, 1988, to be published.

R. J. Kerans, "Dependence of Composite Properties upon Statistical Variations in Fiber Loading and Properties," Ceramic Engineering and Science Proceedings, 9, Am. Ceram. Soc. Westerville, Ohio, 1988, to be published.

A. P. Katz and R. J. Kerans, "The Structural Ceramics Program at the Air Force Wright Aeronautical Laboratories, Materials Laboratory," Am. Ceram. Soc. Bull. 67, 1360 (1988).

K. Cho, R. J. Kerans, and K. A. Jepsen, "Processing and Properties of SiC Monofilament Reinforced Glass Composites," Ceramic Engineering and Science Proceedings, 9, Am. Ceram. Soc. Westerville, Ohio, 1988, to be published.

FIELDS OF STUDY

Major Field: Metallurgical Engineering

Studies in Metallurgical Engineering (John P. Hirth and William A. T. Clark)

TABLE OF CONTENTS

DEDICATION.....		ii
ACKNOWLEDGMENTS.....		iii
VITA.....		iv
LIST OF FIGURES.....		ix
LIST OF TABLES		xiii
CHAPTER		PAGE
I	INTRODUCTION.....	1
	1.1 Objectives.....	1
	1.2 Ordered Alloys: Ni ₃ Al.....	3
II	GRAIN BOUNDARY STRUCTURE: BACKGROUND AND THEORY.....	13
	2.1 Background.....	13
	2.1.1 Structure and Properties.....	13
	2.1.2 Boundaries in Ni ₃ Al.....	14
	2.2 The DSC Lattice Model of Boundary Structure.....	16
	2.3 Calculation of DSC Vectors.....	27
	2.4 Boundaries in Ordered Material.....	28
III	GRAIN BOUNDARY STRUCTURE: EXPERIMENT.....	35
	3.1 Experimental Procedure.....	35
	3.1.1 Sample Preparation.....	35
	3.1.2 Approximate Misorientation from Stereographic Projection.....	37
	3.1.3 More Precise Determination of Misorientation.....	38
	3.1.4 Determination of Boundary Plane.....	44
	3.1.5 Solution for Boundary Structure.....	54
	3.2 Boundary 1, $\Sigma = 31$	54
	3.3 Grain Boundary 2, $\Sigma = 9$	67
IV	DEFORMATION IN Ni ₃ Al: BACKGROUND AND THEORY.....	83
V	DEFORMATION IN Ni ₃ Al: EXPERIMENT.....	88

5.1	Experimental Procedures.....	88
5.1.1	Specimen Preparation.....	88
5.1.2	Fault Analysis and the Magnitude of 112 Burgers Vectors.....	88
5.1.3	Annealing Twins, Grain Size and Chemistry.	89
5.2	Results.....	90
5.2.1	Frequency of Annealing Twins and Grain Size.....	90
5.2.2	Dislocations and Stacking Faults.....	93
VI	DISCUSSION.....	134
6.1	Grain Boundary Structure.....	134
6.2	Surface Energies and Grain Boundary Population..	137
6.3	Possible Effects of Segregants Upon Slip Transmittal and Grain-Boundary Sources.....	139
6.4	The Role of SISF Coupled Dislocations.....	146
VII	CONCLUSIONS.....	151
	LIST OF REFERENCES.....	153

LIST OF FIGURES

FIGURE		PAGE
1	Unit cell of Ni_3Al . Open circles-Al, closed-Ni $1/2 [101]$ and $[011]$ vectors shown.....	4
2	Two dimensional structure with APB's, indicated by lines, and 3 superpartials two of which are paired as a superdislocation.....	5
3	Important faults in Ni_3Al . Large circles one plane above, small circles one plane below. Closed Al, open Ni. a) $L1_2$, b) APB resulting from translation of upper plane of $1/2 [\bar{1}01]$ c) SISF resulting from translation of $1/3 [\bar{2}11]$ d) CSF resulting from translation of $1/6[\bar{1}\bar{1}2]$	8
4	APB coupled superdislocation.....	9
5	SISF coupled superdislocation.....	10
6	Shockley partial dislocation loop transforms APB to SISF coupled dislocation.....	12
7	fcc crystals in $\Sigma 9$ CSL relationship. Closed figures crystal 1. Triangles one plane out of page.....	18
8	Low angle tilt boundaries. a) One Burgers vector. b) Two different Burgers vectors.....	20
9	a) Grain boundary dislocation of the disordered (fc) structure in an ordered $\Sigma 11$ boundary between crystals of the $L1_2$ structure. Anti-coincident region to the right. b) Dislocation of the ordered boundary (twice the magnitude in a) preserve the structure.....	30
10	DSC vectors of the ordered and disordered $\Sigma 3$ CSL.....	33
11	DSC vectors of the ordered and disordered $\Sigma 5$ CSL in an $L1_2$ structure.....	34
12	Misorientation determination from near-colinear zone axes.	41

FIGURE	PAGE
13	Line features p, q in boundary projected on TEM plate from two different orientations of the boundary..... 45
14	Determination of transformation for gb normal..... 47
15	Schematic of grain boundary 1..... 56
16	Bright-field (BF) micrograph of boundary 1. Set A visible..... 57
17	BF micrograph, gb 1. Set A visible..... 58
18	Dark-field (DF) micrograph, gb 1. Set A and B visible.... 59
19	DF micrograph, boundary 1. Set B visible..... 60
20	BF micrograph, boundary 1. Dislocation emission or absorption..... 61
21	BF micrograph, boundary 2. Set A visible..... 68
22	Schematic diagram of boundary 2..... 69
23	BF micrograph, boundary 2. Set A visible..... 70
24	BF micrograph, boundary 2. Set A visible..... 71
25	BF micrograph. Set A visible..... 72
26	Weak-beam dark-field (WB) micrograph of boundary 2. Set A visible..... 73
27	DF micrograph of boundary 2. Set C visible..... 74
28	Grain structure in Ni-24.5 Al with and without B..... 91
29	Effect of B on twin frequency and grain size..... 92
30	Typical SISF coupled pairs..... 95
31	Typical SISF coupled pairs..... 96
32	Typical extended SISF..... 97
33	High density of extended faults and SISF debris..... 98

FIGURE	PAGE
34	Extended SISF..... 99
35	Bounding dislocations visible, fault invisible..... 100
36	One bounding dislocation invisible..... 101
37	The second bounding dislocation invisible..... 102
38	Schematic of extended fault 1..... 103
39	WB image of extended fault 1..... 104
40	Extended fault 2..... 107
41	Fault 2 invisible..... 108
42	WB, fault 2 invisible..... 109
43	One bounding dislocation invisible..... 110
44	The second bounding dislocation invisible..... 111
45	Undissociated superdislocation invisible..... 112
46	Schematic of fault 2 and lozenge (L)..... 113
47	$\pm \underline{g}$ images of SF2..... 114
48	WB image of lozenge..... 116
49	WB image of lozenge..... 117
50	Lozenge disociation of superdipole in Thompson notation.. 118
51	Lozenge disociation of superdipole..... 119
52	Faint dislocation line - like contrast in some fundamental reflections arrow..... 120
53	Faint residual fault contrast in region bounded by A, B an imaginary extension of C and the foil surface..... 124
54	Extended fault 3..... 125

FIGURE		PAGE
55	Schematic of extended fault 3.....	126
56	WB image, fault invisible.....	127
57	One bounding dislocation invisible.....	128
58	Second bounding dislocation invisible.....	129
59	\pm g images of SF3.....	130
60	Region of high density of SISFs.....	131
61	Faults and some dislocations invisible.....	132
62	Faults and some dislocations invisible.....	133
63	Slip transmittal. a) localized. b) diffuse.....	140
64	Emission of superdislocation.....	142
65	Emission of superdislocation.....	145
66	Kear-Wiltsdorf lock as source of SISF, $1/3(112)$ superdislocation.....	148

LIST OF TABLES

TABLE		PAGE
1.	Selected CSL Lattices for $\Sigma > 49$	29
2.	Typical Chemical Analysis.....	36
3.	$\Sigma = 31b$ DSC Vectors.....	63
4.	Characteristics of Grain Boundary 1, $\Sigma = 31b$	64
5.	Summary of $\underline{g \cdot b}$ Analyses, Grain Boundary 1.....	65
6.	Possible Misorientations of Grain Boundary 2.....	75
7.	$\Sigma = 9$ DSC Vectors.....	76
8.	$\Sigma = 57c$ DSC Vectors.....	77
9.	$\Sigma = 59b$ DSC Vectors.....	78
10.	Possible Dislocations Sets, Grain Boundary 2.....	80
11.	Summary of $\underline{g \cdot b}$ Analysis.....	81
12.	Summary of $\underline{g \cdot b}$ Analysis, SF1.....	94
13.	Summary of $\underline{g \cdot b}$ Analysis, SF2.....	106
14.	Summary of $\underline{g \cdot b}$ Analysis, Lozenge.....	115
15.	Summary of $\underline{g \cdot b}$ Analysis, SF3.....	123

CHAPTER I
INTRODUCTION

1.1 Objectives

Alloys based on the intermetallic compounds have many potentially attractive properties for structural use at high temperatures. These include high stiffness and strength, low density, and oxidation resistance. There are also a number of interesting consequences of their ordered nature which make them interesting and fruitful subjects of research. For example, the character and deformation behavior of lattice dislocations are subject to more rigorous constraints, and are more complex, than in disordered materials. It is probable that ordering also affects the structure and deformation of grain boundaries but this is a question which has received little attention from a fundamental viewpoint.

These are issues of practical importance as well, since most intermetallics are brittle to the point of being unusable. In most systems, that is a difficult property to moderate. However, one of the factors motivating the continuing interest in Ni_3Al is the remarkable effect of boron on ductility. Small amounts of B can increase

the strain-to-failure from zero to over 30% and is clearly related to grain boundary behavior.

Another factor is the scientific interest excited by the anomalously increasing yield strength with increasing temperature demonstrated by Ni_3Al and some other L1_2 structured compounds. It is this behavior which is in large part responsible for the remarkable properties of Ni-based superalloys, in many of which, Ni_3Al is the major phase. These materials are of major technological importance.

The general objective of this work was to investigate the question of grain boundary structure in ordered alloys. Specifically, the goal was to determine the structure of one or more boundaries in Ni_3Al and identify in what ways the ordered nature affects the boundary structure, e.g., whether the structure is characteristic of the ordered lattice or the disordered lattice. Early in the study, it became evident that there were aspects of lattice dislocation behavior which had not been adequately addressed in the literature and which clearly had the potential for affecting deformation behavior at grain boundaries, and hence, apparent grain boundary behavior. Consequently, a parallel study on aspects of the character of certain configurations of lattice dislocations was performed. In addition, the effects of B on Ni_3Al are so pronounced they may provide additional insight into fundamental issues. Therefore, B containing alloys were made and investigated, although in a more cursory manner. Notable differences between the two types of materials are noted and some effects of B are discussed.

Following a brief overview of ordered alloys, the two topics (grain boundaries and lattice dislocations) are treated separately with the grain boundary work in Chapters II and III, and lattice dislocations in Chapters IV and V. The implications of the findings and the relationship of the two areas of investigation are considered in Chapter V, with summary and conclusions in Chapter VI.

1.2 Ordered Alloys: Ni_3Al

Ni_3Al is of the L1_2 structure, which may be thought of as face-centered cubic with Al atoms at the cube corners and Ni atoms at the face center position (Fig. 1). An equivalent description is that of four interpenetrating cubic lattices, one of which is Al and three are Ni. More properly it is primitive cubic with four atoms per lattice point. Because the ordering process can originate at more than one point, a single grain can contain equivalent domains which differ only by choice of origin (Fig. 2). The domains are separated by interfaces called Anti-Phase Boundaries (APB). Atomic neighbors are mismatched by type across the boundary, therefore, it is a higher energy configuration. The APB energy is dependent upon the magnitude of the ordering energy and upon the plane of the boundary, i.e., the types and distances of mismatched bonds. Ni_3Al is ordered to the melting point: consequently thermal APBs can only be retained by rapid solidification. The Burgers vectors of perfect dislocations (those whose passage leaves the crystal structure unaltered) are translation vectors

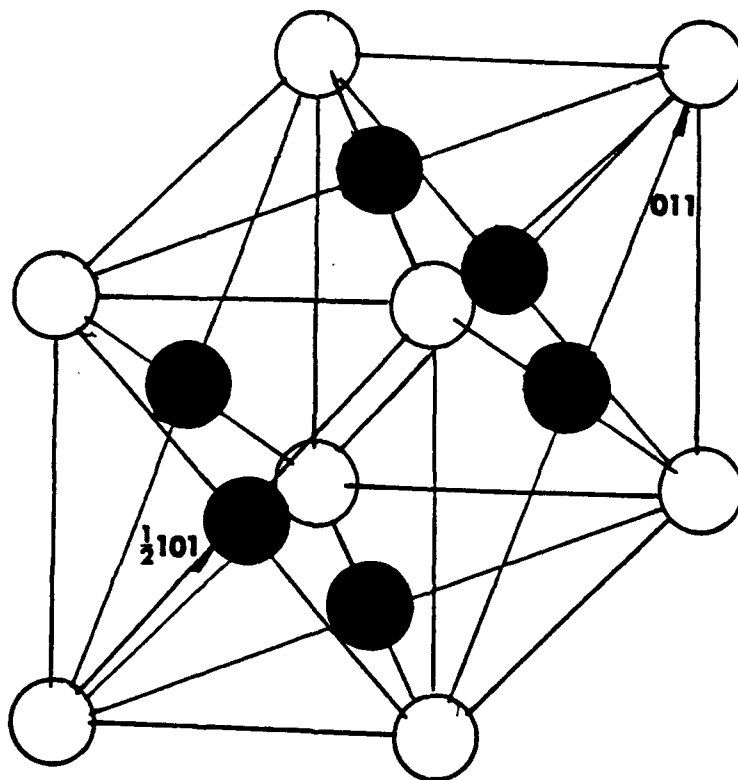


FIGURE 1. Unit cell of Ni₃Al. Open circles-Al, closed-Ni, $\frac{1}{2}[101]$ and $[011]$ vectors shown.

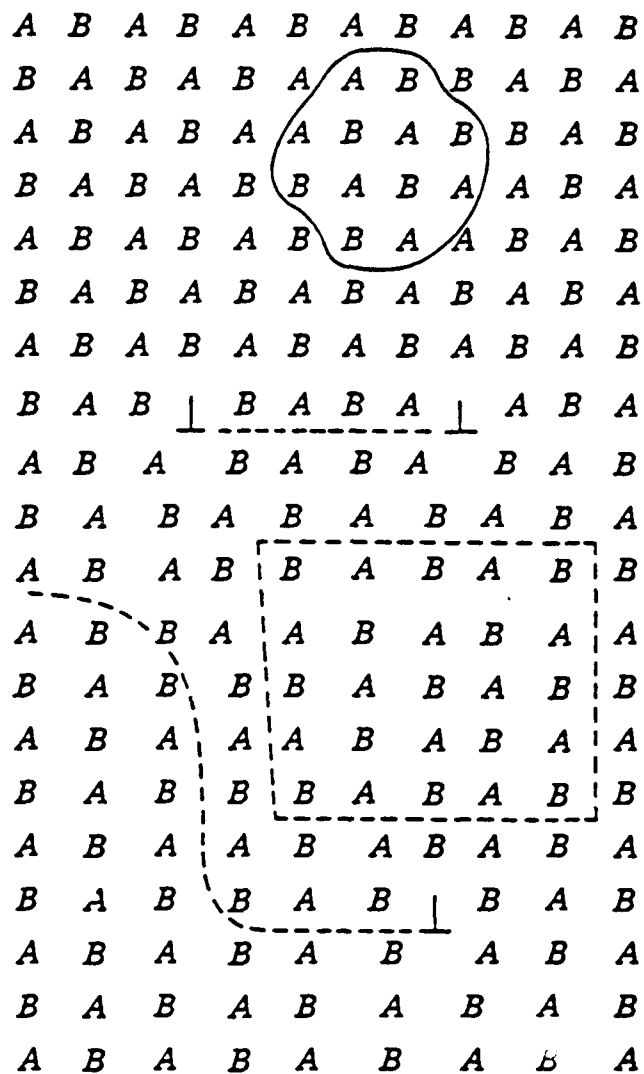


FIGURE 2. Two dimensional structure with APB's, indicated by lines, and 3 superpartials two of which are paired as a superdislocation. (11)

of the ordered lattice and are usually double the length of those in the disordered crystal (Figs. 1 and 2).^{1,2}

While the structure of the disordered crystal is completely described by one lattice, and that of the ordered crystal is completely described by a different lattice, the terminology and viewpoint often employed are based upon the disordered lattice. This is partly due to consideration of the transformation from the disordered state to the ordered state. All atom sites are the same before and after ordering. Whereas prior to ordering, A and B, atoms were randomly distributed on all sites, after ordering they are segregated to particular subsets of the same sites. In a sense, the order is overlaid upon the disordered lattice. The disordered lattice is often called the fundamental lattice and the ordered lattice is called the superlattice. Dislocations of the ordered lattice are called superdislocations.

A more rigorous terminology is to refer to the ordered and disordered lattices and perfect dislocations in each. However, when the ordering energy is relatively low, some phenomena in the ordered structure are more easily visualized and explained from the basis of the disordered (fundamental) lattice. It is also usually true that the operative slip systems in ordered alloys are not the close-packed directions and planes of the ordered lattice. Hence the persistence, and utility, of the superlattice terminology. Both sets of terms will be used here.

The strain energy of a dislocation in either lattice decreases if it splits into two partial dislocations. They are separated by a planar fault however, and the fault energy must be sufficiently low that the creation of the fault requires less energy than the strain energy liberated by separating the partials. There have been reported observations of several different dislocation and fault configurations.^{1,3-6} However, the more complicated arrangements involving extrinsic faults occasionally observed in γ - γ' alloys⁵ have not been reported in single phase Ni_3Al . The three important faults are the APB, the superlattice intrinsic stacking fault (SISF), and the complex stacking fault (CSF) [Fig. 3(a)]. Across the APB,² the stacking is correct but the order is wrong. Across the SISF, which is the intrinsic stacking fault of the ordered lattice, the stacking is wrong but the order is correct. The CSF is the intrinsic stacking fault of the disordered lattice and has both incorrect order and stacking. The SISF is the lowest energy fault, the APB next, and the CSF is highest. If the fault energy is low, the separation between super-partial may be quite large^{7,8} and the dislocations are nearly independent. It is in such a case that it is advantageous to consider the disordered (fundamental) lattice as the basis. In Ni_3Al , the relevant perfect dislocation is a $\langle 110 \rangle$ which can split into either $a/2\langle 110 \rangle$ or $a/3\langle 112 \rangle$ superpartials as in Figs. 4 and 5. The superpartials can further split into Shockley partials, as shown. In principal, it is possible to convert one pair of superpartials into the other by adding opposite Shockley partials to each superpartial, as in the reaction of

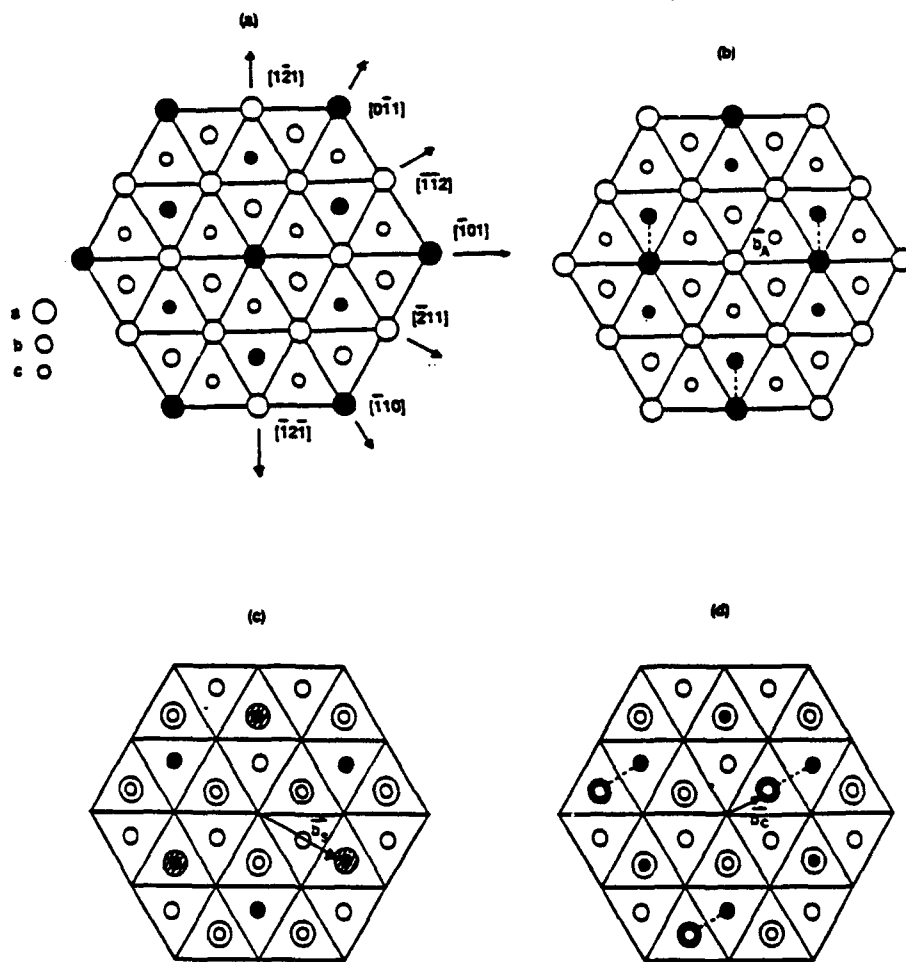


FIGURE 3. Important faults in Ni_3Al . Large circles one plane above, small circles one plane below. Closed Al, open Ni. a) L1_2 b) APB resulting from translation of upper plane of $1/2 [\bar{1}01]$ c) SISF resulting from translation of $1/3 [\bar{2}11]$ d) CSF resulting from translation of $1/6 [\bar{1}\bar{1}2]$ (after 66)

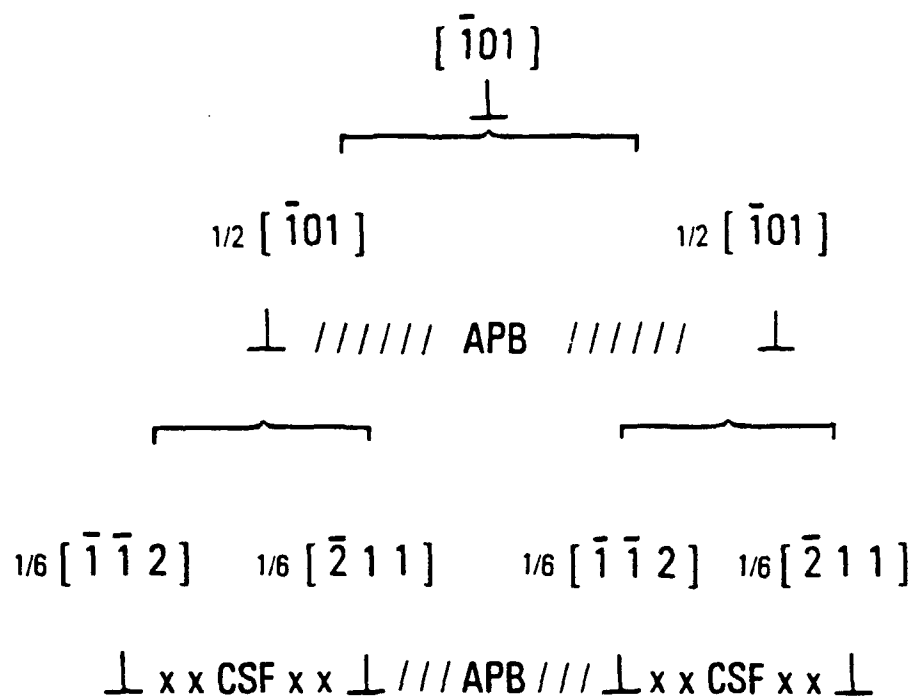


FIGURE 4. APB coupled superdislocation.

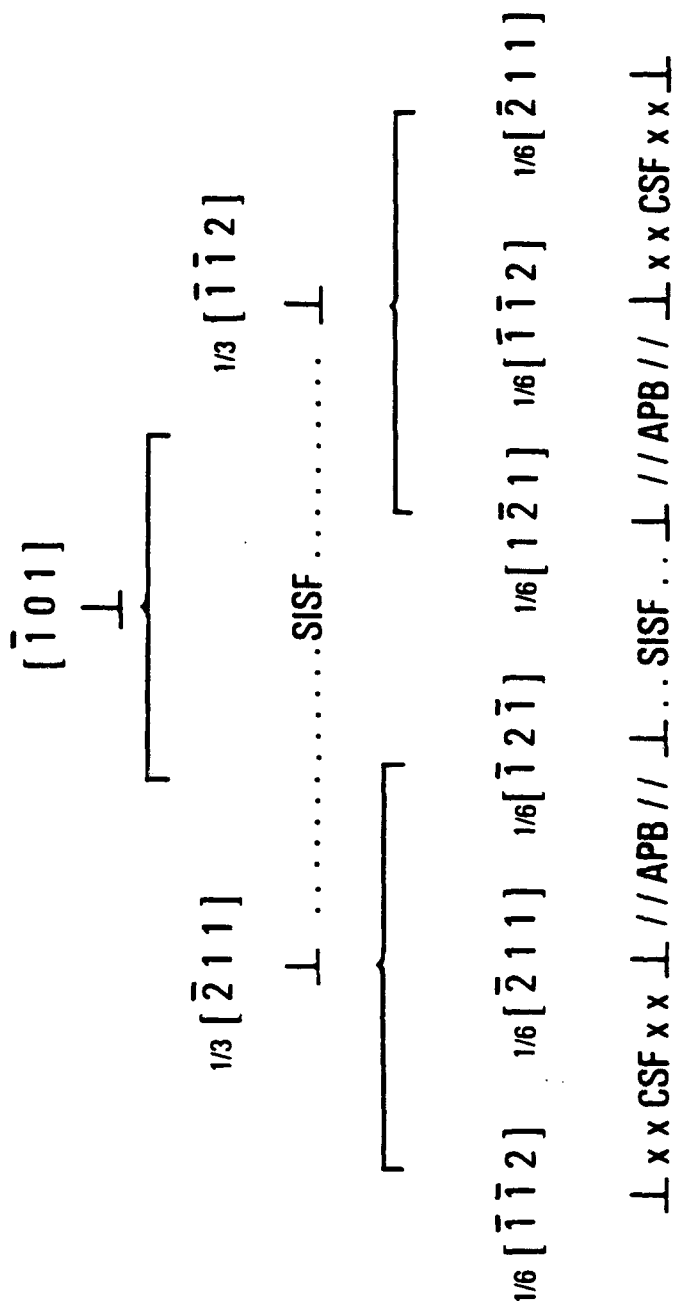


FIGURE 5. SISF coupled superdislocation.

Fig. 6. Such a reaction could occur through the nucleation of a loop of Shockley partial in the faulted region between superpartials. Effects of ordering on grain boundaries are discussed in Chapter II.

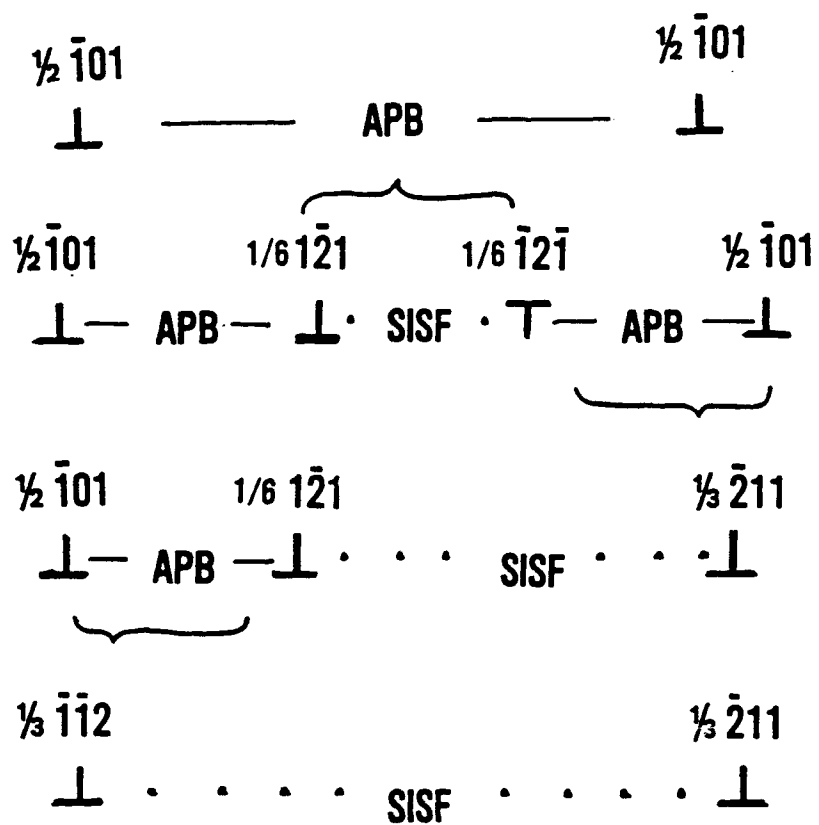


FIGURE 6. Shockley partial dislocation loop transforms APB to SISF coupled dislocation.

CHAPTER II

GRAIN BOUNDARY STRUCTURE: BACKGROUND AND THEORY

2.1 Background

2.1.1 Structure and Properties

It has long been recognized that grain boundaries can play a significant role in the deformation behavior of metals and that they behave differently than the bulk crystal. Macroscopic issues such as dependences of properties of polycrystals upon grain size, concentration of deformation in boundaries at very high temperatures, grain boundary embrittlement and grain boundary diffusion are among boundary related phenomena well known for many years.^{9,10} Recent years have brought an appreciation of macroscopic issues related to elastic and plastic compatibility and slip transmission through grain boundaries.¹¹

For many years, boundaries were thought to consist of thin layers of amorphous cement which bond the crystallite grains together.⁹ By 1950, dislocation models of boundary structure began to appear,^{10,11} and in 1955, a treatment utilizing a continuous surface of dislocations was introduced.^{11,12} By this time, the power of the electron

microscope was beginning to contribute to the foundations established by elegant, but low-resolution, etch-pit and decoration techniques.¹⁰

In the late 60's and early 70's there occurred both increasing interest in the role of boundaries, particularly as sources and sinks for lattice dislocations,¹³⁻¹⁵ and the development of an analytical model of boundary structure.¹⁶ Bollmann's O-lattice theory was based upon descriptions of low-angle boundaries and the Coincident Site Lattice (CSL) model of boundary structure.¹⁷ The approach has been refined and interpreted by numerous investigators,¹⁸⁻²³ and has been utilized successfully in transmission electron microscope studies of boundary structure.²⁴⁻²⁷

X-ray diffraction experiments²⁸ and calculated boundary structures²⁹⁻³⁶ indicate that boundaries can undergo significant relaxation from an ideal CSL arrangement. Individual atoms relax to new positions and the crystals may translate both along the interface and normal to it. As a consequence the CSL model should not be expected to provide a rigorous model of the actual structure of the boundary. However, the model is well accepted as providing an accurate description of the periodic nature of the boundary and of the Burgers vectors of interfacial dislocations.³⁷

2.1.2 Boundaries in Ni₃Al

Notable reported experimental findings in Ni₃Al that relate particularly to grain boundary behavior include: 1. Single crystals of

Ni_3Al are ductile at all temperatures.³⁸ 2. Polycrystals are brittle except at quite high temperatures and fail intergranularly.^{39,40} 3. Small amounts (< 1%) of B increase the ductility of Ni-rich polycrystals to > 10%.⁴¹ 4. The magnitude of the B effect upon ductility decreases with increasing Al to no effect in slightly Al-rich compositions.⁴²

In many cases, grain boundaries play key roles in yield behavior. Sometimes the role is a second-order effect such as slip incompatibility at boundaries due to an insufficient number of slip systems.⁴³ In other instances it is a first-order effect such as interfering with slip transmittal or having low cohesive strength, as has been thought in the case of Ni_3Al .⁴² The discovery by Aoki and Izumi that 0.5 at.% B increased the room-temperature tensile ductility of Ni_3Al from 0 to over 30% has been principally responsible for the recent interest in the compound.⁴¹ Until very recently, the effect has generally been attributed entirely to increased grain boundary cohesion. However, Baker, Schulson and Horton⁴⁴ have suggested that B affects slip transmittal and suggest that the boundaries disorder. Several calculations on the effects of B and other segregants on boundary energy in several systems support the case for increased cohesion.⁴⁵⁻⁴⁸ These have indicated that the principal effect of B is to increase the Ni-Ni bond strength. Several experimental studies have been done on the chemistry of boundaries confirming preferential segregation of B to boundary rather than free surfaces.⁴⁹⁻⁵¹

The structure of boundaries in ordered alloys has been considered by Clark and Pond⁵² and others⁵³⁻⁵⁶ and will be discussed somewhat more below. Chen, Voter, and Srolovitz⁵⁵ have performed an atomistic simulation for $\langle 100 \rangle$ tilt boundaries in Ni_3Al and Foiles⁵⁷ has calculated $\langle 100 \rangle$ twist and tilt boundaries using the embedded atom approach. Both have found Ni-rich boundaries to be of lower energy than stoichiometric or Al-rich boundaries. Foiles has found that for off-stoichiometric compositions the boundaries act as sinks for the excess species. Miller and Horton have studied segregation using atom probe field ion microscopy and found B segregated more strongly to high-angle than to $\Sigma = 3$ boundaries. They also observed segregation to APB's.⁵⁸ Sieloff, et al. utilizing the same technique, concur, and add that no disorder of the crystals at the boundary is observed.⁵⁹ Baker and Schulson have observed by AEM the effect of B on the concentration of Al in the grain boundaries.⁶⁰ They found that B enhances the depletion of Al from the boundary.

2.2 The DSC Lattice Model of Boundary Structure

The discussion here follows in part Smith and Pond,¹⁹ Clark and Pond⁵² and Grimmer, Bollman, and Warrington.^{18,61} In the most basic form, the model is quite simple. It is assumed that: 1. The boundary is infinitesimal in width--all atoms on one side of a planar boundary occupy sites of that crystal, and 2. The lowest energy boundary structures are postulated to be those in which the greatest numbers of

interfacial atoms occupy positions belonging to both lattices, i.e., coincidence sites.

Since all the atoms occupy sites of one or the other crystal, all possibilities are included by consideration of two interpenetrating lattices differing by a pure rotation. Only certain rotations result in a high density of coincident sites, however, and these are assumed to be favored. If the rotation is a coincidence orientation, there can be constructed a three dimensional lattice of coincident sites (Fig. 7). The ratio of the volume of the CSL unit cell to the crystal unit cell is also the ratio of CSL sites to lattice sites and is usually labeled Σ . Σ does not necessarily imply a unique rotation, i.e., two or more different CSL's may yield the same Σ . Conceptually then, the bicrystal is constructed by choosing the boundary plane then placing atoms on lattice 1 on one side of the plane and on lattice 2 on the other side. Boundary planes which include high areal densities of coincidence sites are taken to be preferred. However, an apparently arbitrary plane might be made up of strain-free microfacets along high CS density planes.

A slight misorientation from the exact CSL rotation may be thought of as a distortion of the CSL at the boundary exactly analogous to the distortion of crystal lattice planes at a low-angle boundary. It is observed that in low-angle boundaries, the distortion "condenses" to discrete areas of high distortion -- dislocations-- separated by regions of low distortion wherein the lattice structure is preserved. The lowest energy configuration consists of an array of

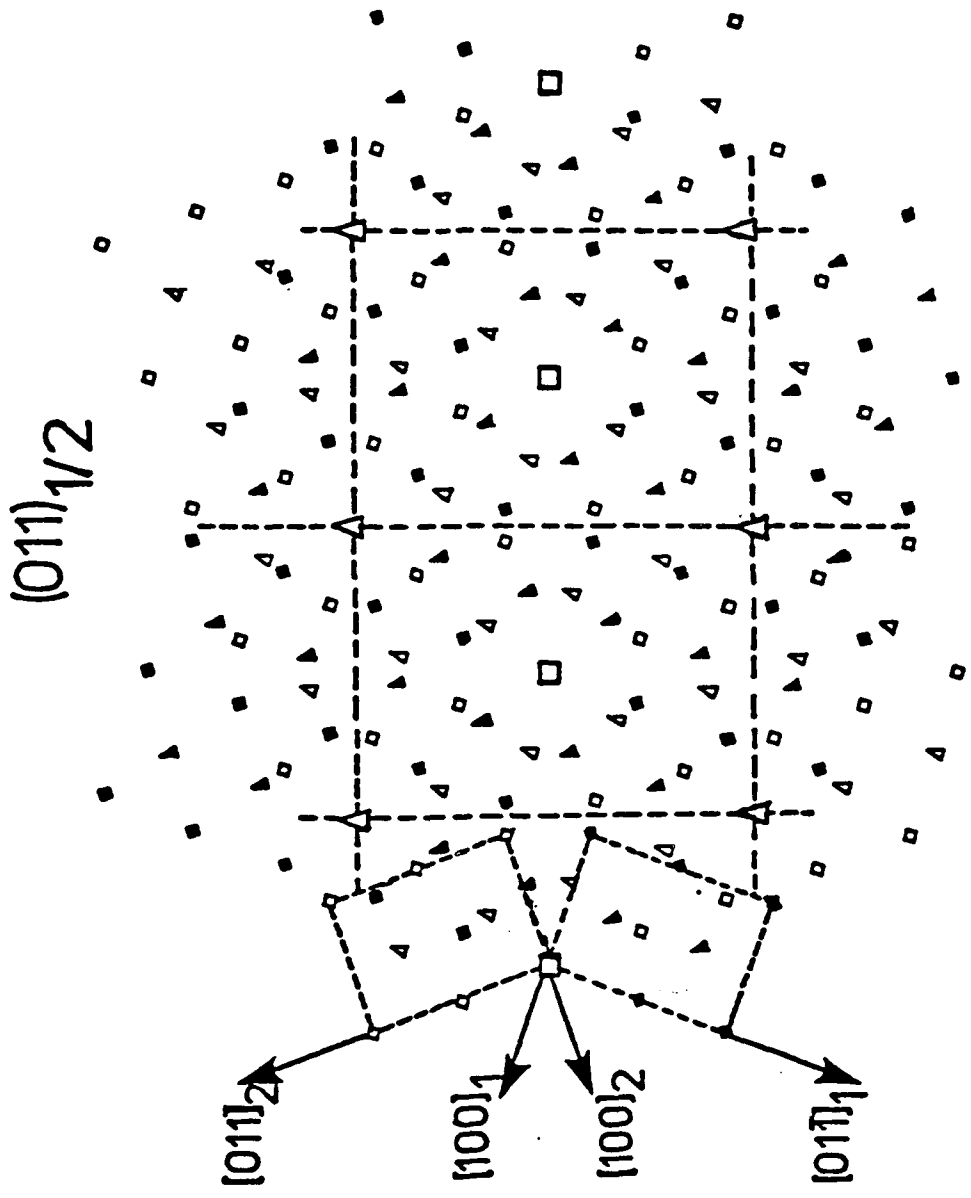


FIGURE 7. fcc crystals in $\Sigma 9$ CSL relationship. Closed figures crystal 1. Triangles one plane out of page. (61)

discrete translations of the crystal lattice, i.e., perfect lattice dislocations. Low-angle boundaries consisting of arrays of a single Burgers vector (a), and two different Burgers vectors (b) are shown in Fig. 8. The boundary model is based upon extension of the analogy to the condensation of distortion of the CSL to an array of dislocations such that the CSL structure is preserved between them. These grain boundary dislocations, gbds, are not lattice dislocations but are characteristic of each CSL.

Translation vectors of the structure formed by the two interpenetrating lattices must be translation vectors of either lattice, or vectors which connect sites of the two lattices. Only such vectors preserve the structure. The latter are the difference vectors between translation vectors (not necessarily equivalent) of the two sublattices.

$$d = t_2 - t_1 \quad 2.1$$

Where t_2 and t_1 are translation vectors in the respective sublattices. The three smallest magnitude non-coplaner differences form a basis of the DSC lattice. The term DSC stands for "Displacement-Shift-Complete", a reference to the fact that the DSC vectors are the shortest translation vectors which preserve the bi-lattice structure. Once these vectors (grain boundary dislocation Burgers vectors) are determined, the analysis of the dislocation content of the interface may proceed using Frank's solution for low-angle boundaries.¹⁰

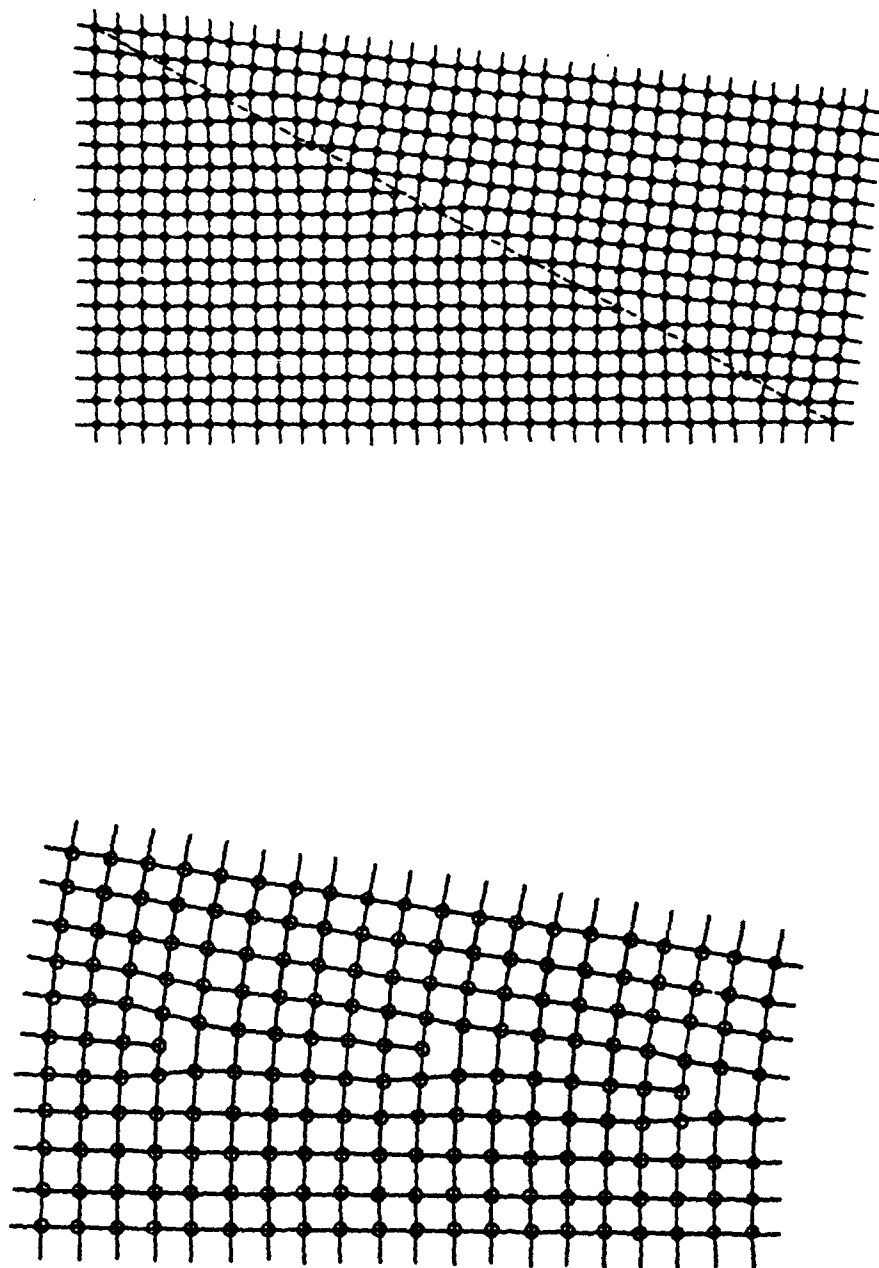


FIGURE 8. Low angle tilt boundaries. a) One Burgers vector. b) Two different Burgers vectors. (10)

Frank's formula was developed as a description for the dislocation content of an interface. Where the Burgers vectors are those of lattice dislocations, it accurately describes low-angle boundaries and is usually simplified with a small angle approximation. In high-angle boundaries, it is used to calculate the DSC dislocation content of a low-angle boundary between two CSLs.

The discrepancy between equivalent points a distance r from the origin in two lattices differing by the angle θ is $r\theta$. Coincidence of the points (the structure of the interface) is re-established if translations summing to $-r\theta$ are accomplished along r . The translations are accomplished by dislocations, each of them \underline{b}_1 . The total Burgers vector content of the portion of the interface traversed by r is $-r\theta$. It is assumed that the interface has equilibrated, i.e., the structure contains the fewest possible dislocations. If the Burgers vectors are known, the line directions and densities are then given by,

$$\underline{r}_1 = [\hat{\underline{u}} \times (\underline{b}_j \times \underline{b}_k)] \times \hat{\underline{v}} \quad 2.2$$

$$\rho_1 = |\hat{\underline{v}} \times (\underline{b}_1^* \times \hat{\underline{u}})|\theta \quad 2.3$$

where the \underline{b}_1^* are the reciprocal lattice vectors,¹⁰

$$\hat{b}_1^* = \frac{\underline{b}_j \times \underline{b}_k}{\underline{b}_1 \cdot (\underline{b}_j \times \underline{b}_k)} \quad 2.4$$

\hat{u} is the unit rotation axis, and \hat{v} is the boundary plane unit normal.

Although it yields no more useful information, the O-lattice approach is a somewhat more elegant solution and is briefly described here. The initial portion of the analysis includes the solution for the CSL and the DSC vectors as a special case for which it is not necessary to introduce the O-lattice.

The fact that coincidence relationships are not described by, at least, piece-wise continuous functions of the transformation render that approach incapable of directly dealing with misorientations from exact CSL rotations. Therein lies the analytical advantage of the O-lattice theory. For any misorientation there exists a lattice of coincident equivalent points or lines. It consists of all the points in lattice two which are coincident with an equivalent point in lattice 1. (which is not to say that all points in either lattice are equivalent). All of these points are possible origins for the rotation, hence the term O(origin)-lattice. At particular discrete values of the rotation, some O-points happen to fall on lattice points, i.e., coincidence sites. The coincidence sites are then a subset of the O-points. The feature of continuity allows the use of straightforward linear algebra to calculate the dislocation content of the interface.

A point in lattice 1 is transformed to a point in 2 by the transformation \underline{A} . \underline{A} may be any affine transformation -- a homogeneous combination of rotation, expansion or shear (parallel lines remain parallel).

$$\underline{x}_2 = \underline{A}\underline{x}_1, \quad 2.5$$

If the points are equivalent, then also

$$\underline{x}_2 = \underline{x}_1 + \underline{t}_1 \quad . \quad 2.6$$

Combining these,

$$\underline{x}_2 = (\underline{I} - \underline{A}^{-1})^{-1} \underline{t}_1 = \underline{T}^{-1} \underline{t}_1 \quad 2.7$$

The vectors \underline{x}_2 describe points differing by translation vectors \underline{t}_1 from, and hence equivalent to, the point described by \underline{x}_1 . The \underline{x}_2 then describe 0 points and Eq. 2.7 is usually written

$$\underline{x}_0 = (\underline{I} - \underline{A}^{-1})^{-1} \underline{t} = \underline{T}^{-1} \underline{t} \quad 2.8$$

\underline{T}^{-1} is some cell in the 0-lattice and can be manipulated to obtain the unit cell. In the case that \underline{A} describes a coincidence relation, the determinant of \underline{T}^{-1} (the volume of the cell enclosed by the three vectors) is Σ/n which implies that the CSL unit cell volume is n times that of the 0-lattice cell. The CSL cell, \underline{C} , is obtained by first

multiplying one column of \underline{T}^{-1} by n , so that $\det \underline{C} = \Sigma$. (n can be the product of several factors. One column should be multiplied by each factor such that each element becomes an integer). The columns are then manipulated by adding multiples of one column to another. The convention is to make one column lie as nearly as possible along the rotation axis, the cell as near orthogonal as possible, and the vectors as short as possible.

The objective at this point is the set of perfect dislocations of the bi-lattice--the DSC unit cell, \underline{D} . In the primitive cubic case, the DSC lattice is the reciprocal lattice to the CSL,

$$\underline{D} = [\underline{C}^{-1}]^T . \quad 2.9$$

As will be discussed, \underline{D} can be modified to describe the fc (or bc) case. If the preceding discussion were to be restricted to the CSL without reference to the O-lattice, the notation would change in the following ways: 1. $\underline{x}_1, \underline{x}_2$ in the O-lattice case refer to any point in crystals 1 and 2, respectively, while in the CSL case they refer only to lattice sites. 2. The transformation A is restricted to a coincidence transformation in the CSL case. 3. For the CSL case, the words "coincident" and "coincidence site" should be substituted for "equivalent" and "O-point". The DSC vectors of Eq. 2.9 combined with Franks solution for low-angle boundaries are sufficient to solve for the dislocation structure of the boundary, and that approach has been utilized throughout the analyses in this work.

The O-lattice solution for a near-CSL high angle grain boundary is based on the following concept. Consider two transformations which differ slightly, \underline{A} and \underline{A}' , e.g., coincidence and near-coincidence orientations. The O-lattices obtained for each will differ slightly,

$$(\underline{I} - \underline{A}^{-1})\underline{x}_0 = \underline{T}\underline{x}_0 = \underline{t} \quad 2.10$$

$$(\underline{I} - \underline{A}'^{-1})\underline{x}'_0 = \underline{T}'\underline{x}_0 = \underline{t} \quad 2.11$$

which yields,

$$\underline{x}'_0 = (\underline{T}'^{-1}\underline{T})\underline{x}_0 = \underline{B}\underline{x}_0 \quad 2.12$$

and \underline{B} is then the transformation from one O-lattice to the other. The boundary has then become a low-angle boundary between two O-lattices, which gives rise to a second order O-lattice, the O2-lattice. Eq. 2.8 becomes, in this case,

$$\underline{x}_{O2} = (\underline{I} - \underline{B}^{-1})^{-1} \underline{d} \quad 2.13$$

where \underline{d} is a translation vector of the O-lattice, the shortest of which are the DSC Burgers vectors. In Eq. 2.8, \underline{x}_0 describes the O-lattice, \underline{A} the transformation between crystals, and \underline{t} is a translation vector of lattice 1. In Eq. 2.13, \underline{x}_{O2} describes the O2 lattice, \underline{B} the transformation between the O-lattice and the O'-lattice

and \underline{d} is a translation vector of the O-lattice. Equation 2.13 is the O-lattice solution for the dislocation content of the interface.

The misorientation forming the grain boundary can always be described by a pure rotation. A simple rotation, however, is a matrix of rank 2 and a rank 3 description of a matrix of rank 2 will have a determinant = 0, i.e., the volume of the O-lattice cell = 0. This means that the lattice is adequately described by a line lattice. In the third dimension, the O-points can be thought of as O-lines. A suitable choice of transformation which is not pure rotation but which accomplishes the same configuration will yield a solution of rank 3. The choice of transformation is non-physical and some solutions simply contain less information than others. In order to solve for the CSL and DSC lattices, it is necessary that we choose one that contains adequate information, i.e., $\det \neq 0$. Different solutions consist of different choices of equivalent point in lattice 2 which is related to a point in lattice one. As noted above, the smallest difference vectors will be obtained only through the choice of translation vectors which describe the positions of sites which are nearest neighbors after the transformation. In most cases, that will not be differences between equivalent vectors. An equivalent transformation which is made up of rotation and shear and which does relate nearest neighbors may be obtained by operating on \underline{R} with a unimodular transformation \underline{U} . (A unimodular transformation has determinant ± 1 .) Such a choice will also yield a solution with non-zero determinant.

$$(\underline{I} - \underline{A}^{-1}) = (\underline{I} - \underline{UR}^{-1}) \quad 2.14$$

2.3 Calculation of DSC Vectors

Tables which include the rotation matrix, CSL, and DSCL for sigma up to 49 are available in the literature,¹⁸ as are listings of axis/angle pairs through $\Sigma = 101$.⁶² Several of the boundaries investigated in the course of this study required consideration of high-sigma disorientations. In addition, the DSCL's were recalculated in all cases using the rotation axis as assigned on the stereogram used during TEM investigations, as opposed to transforming one set of coordinates.

The rotation matrix is given in terms of the angle and axis, \hat{u}/θ , by,⁶³

$$\underline{R} = \begin{bmatrix} u_1^2(1-c\theta)+c\theta & u_1u_2(1-c\theta)-u_3s\theta & u_1u_3(1-c\theta)+u_2s\theta \\ u_1u_2(1-c\theta)+u_3s\theta & u_2^2(1-c\theta)+c\theta & u_2u_3(1-c\theta)-u_1s\theta \\ u_3u_1(1-c\theta)-u_2s\theta & u_2u_3(1-c\theta)+u_1s\theta & u_3^2(1-c\theta)+c\theta \end{bmatrix} \quad 2.15$$

where $c\theta = \cos\theta$ and $s\theta = \sin\theta$.

The procedure described by Eqs. 2.8, 2.9 and 2.14 was used to calculate the CSL and DSCL. \underline{U} of Eq. 2.14 was arrived at by trial and error. It is taken to be made up of elements of 0 or ± 1 . For low Σ disorientations, it often looks much like the rotation matrix with the

elements all rounded to such values. For high Σ 's, it may be quite dissimilar. The procedure used here (after exhausting guesses similar to \underline{R}) was to compile a list of \underline{U} 's and try them in succession until a solution with $n = 1$ or 2 is obtained. Solutions at larger n can require much matrix manipulation to determine \underline{C} . The results for $\Sigma > 49$ are presented in Table 1.

2.4 Boundaries in Ordered Materials

Ordering of a lattice adds additional information about the surroundings at a given point in the lattice. Whereas before ordering lattice points were compared based on the presence of other points in particular locations, after ordering they are also examined for type. The same distinction must also be made in considering the boundary structure. In a grain boundary between two disordered crystals, a coincidence site is simply a site which belongs to both crystals. In the ordered lattice, each lattice imposes a type on the site. If the types are the same, then the site is consistent with the ordering in each crystal. If not, there is an antiphase energy associated with the site. For example, for the boundary of Fig. 9(a), the CSL is ordered at the left. To the right of the dislocation, which is a perfect dislocation of the disordered boundary, there is disorder of the CSL across the boundary. A second Burgers vector of the same type restores the order [Fig. 9(b)].

TABLE 1

Selected CSL Lattices for $\Sigma > 49$

Σ	\hat{u}	$\Sigma \cdot \underline{R}$	CSL	$\Sigma \cdot \text{DSCL}$
51a	$10\bar{1}$	50 10 $\bar{1}$	$\bar{2}9$ 5 1	1 5 25
		$\bar{1}0$ 49 $\bar{1}0$	11 $\bar{1}$ 0	10 $\bar{1}$ $\bar{5}$
		$\bar{1}$ 10 50	$\bar{3}0$ 5 $\bar{1}$	1 5 $\bar{2}6$
57c	$01\bar{1}$	41 28 28	2 5 0	4 7 9
		$\bar{2}8$ 49 $\bar{8}$	3 $\bar{6}$ 1	7 $\bar{2}$ 30
		$\bar{2}8$ $\bar{8}$ 49	4 $\bar{5}$ $\bar{1}$	7 $\bar{2}$ $\bar{2}7$
59b	$01\bar{1}$	41 30 30	$\bar{5}$ 3 0	$\bar{1}0$ 3 $\bar{1}5$
		$\bar{3}0$ 50 $\bar{9}$	0 5 1	3 5 34
		$\bar{3}0$ $\bar{9}$ 50	3 5 $\bar{1}$	3 5 $\bar{2}5$
73b	$10\bar{1}$	72 12 $\bar{1}$	0 5 1	1 6 43
		$\bar{1}2$ 71 $\bar{1}2$	6 $\bar{7}$ 0	12 $\bar{1}$ 5
		$\bar{1}$ 12 72	1 6 $\bar{1}$	1 6 $\bar{3}0$
83a	$10\bar{1}$	81 18 $\bar{2}$	$\bar{4}$ $\bar{3}$ 1	$\bar{9}$ 1 46
		$\bar{1}8$ 79 $\bar{1}8$	1 10 0	2 9 $\bar{1}$
		$\bar{2}$ 18 81	$\bar{5}$ $\bar{4}$ $\bar{1}$	$\bar{9}$ 1 $\bar{3}7$
99a	$10\bar{1}$	98 14 $\bar{1}$	$\bar{6}$ 7 1	$\bar{7}$ 8 49
		$\bar{1}4$ 97 14	8 $\bar{1}$ 0	1 13 $\bar{1}$
		$\bar{1}$ 14 98	$\bar{7}$ 7 $\bar{1}$	$\bar{7}$ 8 $\bar{5}0$

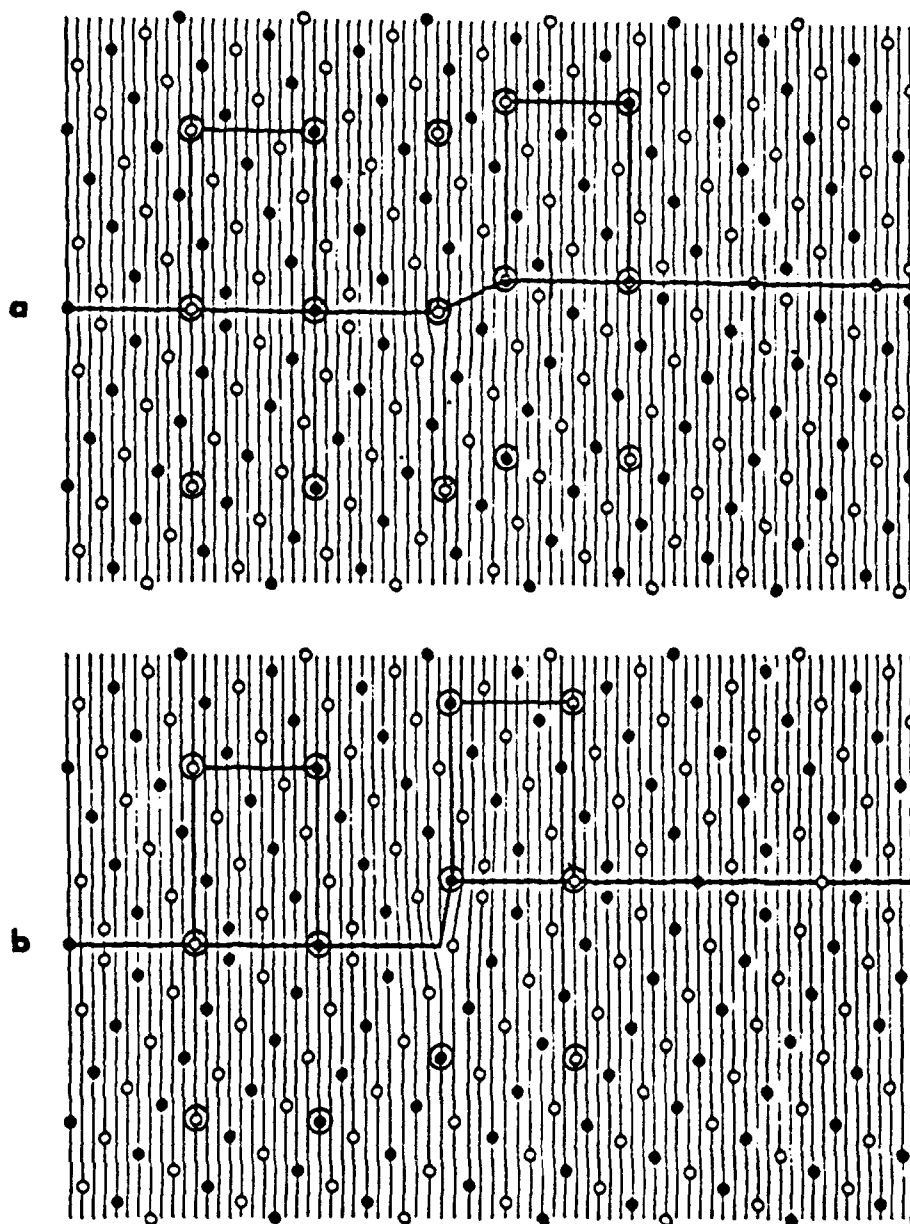


FIGURE 9. a) Grain boundary dislocation of the disordered (fc) structure in an ordered $L11'$ boundary between crystals of the $L1_2$ structure. Anti-coincident region to the right. b) Dislocation of the ordered boundary (twice the magnitude in a) preserves the structure. (56)

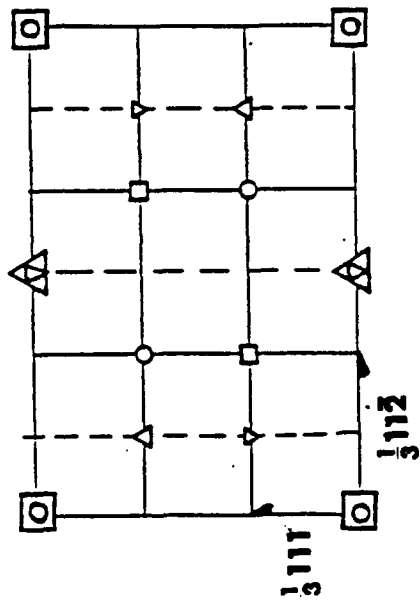
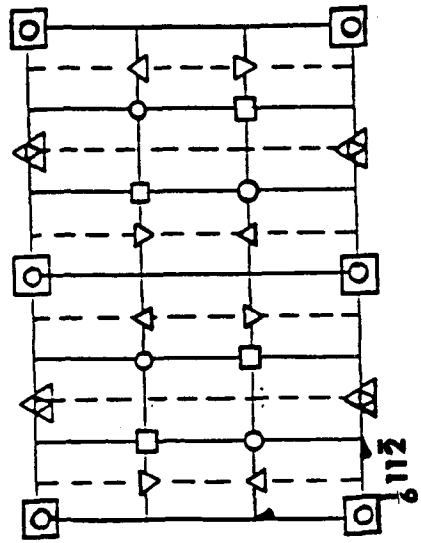
(The terminology used here with reference to a coincidence boundary between two ordered crystals which is mismatched by type [Fig. 9(a)] will be "anti-coincidence sites", "anti-order" and "misorder". The term "disordered boundary" is taken to mean that the atoms in the boundary are randomly placed by type. If the crystals are ordered, this implies two additional interfaces between the ordered and near-boundary disordered regions.)

The most incisive discussion of the subject is that of Clark and Pond.⁵² An elegant argument is made that the Burgers vectors of perfect boundary dislocations will be only those of the ordered structure. It seems reasonable to consider the possibility of vectors of the disordered boundary as partials grouped to form perfect vectors of the ordered structure with the spacing being dependent upon the antiphase energy of the boundary. As an analogy, if we consider the ordered structure of Ni_3Al , it is simple cubic with four atoms per point. Considering only that much of the crystallography, the expected slip system would be $\langle 100 \rangle \{110\}$. In fact the predominant slip system is that of the disordered lattice doubled such that it is a translation vector of the perfect lattice, specifically $\langle 110 \rangle \{111\}$, occurring as pairs of partials which are perfect dislocations of the disordered lattice. Alternatively, if one imagines the ordering energy decreasing, a point must be reached at which elastic considerations favor the shorter vectors.

Of course, all near-boundary sites are subject to the same considerations regarding types of near-neighbors, not only coincidence

sites. Casual inspection of Fig. 9, for example, does not immediately reveal whether the coincidence or anti-coincidence structure has fewer incorrect near-neighbor bounds. It is likely for low symmetry boundaries, that no simple translations in the boundary appreciably change the average matching by type of non-coincident sites across the boundary, while the coincidence sites are an insignificant contribution. On the other hand, it must be that ordering plays a role in a $\Sigma = 3$ boundary, so the question is at what level of complexity of boundary structure, if any, is ordering no longer important?

The perfect dislocations of an ordered (pc) boundary differ from those of the disordered (fc) boundary in different fashions depending upon the particular boundary structure. In some cases, two of the disordered basis vectors will be half the length of the ordered vectors (Fig. 10). In others, one or two of the vectors may differ in direction as well (Fig. 11). (The latter appears in the formalism as a need to reshape the DSC matrix before face-centering.) In either event, the b_{3i} 's differ in direction and magnitude. In general, the ordered and disordered solution sets will differ, albeit in some cases, only in spacing of one set. Consequently, the CSL formalism has the potential for distinguishing between ordered and disordered boundary structures. Furthermore, a situation analogous to that in the lattice may exist, wherein a perfect dislocation of the ordered boundary consists of partials which are dislocations of the disordered boundary with an associated grouping.



(110)

FIGURE 10. DSC vectors of the ordered and disordered $\Sigma 3$ CSL.

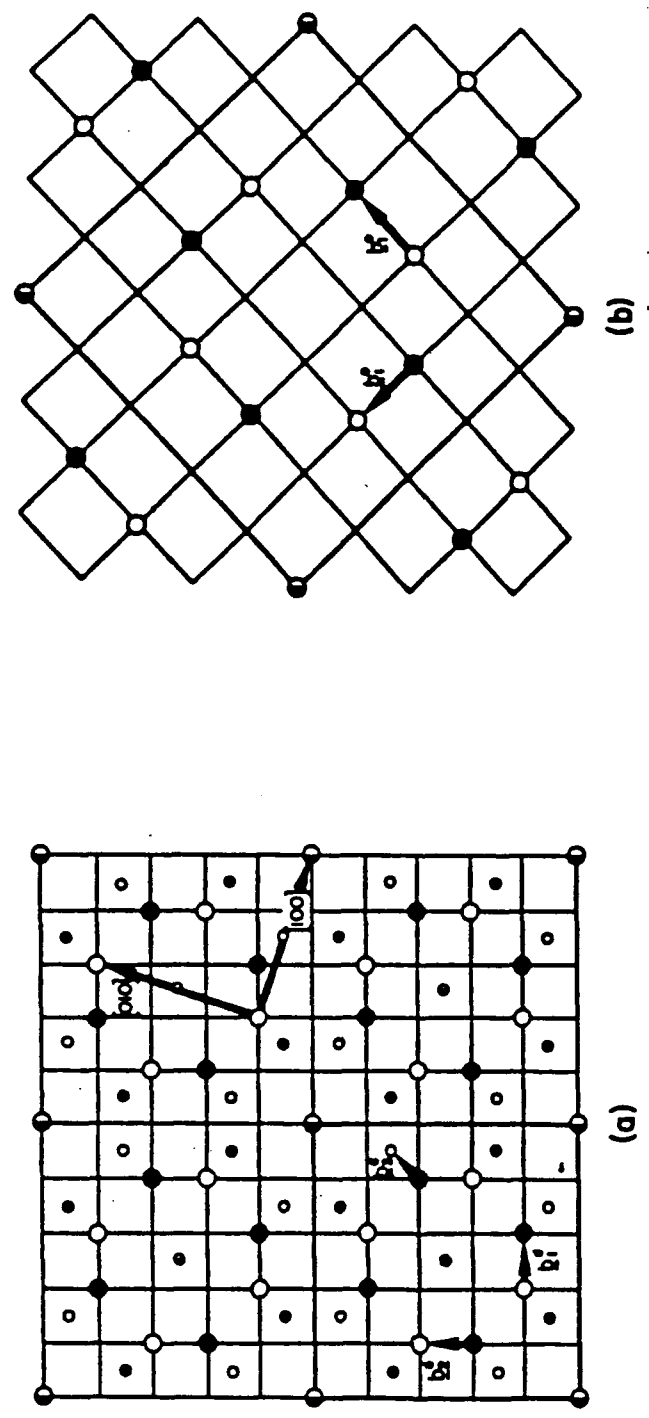


FIGURE 11. DSC vectors of the ordered and disordered I5 CSL in an $L1_2$ structure. (52)

CHAPTER III

GRAIN BOUNDARY STRUCTURE: EXPERIMENTS

Two boundaries in Ni - 24.5 at.% Al have been studied thoroughly and will be discussed in detail. Numerous others have been inspected in a less thorough manner. A few notable features of these will be briefly discussed in Chapter VI. Observations related to the effects of B in boundaries, but not directly relevant to structure determinations, are presented in Chapter V.

3.1 Experimental Procedure

3.1.1 Sample Preparation

Specimens were fabricated by arc-melting 150 g ingots from pre-forms of cold-pressed high purity powders of Ni and Al. The ingots were turned and remelted several times. Portions of the billets were then isothermally forged at 1100°C in vacuum and subsequently annealed at 1200°C for 1 hour. Compositional uniformity was confirmed utilizing electron microprobe analysis. A typical chemical analysis by wet chemical and vacuum fusion is shown in Table 2. Average grain size was about 100 micrometers. Foils for TEM

TABLE 2
Typical Chemical Analysis

Element	Amount
Ni	86.7 wt. %
Al	12.7
B	0.014
Si	200 ppm
Mn	30
Fe	400
Cu	70
Cr	< 100
W	< 300
Co	< 10
O	40

analysis were ground to 0.005 in. thick, and jet polished in a solution of 2% perchloric acid in butoxy-ethanol at $-20 < T < 0^{\circ}\text{C}$.

3.1.2 Approximate Misorientation from Stereographic Projection

It is useful during the analysis to quickly determine the angle and axis of the misorientation while at the microscope. The following procedure was used. Both crystals were plotted on a stereogram by measuring the tilt angles of several zone axes using a double-tilt TEM stage. The rotation axis and angle can be determined by construction. However, a simpler and more precise approach is that described by Clark.⁶¹ The rotation matrix is made up of the column vectors of the "new" axes as represented in the "old" system. The components are the direction cosines to each axis. That is, the elements of \underline{R}' are

$$a_{ij} = \cos \rho_{ij} \quad 3.1$$

where ρ_{ij} is the angle between the axes \underline{x}_i in the old system and \underline{x}_j in the new system. Once the rotation matrix is obtained, the rotation angle is given by

$$\theta = \arccos((\text{trace } \underline{R}' - 1)/2) \quad 3.2$$

where trace $\underline{R}' = r_{11} + r_{22} + r_{33}$. The axis of rotation is given by the eigenvector of \underline{R} ,

$$\underline{u}_i = r_{kj} - r_{jk}. \quad 3.3$$

3.1.3 More Precise Determination of Misorientation

In order to determine the boundary structure with any degree of certainty it is necessary to accurately determine the misorientation. While diffraction spot patterns are relatively insensitive to small tilts, Kikuchi patterns behave as though they are rigid extensions of the crystal. This allows accurate determination of orientation. Two approaches were utilized in this work. Both use patterns taken on either side of the boundary at the same tilt and basically constitute the same calculation. The details differ considerably, however.

In principle, the first approach requires only patterns with any three Kikuchi bands not all of the same zone. If the Kikuchi pattern is correctly indexed: 1. The camera length (radius of Ewald sphere, r) can be computed. 2. The three K-bands can be extended to the three poles at the intersections. 3. The distances (arc lengths, l) of the three poles to the origin are then measured, and 4. The angle(s) of tilt from the known pole(s) are determined from $l = r\theta$. The precise orientation of the crystal with respect to the microscope is then known. Once this is accomplished for both crystals, the relative misorientation may be calculated. Practically, if the

K-bands are not low index, it is virtually impossible to index them, therefore the plates should be taken with care. When a known pole is present, a variation of the procedure replaces step 2 with a determination of the orientation of a known direction in the zone. These procedures have been described elsewhere as have the computer programs with which the calculations were performed.^{64,65}

This approach was used for boundary 2. The uncertainty was assigned to cover the spread of three separate determinations. Had this value been smaller than the uncertainty estimated by Young, Steele and Lytton,⁶⁴ the larger value would have been assigned. Clark has discussed in detail uncertainties involved in misorientation determination, including this technique.⁶¹ The misorientation was found to be $42.776 \pm 0.164^\circ$ about $[\ .620 \ - .7839 \ .0289] \pm 1.17^\circ$.

The second approach differs first in that the plates are taken from an orientation such that a reasonably low index pole of each crystal will fall on the plate. Although this sounds fortuitous, such conditions are nearly always available for near-CSL misorientations. The rotation matrix is then the product of the rotation required to bring the poles into coincidence, which is readily calculated, and those required to rotate slightly away from coincidence to the configuration on the plate. This approach has some advantage in simplicity in that it is more easily calculated by hand, and measurements are made on one plate from pole to pole rather than each crystal to a separate reference frame. Consequently there are half as many

measurements, i.e., one measurement of angle and two measurements of distance.

Both methods were used in the case of boundary 1. The second method, in which \underline{R}' is found as the product of more easily determined rotations, is described in some detail. In this case, $\underline{P}_1 = [012]_1$ and $\underline{P}_2 = [132]_2$ are nearly coincident (Fig. 12). For analysis in crystal 2, the rotation axis for \underline{R}_1 is given by $\underline{P}_1 \times \underline{P}_2 = [\bar{4} \ 2 \ \bar{1}]$, and the angle by

$$\theta = \arccos[\underline{P}_1 \cdot \underline{P}_2 / (|\underline{P}_1| |\underline{P}_2|)] = 33.211^\circ \quad 3.3$$

The rotation matrix is given by Eq. 2.15, and is,

$$\underline{R}_1 = \begin{pmatrix} .96111 & .05729 & .27016 \\ -.18175 & .86777 & .46256 \\ -.20793 & -.49365 & .84444 \end{pmatrix} \quad 3.4$$

\underline{R}_1 is not necessarily nearly-equivalent to the actual rotation, so a rotation about the now common direction is required. A direction in \underline{P}_1 is chosen and operated upon by \underline{R}_1 yielding its transformed direction. The angle between the transformed direction and a direction in \underline{P}_2 is calculated. The difference between the measured angle and the calculated angle is the rotation to be accomplished by \underline{R}_2 . In this case, $[012]_1$ contains $[\bar{1}00]$, and $[132]_2$ contains $[1\bar{1}1]$. The calculated angle α is given by the angle between $\underline{R}_1[\bar{1}00]_1$ and $[1\bar{1}1]_2$. If

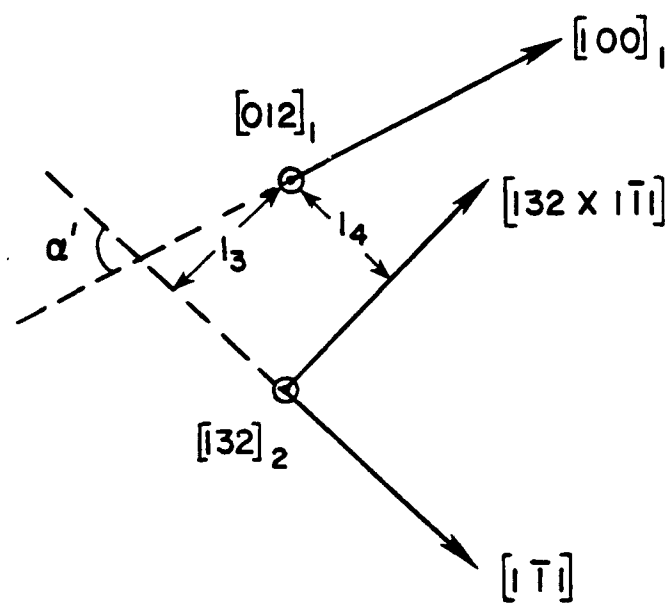


FIGURE 12. Misorientation determination from near-colinear zone axes.

the measured angle is α' , R_2 performs the rotation through angle $\alpha' - \alpha$ about $[132]_2$. Specifically,

$$R_1 \begin{bmatrix} \bar{1} \\ 0 \\ 0 \end{bmatrix} = \begin{bmatrix} -1.6083 \\ 0.3041 \\ .3479 \end{bmatrix}, \quad \alpha = -122.669^\circ \quad 3.5$$

The measured angle is -80.5° or $180 - 80.5 = -99.5^\circ$. In this case, it is -99.5° . The required rotation for R_2 is, then, $-99.5^\circ + 122.669^\circ = 42.169^\circ$ about $[132]$.

$$R_2 = \begin{bmatrix} .75966 & -.30337 & .57523 \\ .41430 & .90756 & -.06849 \\ -.50128 & .29035 & .81512 \end{bmatrix} \quad 3.6$$

Axes centered upon P_2 are chosen and the displacement of P_1 is measured. In this case the axes were chosen to be $[1\bar{1}1]$ and $[132] \times [1\bar{1}1]$. The displacements are, to a good approximation, the arc lengths of the rotations accomplished by R_3 and R_4 about the respective axes.

$$\theta_3 = l_3/L = \frac{(-4.2 \text{ mm} \cdot 180)}{(504 \text{ mm} \cdot \pi)} = -0.4775^\circ \text{ about } [1\bar{1}1] \quad 3.7$$

where L is the camera length. Similarly, l_4 is -3.6 mm and $\theta_4 = -0.4093$ about $[51\bar{4}]$. The matrices are given by Eq. 2.15, as above.

The total rotation then is given by

$$\underline{R}' = \underline{R}_4 \underline{R}_3 \underline{R}_2 \underline{R} = \begin{bmatrix} .66314 & -.50401 & .55338 \\ .23990 & .84342 & .48070 \\ -.70901 & -.18601 & .68022 \end{bmatrix} \quad 3.8$$

A simple analysis of the sources of error reveals that the uncertainty in the measurement of angle is by far the largest. Distances can be measured reliably to 0.5 mm. If two plates are used, there is an additional distance measurement, for a total of three. The worst case then, is the angular uncertainty due to 1.5 mm deviation, which by Eq. 3.7 is 0.17° . The estimated uncertainty in angle is 0.5° , which contributes directly to the uncertainty in R' (or \hat{u}) for a total of 0.53° . In fact, eight determinations using two methods yielded a spread in angle of $\pm 0.43^\circ$ and in \hat{u} of ± 0.35 . The uncertainty will be taken to be $\Delta\theta = \pm .3^\circ$, $\Delta u = \pm .3^\circ$.

The uncertainty in R_{02} is more problematical. R_{02} is essentially a small difference in two large values. To make matters worse, the rotation axis is a vector difference, so that a small error in R' can cause a very large error in \hat{u} . It is clearly important that measurements be made carefully. The actual spread in R_{02} was $\Delta\theta = \pm 0.35^\circ$ and $\Delta u = \pm 5^\circ$. The estimated uncertainties are $\Delta\theta = .25^\circ$, $\Delta u = \pm 3^\circ$. The resulting spread in line directions was 16° and 7° for sets A and B,

respectively. The spacings varied from 6.3 to 3.9 nm and 1.7 to 2.3 nm.

3.1.4 Determination of Boundary Plane

Determination of the boundary plane can be done by straightforward trace analysis if the boundary can be tilted edge-on, as in the case of boundary 2. The uncertainty, as estimated by multiple determinations, is about $\pm 5^\circ$.

In the case of boundary 1, the orientation of the boundary with respect to the plane of the foil prevented such a tilt. The procedure used here differs in some respects from those described elsewhere and is developed in some detail. All such procedures are basically the same in that two lines lying in the boundary are chosen and observed from two known orientations. The equations of the lines can then be solved uniquely and the cross product yields the boundary normal.

The lines on the plates are projections of the features onto the plane of the plate and the out-of-plane components are unknown (Fig. 13). By obtaining two views differing by a known transformation, one obtains equations of the form,

$$P_{2x} = T_{11} P_{1x} + T_{12} P_{1y} + T_{13} P_{1z} \quad 3.9$$

where the p_{ij} are the j 'th components of the line d in the i 'th reference frame, T is the transformation, and the only unknown is p_{1z} .

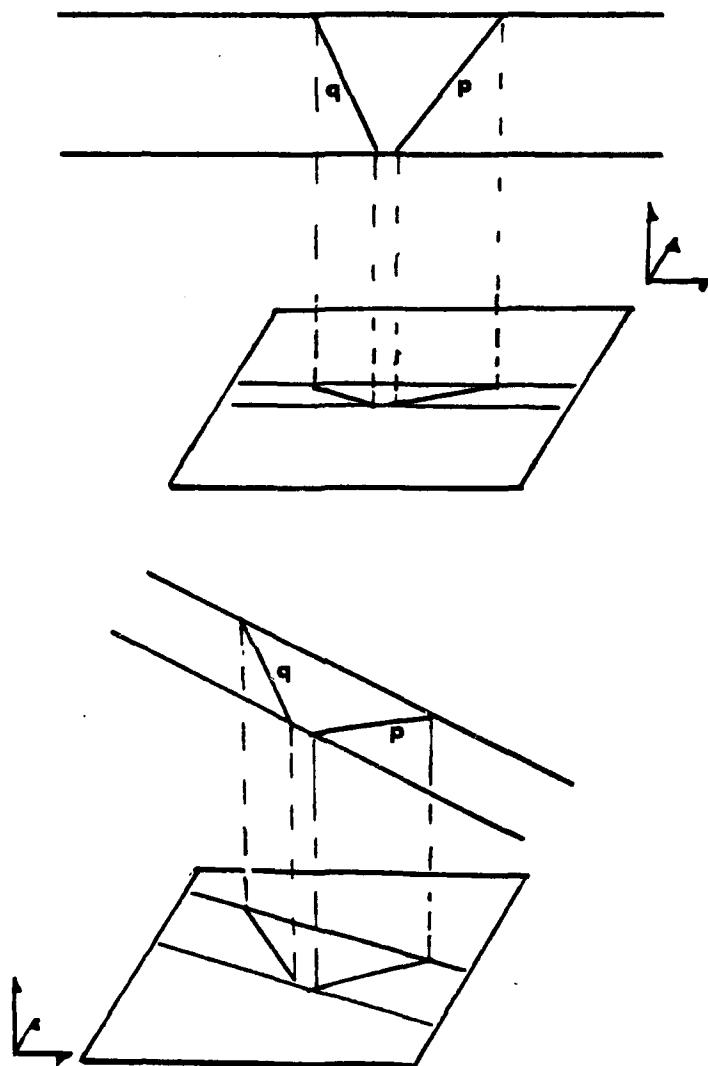


FIGURE 13. Line features p, q in boundary projected on TEM plate from two different orientations of the boundary.

In order to simplify the precise determination of the orientations, the plates were exposed such that there was a low index pole in the diffraction pattern. The images are, of course, of poor quality, but they can be obtained with sufficient detail to determine the line directions and lengths. The procedure is as follows: 1. Two line features in the boundary are chosen. 2. Two images are exposed such that a different known pole (preferably low index) of the same crystal, separated by a rotation about a common axis, is on each diffraction pattern. 3. Lengths and directions of the projections of the features are measured in the frames of each of the microscope plates, RF_1 , RF_2 . 4. Coordinates are transformed from RF_1 to RF_2 . 5. Two sets of values are then available for the x and y components of the lines in RF_2 : those just transformed from RF_1 , which are in terms of the unknowns p_{1z} and q_{1z} , and the measured values. The two expressions containing the measured and transformed in-plane components are solved for the out-of-plane component of each line. 6. The boundary normal \hat{v} is determined by taking the cross product of the resulting vectors. 7. \hat{v} is then transformed to the crystal frame.

In the case of boundary 1, P_{1z} is $[011]$ and P_{2z} is $[\bar{1}11]$ and the approximate rotation axis is $[01\bar{1}]$ in the crystal frame. Coordinates are chosen along $[100]$ and $[01\bar{1}]$ and the distances along these directions from \underline{B} to \underline{P}_1 are carefully measured on large prints (Fig. 14). The distance so measured divided by the camera length is the required angle of rotation. A transformation of coordinates from \underline{B} to \underline{P}_1 (or

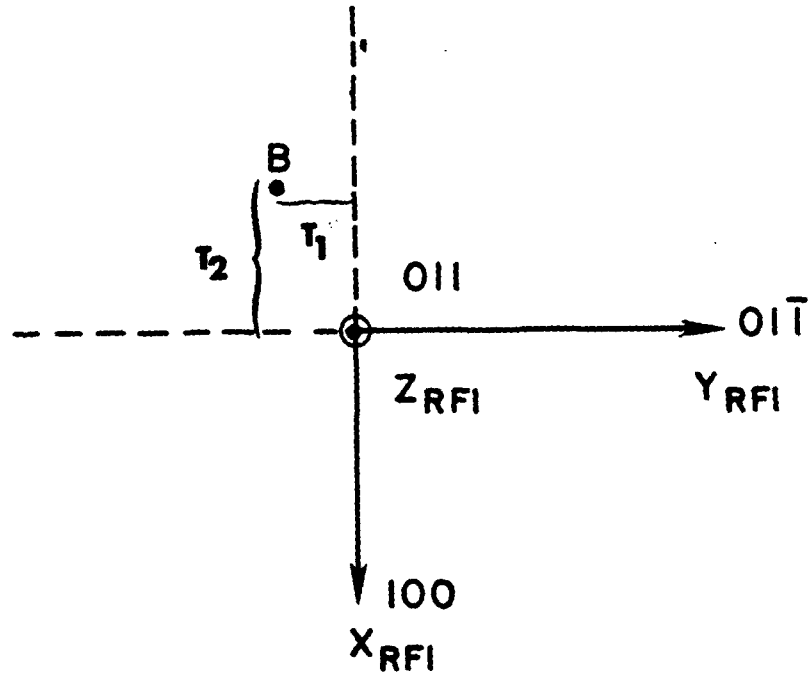


FIGURE 14. Determination of transformation for gb normal.

rotation from P_1 to B) will require $T_{\underline{1}}$, which is a rotation of 0.5571 about $[100]_{RF1,CF}$, and $T_{\underline{2}}$, which is a rotation of -1.508 about $[010]_{RF1}$, $[01\bar{1}]_{CF}$. The matrices are given by Eq. 2.15. $T_{\underline{3}}$ is then required to transform from P_1 to P_2 and is the matrix of direction cosines of the bases as given by Eq. 3.1.

$$\begin{array}{c}
 \underline{P}_2 \\
 \begin{array}{l}
 211 \\
 01\bar{1} \\
 \bar{1}11
 \end{array}
 \end{array}
 \begin{array}{c}
 \underline{P}_1 \\
 \begin{array}{l}
 100 \\
 01\bar{1} \\
 011
 \end{array}
 \end{array}
 \left[\begin{array}{ccc}
 .8165 & 0 & .5773 \\
 0 & 1 & 0 \\
 -.5773 & 0 & .8165
 \end{array} \right]
 \quad 3.10$$

$T_{\underline{4}}$ is then required to transform from P_2 to RF_2 by a rotation of 1.647° about $[100]_{RF2}$, $[211]_{CF}$ in the same fashion as $T_{\underline{1}}$, $T_{\underline{2}}$. The complete transformation is then

$$\underline{T} = T_{\underline{4}} T_{\underline{3}} T_{\underline{2}} T_{\underline{1}} \quad 3.11$$

and

$$\begin{bmatrix} P_{2x} \\ P_{2y} \\ P_{2z} \end{bmatrix} = \underline{T} \begin{bmatrix} P_{1x} \\ P_{1y} \\ P_{1z} \end{bmatrix} \quad 3.12$$

This yields two equations of the form of Eq. 3.9 for each line with one unknown for each pair, e.g., p_{1z} . Since the solution is over determined, an additional factor (m) may be introduced to compensate for (small) differences in magnification between images and the equations solved simultaneously. This also serves to average the values, in a sense, by finding the most consistent solution. Equation 3.9 then becomes

$${}^m P_{2x} = T_{11} P_{1x} + T_{12} P_{1y} + T_{13} P_{1z} \quad 3.13$$

$${}^m P_{2y} = T_{21} P_{1x} + T_{22} P_{1y} + T_{23} P_{1z}$$

There is a similar set for q_1 , q_2 and n . Comparison of the magnification factors (they should be the same) provides a check for consistency. Once these equations are solved for p_{1z} and q_{1z} the gb normal is given by $\underline{d} \times \underline{f}$, in the coordinates of RF_1 . All that remains is to transform to the crystal frame, CF. This is most easily accomplished by transforming from RF_1 to \underline{P}_1 then \underline{P}_1 to CF. The former has already been determined to be $T_{21} T_{11}$. The latter, T_{51} , is determined in the manner of Eqs. 3.1 and 3.10 by

		RF			
		100	01 $\bar{1}$	011	
	100	1	0	0	
CF	010	0	1/ $\sqrt{2}$	1/ $\sqrt{2}$	3.14
	001	0	1/ $\sqrt{2}$	1/ $\sqrt{2}$	

The complete transformation is then

$$\underline{C} = \underline{T}_5 \underline{T}_2 \underline{T}_1 \quad 3.15$$

In summary, the transformation between reference frames, \underline{T} (Eq. 3.11), is determined and applied to features $\underline{p}_1, \underline{q}_1$. The calculated and measured $\underline{p}_2, \underline{q}_2$ are used to determine the unknown component of $\underline{p}_1, \underline{q}_1$ (Eq. 3.12). The grain boundary normal in crystal coordinates is then

$$\underline{v} = \underline{C} (\underline{p}_1 \times \underline{q}_1) \quad 3.16$$

In order to estimate uncertainties, consider Eq. 3.13 rearranged to solve for the unknown p_{1z} ,

$$p_{1z} = \frac{m}{T_{13}} p_{2x} \frac{T_{11}}{T_{13}} p_{1x} \frac{T_{12}}{T_{13}} p_{1y} \quad 3.17$$

It is difficult to identify the intersection of the boundary with the foil surface, so the uncertainty in length of d is large and combines with the uncertainty in angle for an estimated uncertainty in the p_{1j} of ± 2 mm, or typically about 6%.

The uncertainty in the matrix elements is determined by the uncertainty in the distance measurements on the diffraction patterns. The rotation angle is given by

$$\cos \theta = 1/2 (\text{trace } T - 1) = 1/2 (T_{11} + T_{22} + T_{33} - 1) \quad 3.18$$

and,

$$d \cos \theta = 1/2 (dT_{11} + T_{22} + T_{33}) = 3/2 dT_{ij} \quad 3.19$$

Since

$$d \cos \theta = -\sin \theta d\theta = -\theta d\theta \quad 3.20$$

for small angles, then

$$\Delta T_{ij} = 2/3 \theta d\theta \quad 3.21$$

Theta is about 1° and $\Delta \theta$ about .06, and

$$\Delta T_{ij} = 2/3 (.06) (\pi/180)^2 = 1.2 \times 10^{-5} \quad 3.22$$

Since T_{ij} is typically 0.5 or so, its uncertainty is negligible as compared to the p_{ij} .

If the error is taken to be in the rotation axis as the angular difference in two unit vectors, the measured \hat{u} and the actual \hat{x} , the angle is

$$\cos \beta = \hat{u} \cdot \hat{x} = \frac{u_1 x_1}{r_1} + \frac{u_2 x_2}{r_2} + \frac{u_3 x_3}{r_3} \quad 3.23$$

and

$$d \cos \beta = du_i + du_j + du_k = 3du_i \quad 3.24$$

Since the \underline{u}_i are all of the form

$$\underline{u}_i = T_{kj} - T_{jk} \quad 3.25$$

then

$$du_i = 2dT_{ij} \quad 3.26$$

and these two expressions yield

$$dT_{ij} = 1/6 d \cos \beta \quad 3.27$$

which is 1/4 the value calculated in Eq. 3.22. Therefore the uncertainty in the transformation is negligible.

There is also a small error in that measurements in the frame of the plates are assumed to be along crystallographic directions contained in the zone axis on that plate. In fact, those axes lie near, but not in, the plane of the plate (unless, of course, the pole is along the beam direction). The error introduced, however, is in the cosine of small angles and is extremely small. In this case the

largest is .039% which is negligible compared to the uncertainties of measurements.

Taking T to be errorless, the differential of 3.17 is then

$$dp_{1z} = 1/T_{13} (m dp_{2x} + T_{11} dp_{1x} + T_{12} dp_{1y}) \quad 3.28$$

Since $0 < T_{ij} < 1$, and they generally sum to about 1, and $m \approx 1$ then

$$dp_{ij} < dp_{1z} < 5 dp_{ij} \quad 3.29$$

In fact, the simultaneous solution performs an averaging function which improves the uncertainty somewhat, and the value will be taken to be

$$dp_{1z} \approx 3 dp = \underline{+6} \text{ mm} \quad 3.30$$

Now we have the cross product of two vectors each with an uncertainty of 4% in two components and 12% in the other. If we treat it as a simple product with an average uncertainty of 7%, the product has an uncertainty of 14%. To see what this means in terms of angle, a [111] unit vector is increased in one component and decreased in the other two by 14% and the resulting angle calculated, i.e., the angle between [.58 .58 .58] and [.66 .50 .50], which is 7.8°. In fact, the constants m and n provide an internal check, and the estimation has been done pessimistically throughout. A reasonable estimate is $\Delta u = \underline{+6}^\circ$.

In summary, the principal contribution to the uncertainty is from the measurement of lengths and directions on the images. All other sources are insignificant by comparison. The major problem is in distinguishing the intersection of the boundary with the foil surface, i.e., the ends of the lines. This is basically an inherent contrast problem, but is affected by image quality. Therefore it is not wise to sacrifice too much in image quality for ease in calculation of the transformation.

3.1.5 Solution for Boundary Structure

The measured disorientation axis/angle pairs were compared to those of CSL relationships to $\Sigma = 101$. Ordered and disordered CSL and DSC lattices were calculated for each possibility. Complete solutions were then developed for each of the ordered and disordered CSL's, following the procedure described in Chapter II. The grain boundary dislocation line directions and spacings predicted by each solution were compared to the experimental values. Those which yielded line directions in reasonable agreement with experiment were then examined by g·b analysis.

3.2 Boundary 1: $\Sigma = 31$

The segment of boundary analyzed is populated with a number of extrinsic dislocations. In addition, and of principal interest here,

there are two sets of intrinsic secondary grain boundary dislocations which are resolvable. These will be referred to as set A (Figs. 15-18) and set B (Figs. 18 and 19). There are several other notable features in the region of boundary analyzed. There is a relatively high density of extrinsic dislocations and several loops which were frozen in the process of leaving or entering the boundary (Figs. 16, 17, 20). The extrinsic dislocations are generally paired and have spacings greater than, but of the same order of those found in the lattice (Fig. 19). (The mottled area at the edge of the boundary at the top in the photos is an area of surface contamination.)

The plotted stereographic projection yielded a misorientation of $53.39^\circ \pm 3.0^\circ$ about $\hat{u} = [-.42 \ .77 \ .48]$. The precise misorientation was measured using method 2 of Section 3.1.3 and was found to be $53.684^\circ \pm 0.6^\circ$ about $\hat{u} = [-.41607 \ .78337 \ .46175]$. The rotation angles differ by 0.29° and the axes differ by 1.3° which is quite good agreement. The only likely CSL relationships are $\Sigma = 31b$ which is 52.19° about $[\bar{1}21]$, or $\Sigma = 21b$ which is 44.40° about $[\bar{1}21]$. Complete solutions were developed for both ordered and disordered CSL's of each type, following the procedure described in Section 3.1.5. The $\Sigma = 21b$ relationship provided no reasonable solution.

The $\Sigma = 31b$ DSC basis vectors are,

$$\underline{b}_i = 1/31 \begin{bmatrix} 7 & 2 & -8 \\ 2 & 5 & 11 \\ 3 & -8 & 1 \end{bmatrix}_2 \quad \text{and} \quad \underline{b}_i' = 1/31 \begin{bmatrix} 3 & 8 & -1 \\ -2 & 5 & 11 \\ 7 & -2 & 8 \end{bmatrix}_1 \quad 3.31$$

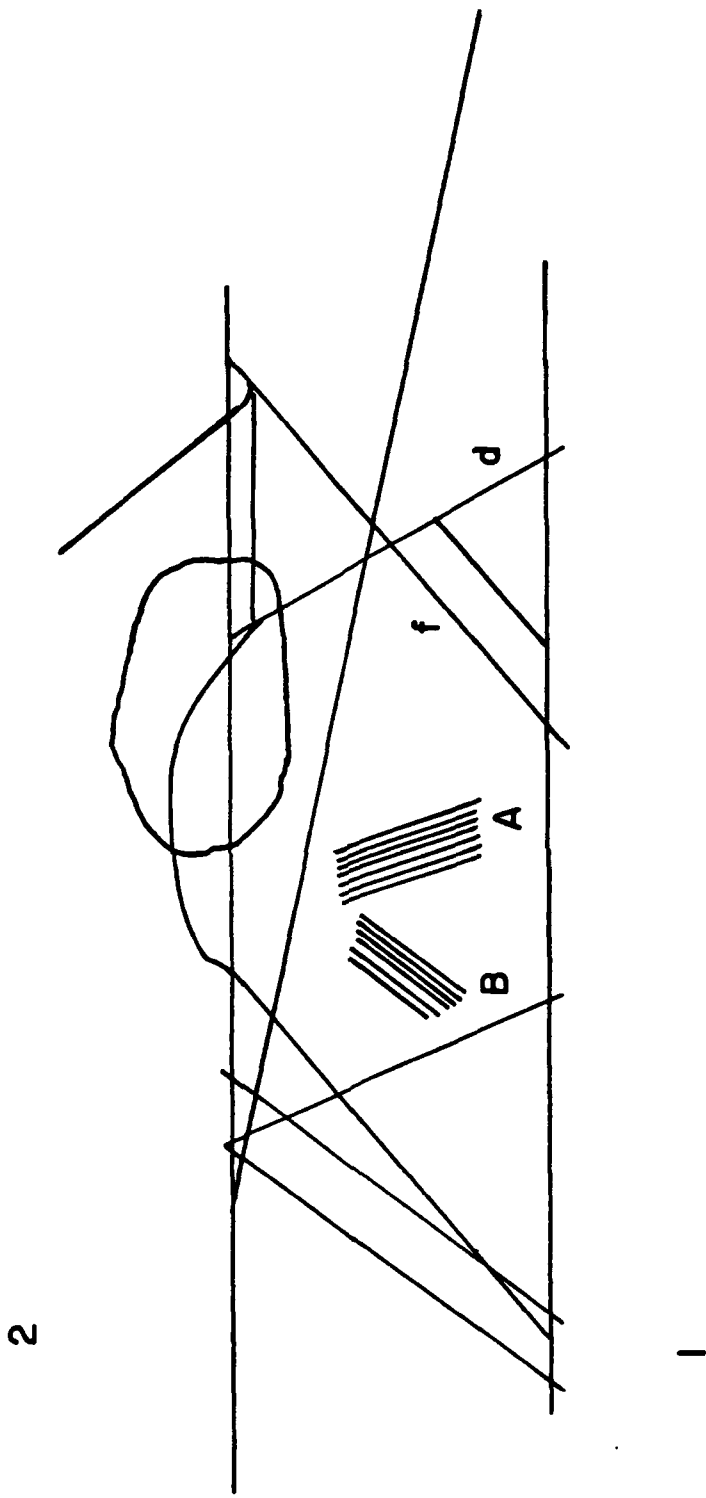


FIGURE 15. Schematic of grain boundary 1.

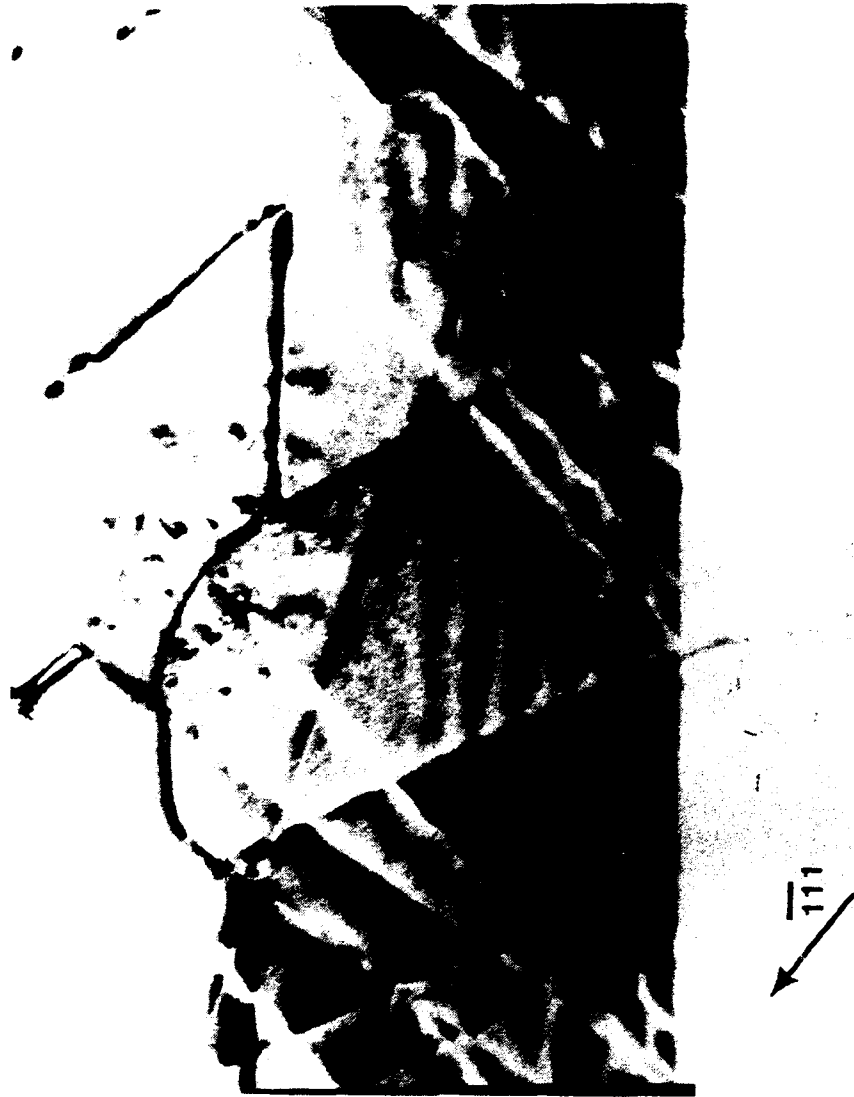


FIGURE 16. Bright-field (BF) micrograph of boundary 1. Set A visible.



FIGURE 17. BF micrograph, gb 1. Set A visible.



FIGURE 18. Dark-field (DF) micrograph, gb 1. Set A and B visible.



FIGURE 19. DF micrograph, boundary 1. Set B visible.



FIGURE 20. BF micrograph, boundary 1. Dislocation emission or absorption.

In this case, the primitive cubic (pc, or p) and face centered cubic (fc, fcc, or f) basis vectors differ only in that two of the three fc vectors are half the length of the pc case. Both sets of vectors may be found in Table 3. The important experimental and calculated characteristics of the boundary and the solution are summarized in Table 4. The only distinctions between pc and bc solutions is the spacing of set B. In the pc case, the spacing is 1.7 nm, which is in poor agreement with observation in the fc case it is 8.5 nm, which is in worse agreement. The agreement in line direction is excellent in both cases, as is the spacing of set A. The spacing of set B is in poor agreement.

The results of the $g \cdot b$ analysis for the Burgers vectors determined to be the best match are summarized in Table 5. The agreement is very poor, therefore the assignment of vectors will be discussed in somewhat more detail. Complete solutions were developed for both pc and fc lattices for each rotation. The predicted line directions were compared to the experimental values and any viable solutions identified. The $g \cdot b$ Burgers vector analysis was performed for all vectors of all rotations providing a viable solution, and for at least the pc and fc basis vectors of all rotations considered. In this case, all vectors of $\Sigma 31$ and $\Sigma 21$ were considered. No pair of vectors from a single solution were found to be consistent with the $g \cdot b$ analysis. Since the Burgers vector analysis is ambiguous and the result above is

TABLE 3

 $\Sigma = 31b$ DSC Vectors

Primitive Cubic (Ordered)

$$b_1 = a/31 [7 \ 2 \ 3] \quad b_2 = a/31 [2 \ 5 \ -8] \quad b_{31} = a/31 [-8 \ 11 \ 1]$$

$$b_{32} = a/31 [-1 \ 13 \ 4] \quad b_{33} = a/31 [-10 \ 6 \ 9] \quad b_{34} = a/31 [-3 \ 8 \ 12]$$

Face-centered Cubic (Disordered)

$$b_1 = a/62 [7 \ 2 \ 3] \quad b_2 = a/62 [4 \ 10 \ -16] \quad b_{31} = a/62 [-8 \ 11 \ 1]$$

$$b_{32} = a/62 [-1 \ 13 \ 4] \quad b_{33} = a/62 [-15 \ 9 \ -2] \quad b_{34} = a/62 [-12 \ 1 \ 17]$$

TABLE 4

Characteristics of Grain Boundary 1, $\Sigma = 31b$

Experimental angle/axis:	$53.684^\circ \pm 0.6^\circ / [-.4142 \ .7842 \ .4621]$
$\Sigma = 31b$ angle/axis:	$52.190^\circ / [-1 \ 2 \ 1]$
$R(02)$:	$3.561^\circ \pm 0.25^\circ / [.1288 \ .0154 \ .9887] \pm 3.0^\circ$
Boundary Normal:	$\hat{v} = [-.6277 \ .5446 \ .5563] \pm 6.0^\circ$

GRAIN BOUNDARY DISLOCATIONS

	Experimental	Calculated	
Difference			
Set A			
Line Direction:	[.754 .595 .267]	[.748 .619 .237]	$\Delta r = 2.2^\circ$
Spacing:	6.7 nm	6.3 nm	$\Delta S = 0.5 \text{ nm}$
		$b = a/31 [2 \ 5 \ -8]$	
Set B			
Line Direction:	[.659 -.009 .752]	[.671 .016 .741]	$\Delta r = 1.7^\circ$
Spacing:	8.5 nm	1.7 nm	$\Delta S = 7.2 \text{ nm}$
		$b = a/31 [7 \ 2 \ 3]$	

TABLE 5

Summary of $g \cdot b$ Analyses, Grain Boundary 1Crystal 2, $\underline{b}_A = [4 \ 10 \ -16]_2$, $\underline{r} = [.754 \ .595 \ .267]$

g	$g \cdot b$	$g \cdot b_e$	$g \cdot b_{xr}$	A
-1-1 1	-.48	-.41	-.07	S*
-1 1-1	.36	.39	-.33	O
2 0 0	.13	.02	.41	S
0 0 2	-.52	-.56	-.16	O

Crystal 1, $\underline{b}_A = [16 \ 10 \ -4]_1$, $\underline{r} = [.40 \ .140 \ .90]$

-1 1-1	-.03	-.05	-.39	W
2 0 0	.52	.46	.31	S
-1-1 1	-.48	-.51	.08	M
0 2 0	.32	.30	-.52	O

Crystal 2, $\underline{b}_B = [7 \ 2 \ 3]_2$, $\underline{r} = [.659 \ -.009 \ .752]$

g	$g \cdot b$	$g \cdot b_e$	$g \cdot b_{xr}$	B
-1-1 1	-.19	-.22	.02	O
2 0 0	.45	.17	.1	W

Crystal 1, $\underline{b}_B = [3-2 \ 7]_1$, $\underline{r} = [-.119 \ -.461 \ .883]$

-1 1-1	-.39	-.12	-.11	S
2 0 0	.19	.25	.1	O
-1-1 1	.19	-.12	.01	O
0 2 0	-.13	.07	-.22	S

*S = Strong, M = Medium, W = Weak, O = Extinct

in good agreement with the geometric structure of the boundary, it is taken as the probable solution.

The adoption of this solution requires the conclusion that $\underline{g \cdot b}$ analysis for gbds in Ni_3Al is unreliable. Such analysis is, in general, more problematical than $\underline{g \cdot b}$ analysis in the lattice. The extension of the dynamical theory to grain boundaries requires additional assumptions and imposes additional experimental constraints. The principal one is that one grain be strongly diffracting in the two-beam condition while the other is very weakly diffracting such that it can be considered a weak absorber.⁶¹ Nonetheless, as noted in Chapter II, reasonable agreement has been obtained in other systems.

There are several properties of Ni_3Al however, which may contribute to the problem. The first is that it is elastically anisotropic. It seems reasonable that in any but symmetric boundaries, a distortion in the strain field of the gbd might be introduced as a result of the different elastic properties of each crystal in the plane of the boundary. Such a distortion would not be adequately accounted for by consideration of $\underline{g \cdot b_e}$ and $\underline{g \cdot b_{xu}}$. Image simulation would seem the most promising approach.

Secondly, as discussed in Chapters IV and VI, there is evidence that there are chemical effects at the grain boundary. Chemical effects at gbds in asymmetrical boundaries might also be expected to be anisotropic and to cause changes in the image.

3.3 Grain Boundary 2, $\Sigma = 9$

The major relevant features of the boundary in Fig. 21 are indicated in the schematic of Fig. 22. There are a number of extrinsic boundary dislocations including those labeled E, and two pile-ups in crystal 2, labeled G. Of principal interest are the intrinsic boundary dislocations. Set A is clearly visible in Figs. 21 and 23-26. Set B is faintly visible in a few diffraction conditions (Figs. 23, 25, 27), and a possible third set parallel to the thickness fringes is suggested by the contrast in Figs. 24 and 25.

The misorientation as calculated from the stereographic projection was $40.4 \pm 3^\circ$ about $\hat{u} = [.05 \ .58 \ -.81]$. The more precise misorientation obtained using method 1 of Section 3.2 was $42.776^\circ \pm 0.164^\circ$ about $\hat{u} = [.0289 \ .6201 \ -.7839] \pm 1.2^\circ$. The difference of 2.4° in rotation and 3.2° in axis is typical of the uncertainty in stereographic plotting and measuring. The boundary could be tilted edge-on, so the boundary normal was found by trace analysis. The most likely CSL relationships are the $[01\bar{1}]$ rotations $\Sigma = 9$, 38.94° ; $\Sigma = 57c$, 43.99° ; and $\Sigma = 59b$, 45.98° (Table 6). Complete solutions were developed for ordered and disordered CSL's of each type, as in Sections 3.2 and 3.1.5. The Burgers vectors are listed in Tables 7, 8, 9.

None of the trial CSL's yielded a line direction consistent with the possible set C. All of them gave a line direction within 4° of B. Both $\Sigma = 57$ and the disordered $\Sigma = 59$ yield line directions for A



FIGURE 21. BF micrograph, boundary 2. Set A visible.

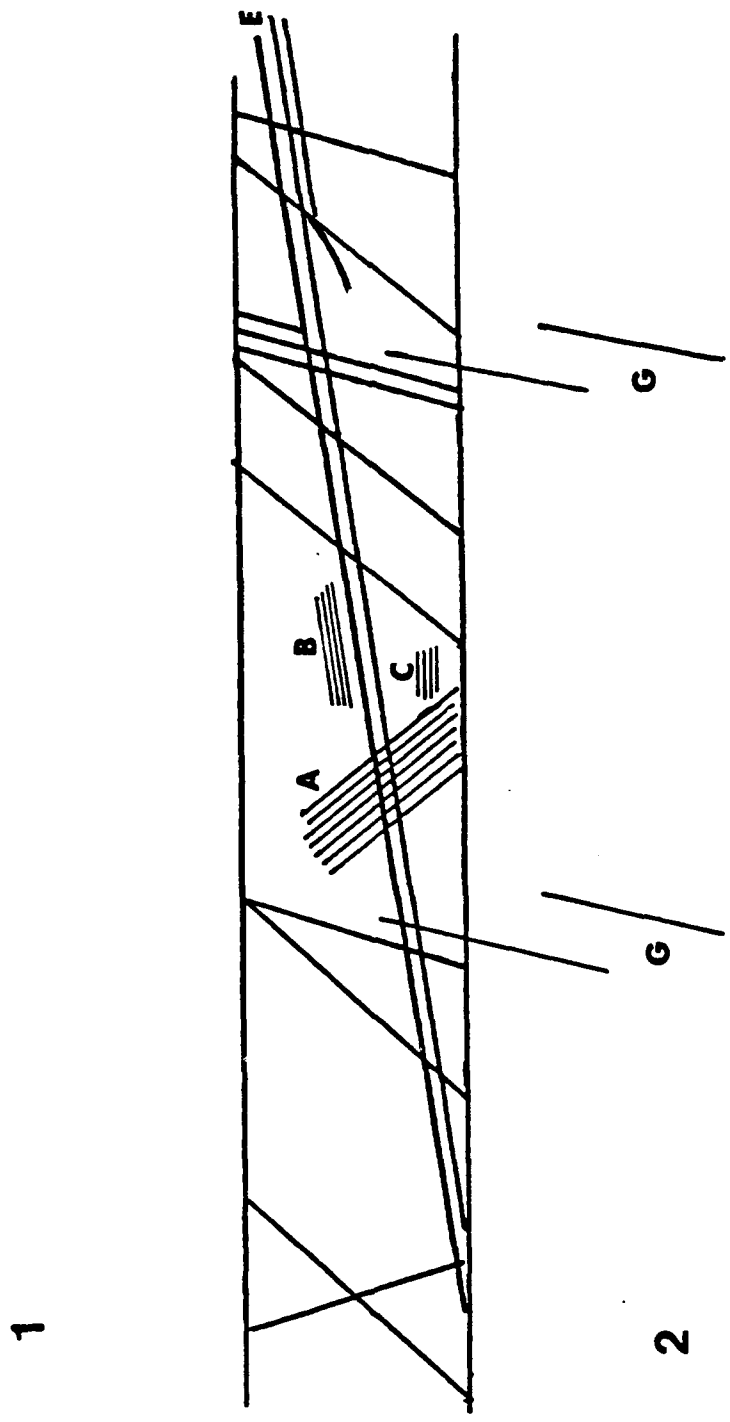


FIGURE 22. Schematic diagram of boundary 2.



FIGURE 23. BF micrograph, boundary 2. Set A visible.



FIGURE 24. BF micrograph, boundary 2. Set A visible.



FIGURE 25. BF micrograph. Set A visible.



FIGURE 26. Weak-beam dark-field (WB) micrograph of boundary 2. Set A visible.



FIGURE 27. DF micrograph of boundary 2. Set C visible.

TABLE 6

Possible Misorientations of Grain Boundary 2

Experimental angle/axis: $42.776 \pm 0.164^\circ / [0.0289 \ .6201 \ .\overline{7839}] \pm 1.17^\circ$

$\Sigma 9$ $38.94^\circ / [01\bar{1}]$

$\underline{R}(02)$ $6.126 \pm 0.164^\circ / [0.\overline{078} \ .\overline{163} \ .\overline{984}]$

$\Sigma 57c$ $43.99 / [01\bar{1}]$

$R(02)$ $5.212 \pm 0.164^\circ / [0.\overline{133} \ .\overline{875} \ .\overline{466}]$

$\Sigma 59b$ $45.98 / [01\bar{1}]$

$R(02)$ $6.084 \pm 0.164^\circ / [0.\overline{128} \ .\overline{977} \ .\overline{169}]$

TABLE 7
 $\Sigma = 9$ DSC Vectors
 (38.94° [01 $\bar{1}$])

$$b_1 = a/9 [\bar{4}11] \quad b_2 = a/9 [122] \quad b_{31} = a/9 [\bar{2}5\bar{4}]$$

$$b_{32} = a/9 [24\bar{5}] \quad b_{33} = a/9 [\bar{1}7\bar{2}] \quad b_{34} = a/9 [\bar{3}3\bar{6}]$$

Face-Centered Cubic (Disordered)

$$b_1 = a/18 [\bar{4}11] \quad b_2 = a/9 [122] \quad b_{31} = a/18 [\bar{3}3\bar{6}]$$

$$b_{32} = a/18 [12\bar{7}] \quad b_{33} = a/18 [\bar{1}7\bar{2}] \quad b_{34} = a/18 [36\bar{3}]$$

TABLE 8

 $\Sigma = 57c$ DSC Vectors(43.99°, [01 $\bar{1}$])

$b_1 = a/57 [477]$

$b_2 = a/57 [7\bar{2}\bar{2}]$

$b_{31} = a/57 [9\ 30\ \bar{2}7]$

$b_{32} = a/57 [5\ 23\ \bar{3}4]$

$b_{33} = a/57 [2\ 32\ \bar{2}5]$

$b_{34} = a/57 [\bar{2}\ 25\ \bar{3}2]$

Face-Centered Cubic (Disordered)

$b_1 = a/114 [477]$

$b_2 = a/57 [2\bar{2}\bar{2}]$

$b_{31} = a/114 [9\ 30\ \bar{2}7]$

$b_{32} = a/114 [5\ 23\ \bar{3}4]$

$b_{33} = a/114 [\bar{5}\ 34\ \bar{2}3]$

$b_{34} = a/114 [\bar{9}\ 27\ \bar{3}0]$

TABLE 9

 $\Sigma = 59b$ DSC Vectors(45.98°, [01 $\bar{1}$])

Primitive Cubic (Ordered)

$$b_1 = a/59 [\bar{1}0 \ 3 \ 3] \quad b_2 = a/59 [355] \quad b_{31} = a/59 [\bar{1}5 \ 34 \ \bar{2}5]$$

$$b_{32} = a/59 [\bar{5} \ 31 \ \bar{2}8] \quad b_{33} = a/59 [\bar{8} \ 26 \ \bar{3}3] \quad b_{34} = a/59 [\bar{2} \ 36 \ \bar{2}3]$$

Face-Centered Cubic (Disordered)

$$b_1 = a/118 [\bar{1}0 \ 3 \ 3] \quad b_2 = a/59 [10 \ 10 \ \bar{5}] \quad b_{31} = a/118 [\bar{5} \ 31 \ \bar{2}8]$$

$$b_{32} = a/118 [\bar{9} \ 44 \ \bar{1}5] \quad b_{33} = a/118 [\bar{2}1 \ 24 \ \bar{3}5] \quad b_{34} = a/118 [\bar{1}1 \ 21 \ \bar{3}8]$$

disagreeing by $> 18^\circ$, and were discarded. The major results of the remaining three solutions are summarized in Table 10. The solutions for line direction in the ordered and disordered $\Sigma = 9$ are identical and are significantly better than the $\Sigma = 59$ solution. The spacings are not unreasonable in all three cases given the associated uncertainty. However, the agreement is quite good in the case of $\Sigma = 9(p)$.

In the case of set A, the Burgers vectors are so similar that they are indistinguishable by $\underline{g \cdot b}$ analysis. The results for one of the possible A's, set A, the three possible B's, and set B are listed in Table 11. Only those reflections which produce images with sufficient quality to definitively identify extinction conditions are listed. The results in crystal 1 are consistent for set A. Possible for set B are $1/9 [36\bar{3}]$ and $1/59 [\bar{8} 26 3\bar{5}]$, the others are unlikely. The results for crystal 2 are less informative, yielding no firm indications. The lattice dislocations, set G, are $[011](1\ 1\ \bar{1})$. Note that the slip plane is viewed nearly edge-on in Fig. 26 yet the apparent spacing between superpartials is 8.3 nm. It is probable that they are dissociated on either (100) or (001).

The best solution for the boundary is the ordered $\Sigma = 9$ solution. The boundary solution is in excellent agreement while the $\underline{g \cdot b}$ analysis is in fair agreement. In the case of boundary 1, the $\underline{g \cdot b}$ analysis was inconsistent with any solution set, yet there was a geometrical solution in excellent agreement with experiment. Here again, the geometrical analysis yields a solution(s) in excellent agreement with experiment, which lends additional credence to those results. While

TABLE 10

Possible Dislocation Sets, Grain Boundary 2

$$\Delta r, \Delta S = |\text{experimental-calculated}|$$

Set A

Σ	\underline{b}	\hat{r}	$\hat{\Delta r} (^{\circ})$	S(nm)	$\Delta S(\text{nm})$
Exp.	A	[.495 .358 .799]		5.6	
9_p	$\frac{1}{9}$ [122]	[.508 .420 .752]	5	5.7	0.1
9_f	$\frac{1}{9}$ [122]	[.508 .420 .752]	5	5.7	0.1
59_p	$\frac{1}{59}$ [355]	[.521 .495 .695]	10	2.0	3.6

Set B

Σ	\underline{b}	\hat{r}	$\hat{\Delta r} (^{\circ})$	S(nm)	$\Delta S(\text{nm})$
Exp.	B	[.026̄ .682̄ .737]		5.3	
9_p	$\frac{1}{9}$ [363̄]	[.008 .650̄ .760]	2	6.4	1.1
9_f	$\frac{1}{18}$ [172̄]	[.008 .650̄ .760]	2	3.2	2.5
59_p	$\frac{1}{59}$ [8̄ 26̄ 33̄]	[.015 .641̄ .767]	4	7.3	2.0

TABLE 11

Summary of $g \cdot b$ Analysis

CR1	g	b	$\frac{1}{9}[\bar{1}7\bar{2}]$	$\frac{1}{9}[122]$	$\frac{1}{59}[\bar{8} 26 \bar{3}\bar{3}]$	$\frac{1}{9}[36\bar{3}]$	IMAGE*	
							A	B
					$g \cdot b$			
	$\bar{1}\bar{1}1$		0.9	0.1	0.9	1.3	O	W
	$1\bar{1}\bar{1}$		0.7	0.3		0	S	O
	$0\bar{2}0$		1.6	0.4	0.9	1.3	S	W
CR2	g	b	$\frac{1}{9}[\bar{3}6\bar{3}]$	$\frac{1}{9}[\bar{1}22]$	$\frac{1}{59}[\bar{2} 23 \bar{3}\bar{6}]$	$\frac{1}{9}[17\bar{2}]$	IMAGE*	
							A	B
					$g \cdot b$			
	$\bar{1}\bar{1}1$		0.7	0.1	1	1.1	S	O
	$02\bar{2}$		2	0	2	2	M	O
	$1\bar{1}\bar{1}$		0.7	0.6	1.2	0.4	S	O
	020		1.3	0.4	0.8	1.6	S	O

* S = Strong, M = Medium, W = Weak, O = Extinct

the g·b analysis approaches the level of agreement expected for such analyses, it is still not convincing.

CHAPTER IV

DEFORMATION IN Ni_3Al : BACKGROUND AND THEORY

There are several unusual aspects to the deformation behavior of Ni_3Al . The experimental results, as reported in the literature and detailed in approximate chronological order below, are summarized as follows: 1. The flow stress (strain $> 10^{-3}$) increases with increasing temperature to a peak at about 700°C and decreases with increasing temperature above 700°C .⁶⁶ 2. The microyield stress (strain $< 10^{-5}$) is nearly independent of temperature.⁶⁷ 3. Below the peak temperature the dominant slip systems are $\langle 110 \rangle \langle 111 \rangle$, while above the peak temperature the dominant systems are $\langle 110 \rangle (100)$.⁶⁸ 4. The yield stress is highest for orientations with the highest resolved shear stresses on cube cross-slip planes.⁶⁹ 5. The tension and compression yield stresses are generally different. The sign and magnitude depend upon orientation.⁷⁰ 6. The magnitude of the peak in yield stress with temperature increases with increasing Al. 7. A major feature of deformed specimens is a high proportion of long, straight screw or near-screw dislocations.⁴

The unusual temperature dependence of yield strength (increasing yield strength with increasing temperature) of Ni_3Al and some other

$L1_2$ compounds has been the object of numerous theoretical and experimental studies.⁶⁶ One of the earliest of these was the work of Flinn,⁷¹ who first suggested dissociation of the $a\langle 110 \rangle$ superdislocation on other than the slip plane might be the responsible mechanism. The APB energy was calculated for various planes and found to be lower on {001} cube planes than on {111} octahedral planes (later confirmed by experiment⁷²). Based upon that observation, he proposed that the dissociation plane (of a dislocation of any character) shifted from {111} to {100} by diffusional climb. Kear and Wilsdorf⁷³ proposed cross-slip into the same configuration to account for high strain hardening in Cu_3Au . They were also the first to find the dislocation structure to be predominately long straight screw dislocations. Davies and Stoloff⁷⁴ found the yield stress to increase continuously from $-196^\circ C$ to $600^\circ C$ and concluded that a diffusion controlled mechanism (Flinn's) was inappropriate. Copley and Kear⁶⁸ first reported a ductility minimum at $810^\circ C$, and attempted to explain all observations by a lattice resistance (Pierls stress) argument.

Thornton, et al.⁶⁷ discovered that the yield stress is independent of temperature for very small strains (micro-yield). They were also the first to suggest the Kear-Wilsdorf variation of Flinn's locking mechanism as the cause of the anomalous temperature dependence of yield stress. Takeuchi and Kuramoto⁶⁹ further clarified the phenomenon by determining that the magnitude of the temperature dependence increases with increasing component of the stress on the {001}

cross-slip plane. They refined the model with a quantitative treatment based upon the number of cross-slipped segments as a function of cross-slip stress and temperature. Lall, et al.³⁸ found a somewhat different orientation dependence than predicted by Takeuchi and Kuramoto⁶⁹ and attributed the effect to the constriction or separation of the Schockley partials either aiding or hindering cross-slip, depending upon the orientation.

The appearance of the companion papers of Yamaguchi, et al. and Paidar, et al.^{75,76} were something of a landmark in that the further refinement of the cross-slip model was based on atomistic calculations of dislocation core structures. The calculations (utilizing assumed model potentials) indicated that the $1/2 \langle 110 \rangle$ superpartial dissociates in a planar fashion in either the plane of the APB or an intersecting $\{111\}$ plane. The former is expected to be glissile. The $1/3 \langle 112 \rangle$ superpartial was predicted to dissociate into one of three variants of near equal energy, two of which are sessile and the third reverts to one of the first two under stress. They noted that different potentials might yield fewer stable structures, perhaps allowing the potentially glissile variant to remain glissile. Later core structure calculations for very high APB energies by Tichy, Vitek and Pope have been in general agreement.^{77,78} (However, the recent calculation of Farkas and Savino using local volume dependent potentials finds the core of the $1/2 \langle 110 \rangle$ always dissociated in a $\{111\}$ plane other than that of the APB.) In any event, this study provided the missing element in the model, i.e., a reason for the dislocation

to be sessile after cross-slip. As outlined in Paidar, Pope and Vitek,⁷⁹ the leading $1/2 \langle 110 \rangle$ superpartial constricts under applied stress and thermal activation, then cross-slips onto $\{100\}$ and immediately redissociates onto a $\{111\}$ plane. Both superpartials are then dissociated on (possibly different) $\{111\}$ planes, and are separated by an APB on $\{100\}$. The tendency for this to happen increases with increasing cross-slip stress and increasing temperature. The yield stress depends upon the sign of the stress due to the different resolved stress constricting the Shockley partials, in agreement with experiment.⁷⁰ Yoo has developed a model in which the driving force for the cross-slip is a torque exerted by the superpartials on one another as a result of elastic anisotropy.^{80,81} The most notable difference regarding operation of the mechanism is that the model predicts a torque, i.e., a driving force for cross-slip in addition to APB energy, even when the cross slip stress is zero.

While the cross-slip model has evolved to a highly sophisticated state and explains the majority of observed macroscopic behavior, there are several remaining issues. Veyssiere, et al. has observed dissociation onto $\{100\}$ planes which appears to have occurred by diffusion.^{82,83} Paidar has calculated the structures and energies of various APB's and predicts that some are non-planar.⁸⁴ He interprets this to support a diffusional dissociation model (the original model of Flinn). Veyssiere, et al. have also observed evidence of drag of APB's during deformation at 650°C .⁸⁵

Another matter that deserves further consideration is the role of $1/3 \langle 112 \rangle$ superpartials. Early in this work it became apparent that stacking fault coupled dislocations were a common feature in binary alloys, but rare in the literature.⁸⁶ Subsequently there have been several reports of profuse stacking faults.^{87,88} Baker and Schulson have observed pairs of $\{112\}$ dislocations bounding narrow stacking faults, many of which have been loops.^{89,90}

The third issue that has received little attention is the role of B in the lattice. With only a few recent exceptions, the role of B in ductilizing Ni_3Al has been assumed to be exclusively an effect upon grain boundary cohesion. It was evident early in the course of this work, and has recently been reported, that there are significant effects upon surface energies and upon the dislocation population, specifically, that relatively small amounts of B completely eliminated the otherwise common stacking fault coupled pairs.⁹¹

CHAPTER V
DEFORMATION IN Ni_3Al : EXPERIMENTS

5.1 Experimental Procedures

5.1.1 Specimen Preparation

Specimen preparation was as described in Section 3.1.1 with the addition of compression testing to introduce unrecovered deformation. Compression test specimens were made by sawing blocks 3x3x6 mm. These were polished on all sides and compressed along the long axis at a crosshead speed of 0.001 in./min. to approximately 5% strain at 23°C. Foils for TEM analysis were sawn perpendicular to the stress axis, and polished as described in Section 3.1.1.

5.1.2 Fault Analysis and the Magnitude of 112 Burgers Vectors

TEM examination was accomplished utilizing JEOL 100CX, 200CX, and 2000FX microscopes. Analysis to determine the orientation of the fault vector \underline{R} was accomplished in the usual fashion utilizing the criterion of invisibility when $\underline{g} \cdot \underline{R} = 0, 1, 2, \dots$ (essentially $\underline{g} \cdot \underline{R} = 0$ since all \underline{g} 's used for fault analysis yield $\underline{g} \cdot \underline{R} = n/3$, $n = 0, 1, 2, \dots$). There are two likely possibilities for the magnitudes of vectors of

the type $\langle 112 \rangle$: $1/6 \langle 112 \rangle$ Shockley partial dislocations or $1/3 \langle 112 \rangle$ superpartials. The magnitudes were assigned in the following manner. It is known that Burgers vectors of the type $1/6 \langle 112 \rangle$ are invisible for diffracting vectors yielding $\underline{g} \cdot \underline{b} = 1/3$. (Hence the invisibility of closely dissociated Shockley partials for diffracting vectors which yield $\underline{g} \cdot \underline{b}(\text{total}) = 0$, where $\underline{b}(\text{total})$ is the Burgers vector of the total dislocation of $\langle 110 \rangle$ type.) They are not generally invisible for $\underline{g} \cdot \underline{b} = 2/3$. Therefore, dislocations which were visible for \underline{g} 's which would yield $\underline{g} \cdot \underline{b} = 1/3$ for $\underline{b} = 1/6 \langle 112 \rangle$ were taken to be $1/3 \langle 112 \rangle$.

5.1.3 Annealing Twins, Grain Size and Chemistry

The incidence of annealing twins and the grain size were determined from optical micrographs of three randomly selected areas in each of five materials. The line-intercept technique was used to determine the numbers of twin and grain boundaries in each image. Boundaries which appeared to be perfectly straight or composed of straight segments were assumed to be twins. The uncertainty (standard deviation) in twin frequency averaged about 25%.

The bulk chemistry was determined by wet chemical and vacuum fusion techniques. The chemistry and degree of homogeneity were also determined by wavelength dispersive X-ray analysis of seven to ten spots in different areas of the forging. The total uncertainty (one

standard deviation about the mean of the composition) was found to be about 0.4 at.% Al. That is a reasonable value for the precision of the technique. The accuracy is very dependent upon the choice and quality of standards and requires particular care when dealing with compounds. Nonetheless, using elemental standards, the results typically agreed with the bulk analyses within 0.5 at.% Al.

5.2 Results

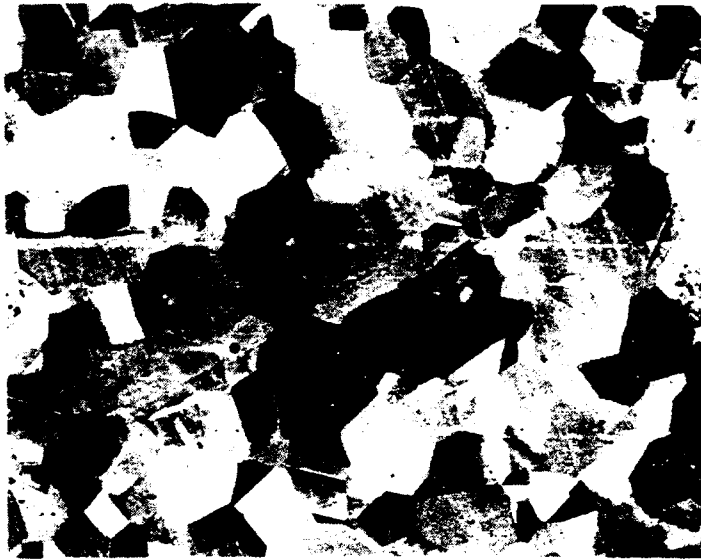
The specimens were found to have approximately equiaxed grains, were generally free of inclusions and were mostly well annealed in the as-annealed condition. However, there were occasional grains which evidenced high densities of dislocations--presumed to be artifacts of forging.

5.2.1 Frequency of Annealing Twins and Grain Size

The addition of B was found to have a strong effect upon both the fraction of twin boundaries and grain size (Fig. 28). The ratio of twin to grain boundaries decreases linearly from 0.24 to 0.05 with the addition of 0.5 and 1.0 at.% B. There are also significant differences in the kinetics of grain growth. After identical processing (described above), the mean grain size increases linearly by a factor of three with the addition of 0.5 and 1.0 at.% B. Both phenomena are illustrated in the plot of Fig. 29.



Ni-24.5Al 0.5B



Ni-24.5 Al

FIGURE 28. Grain structure in Ni-24.5 Al with and without B.

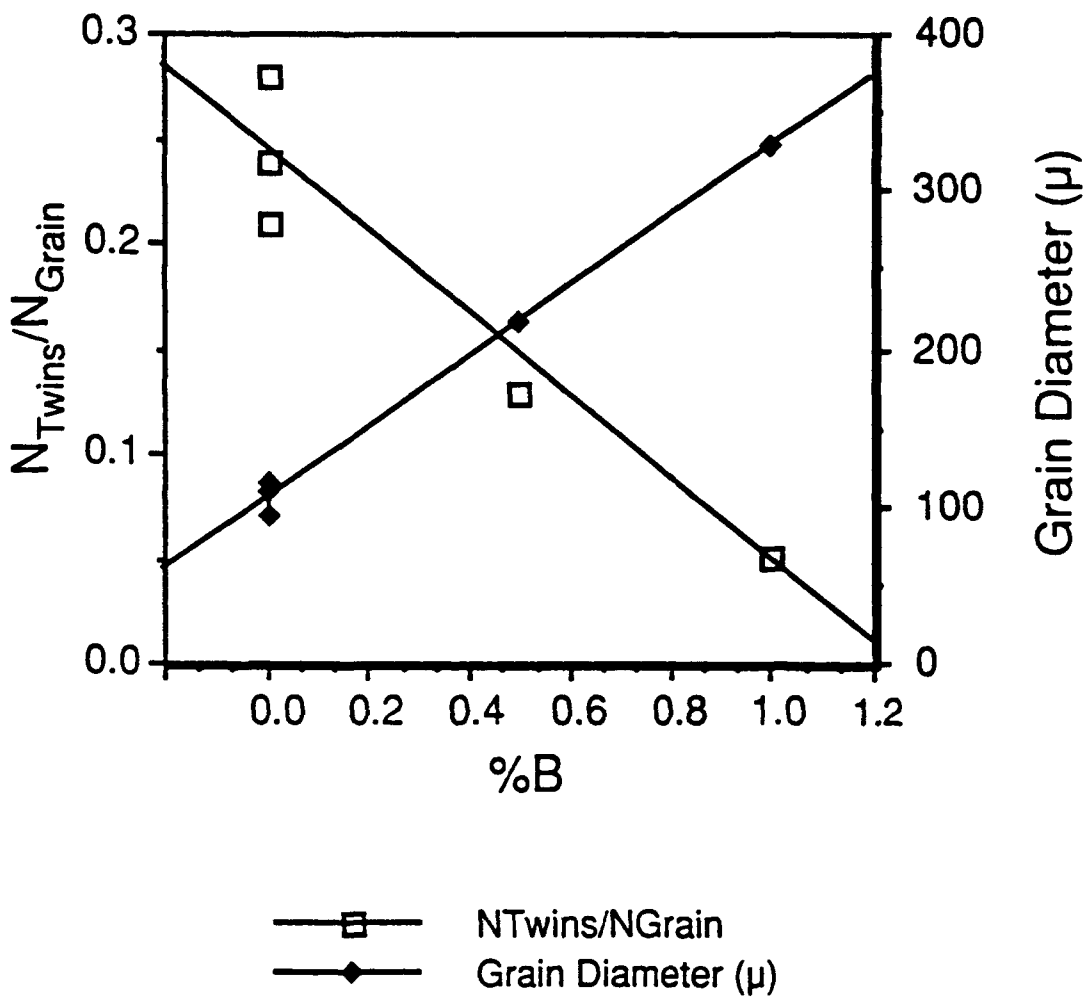


FIGURE 29. Effect of B on twin frequency and grain size.

5.2.2 Dislocations and Stacking Faults

The most obvious feature of the dislocation structures observed in binary alloys is the common appearance of stacking fault contrast between pairs of dislocations. Such contrast commonly appears between closely spaced parallel dislocations throughout some, but not all, grains (Figs. 30 and 31). In addition, there are occasional extended faults such as in Fig. 32. In one specimen, the bounding dislocations are completely dissociated and the faults extend over distances on the order of the grain size, as in Fig. 33. Such faults are completely absent in compositions containing B.

The configuration of Fig. 34 was found in Ni-24.5Al as-annealed. The fault is invisible in Fig. 35, clearly revealing the bounding dislocations. The fault and each of the dislocations, in turn, are invisible in Figs. 36 and 37. The result of the $g \cdot b$ analysis is shown in Table 12 and summarized in Fig. 38. The undissociated superdislocation is determined to be $[\bar{1} 0 1]$, while the superpartials are $1/3 [\bar{1}12]$ and $1/3 [\bar{2}11]$. The fault is of the type $[111]$. The partials in the widely dissociated region lie along $\langle 110 \rangle$ directions. The weak-beam image of Fig. 39 reveals small "tongues" along the $1/3 [\bar{1}\bar{1}2]$ dislocation in the narrowly dissociated region which suggest an additional reaction, perhaps further dissociation of the superpartial with reorientation of one of the $1/6 \langle 112 \rangle$ Shockley partials along $\langle 110 \rangle$ directions.

TABLE 12

Summary of $g \cdot b$ Analysis, SF1

g	b	a	b	c	d	e	SF	1/3	1/3	1/2	1/2	1/3
								$\frac{1}{2}$	$\frac{2}{1}$	$\frac{1}{1}$	$\frac{1}{1}$	$\frac{1}{1}$
Number of images							$g \cdot b$					
$1\bar{1}1$		1	1	1	0	1	1	-2/3	+2/3	0	+2	1/3
200		1	1	2	1	2	1	+2/3	+4/3	1	1	2/3
$\bar{1}\bar{1}1$		2	2	0	1	0	1	-4/3	-2/3	-2	0	-1/3
$02\bar{2}$		1	0	0	1	2	0	2	0	1	-1	0
020		2	2	2	0	2	1	2/3	-2/3	0	-1	2/3
$2\bar{2}0$		0	1	1	1	2	0	0	2	1	2	0
220		1	1	1	1	0	1	2/3	2/3	1	0	4/3
$\bar{2}\bar{2}0$		1	1	0	1	0	1	-2/3	-2/3	-1	0	-4/3
$\bar{2}02$		1	1	1	1	w	0	-2	-2	-1	-1	0
$3\bar{1}1$		0	1	1	1	2	0	0	2	1	-2	1



FIGURE 30. Typical SISF coupled pairs.



FIGURE 31. Typical SISF coupled pairs.



FIGURE 32. Typical extended SISF.



FIGURE 33. High density of extended faults and SISF debris.

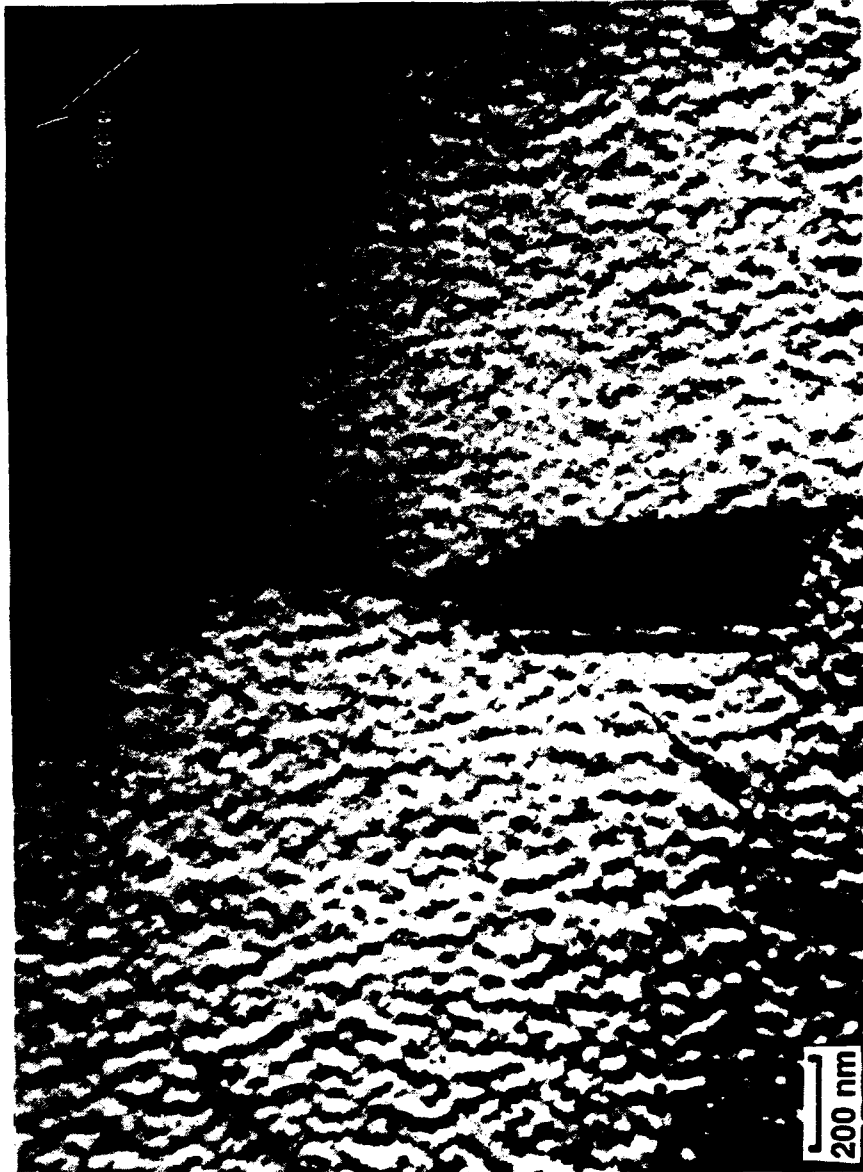


FIGURE 34. Extended SISF.



FIGURE 35. Bounding dislocations visible, fault invisible.

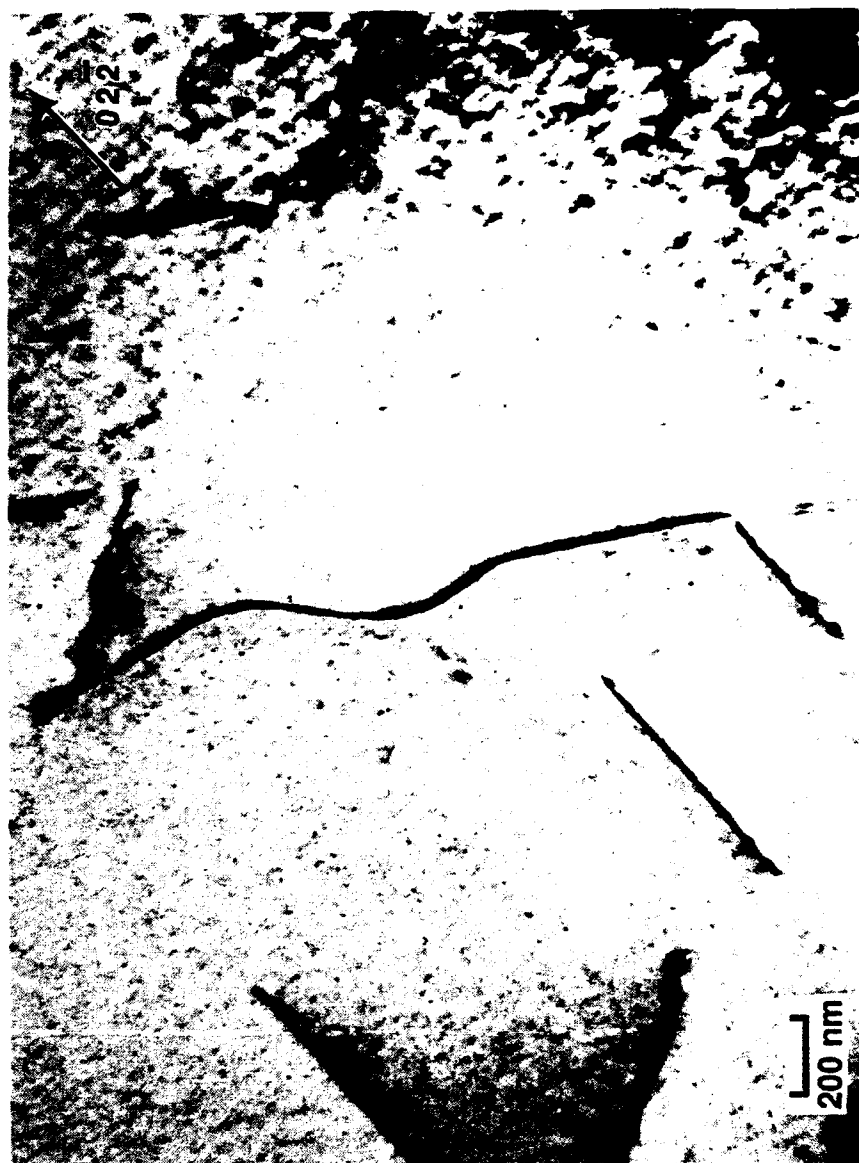


FIGURE 36. One bounding dislocation invisible.



FIGURE 37. The second bounding dislocation invisible.

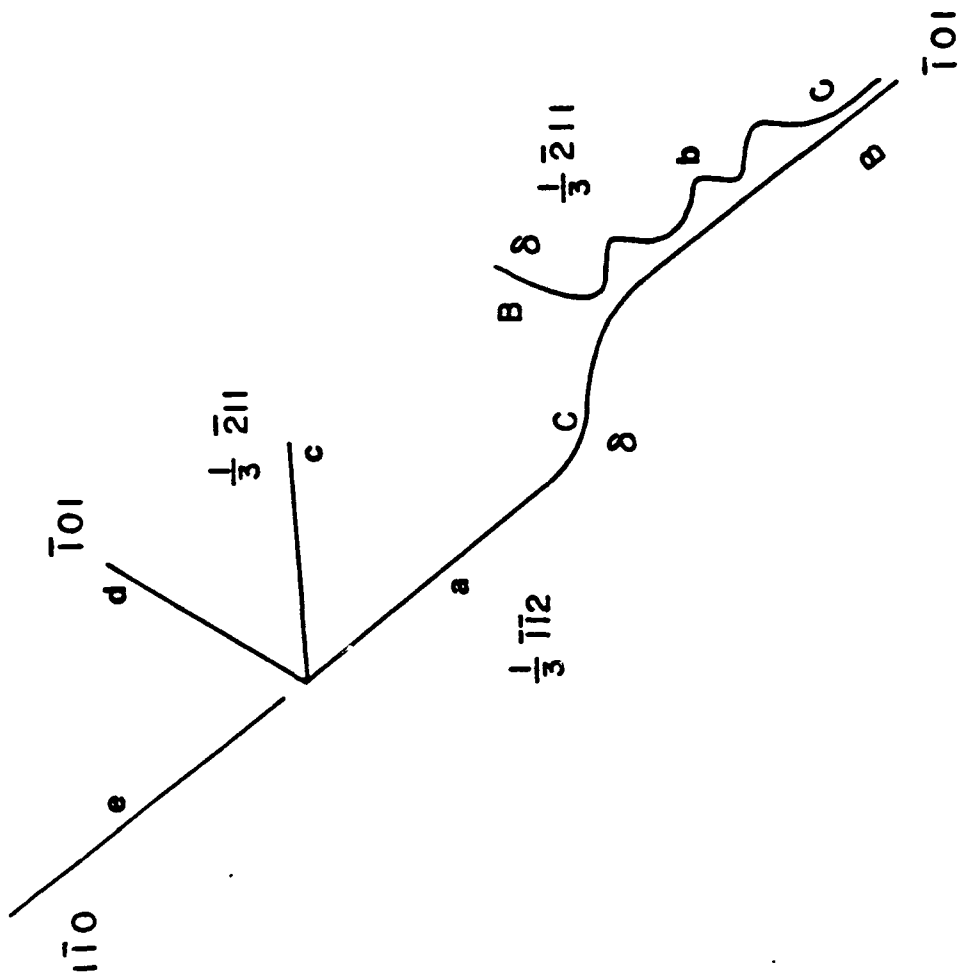


FIGURE 38. Schematic of extended fault 1.



FIGURE 39. WB image of extended fault 1.

Although the overall appearance of the fault of Fig. 40 (Ni-24.5 Al, $\epsilon = -4\%$, 23°C) is different from the previous one, the major features are quite similar. There is a complex interaction with another dislocation(s) to the left of the extended fault region. The region considered here is to the right of the interaction. The bounding dislocations are clearly evident in Fig. 41 and the weak-beam of Fig. 42. The bounding dislocations and the $[\bar{1}\bar{1}0]$ superdislocation are out of contrast in Figs. 43 and 44 and Fig. 45 in turn. The g.b analysis is summarized in Table 13 and the configuration in the schematic Fig. 46. The superdislocation is of type $[\bar{1}\bar{1}0]$ and is in pure screw orientation. The superpartials bounding the fault are $1/3 [\bar{1}\bar{2}1]$ and $1/3 [2\bar{1}\bar{1}]$ and lie along $\langle 110 \rangle$ directions. The consistent spacing of the $[\bar{1}\bar{1}0]$ superdislocation pair in the tg images of Fig. 47 indicates that they are a pair and not a dipole.

A short distance from the left end of this faulted line (L in Fig. 46) is a small, complex interaction between two (or more) dislocations consisting of three segments (Figs. 46, 48, and 49). The g.b analysis is inconsistent with a simple arrangement and several more complex "lozenge" reactions⁹² were considered. A reasonably consistent and best fit was obtained for segment (a) with the reaction outlined in the schematics of Figs. 50 and 51. The g.b analysis is summarized in Table 14.

Two other interesting features are found in this region. The first is the large number of very faintly visible parallel lines with contrast similar to a dislocation (Fig. 52, arrow). They have the

TABLE 13

Summary of $g \cdot b$ Analysis, SF2

\underline{g}	\underline{b}	A	B	C	SF	$1/2$	$1/3$	$1/3$	$1/3$
						$\frac{1}{1}$	$\frac{1}{2}$	$\frac{2}{1}$	$\frac{1}{1}$
						0	1	1	1
		Number of images				$g \cdot b$			
$\bar{1}1\bar{1}$		2	2	1	1	-1	-4/3	-2/3	-1/3
$\bar{2}00$		2	0	1	1	-1	2/3	-2/3	-2/3
$11\bar{1}$		0	2w	1	1	0	-2/3	2/3	1/3
$0\bar{2}2$		2	2	0/1*	0	1	2	0	0
$02\bar{2}$		1	1	0	0	-1	-2	0	0
$0\bar{2}0$		1	1	1	1	1	4/3	2/3	-2/3
$2\bar{2}0$		2	1	1	0	2	2	2	0
$\bar{2}20$		2	1	1	0	-2	-2	-2	0
202		1	2	1	w	-1	4/3	2/3	4/3
220		0	1	1	w	0	-2/3	2/3	4/3
$\bar{2}02$		2	0	1	0	-1	0	-2/3	0

* Part of curved line extinct



FIGURE 40. Extended fault 2.



FIGURE 41. Fault 2 invisible.



FIGURE 42. WB, fault 2 invisible.

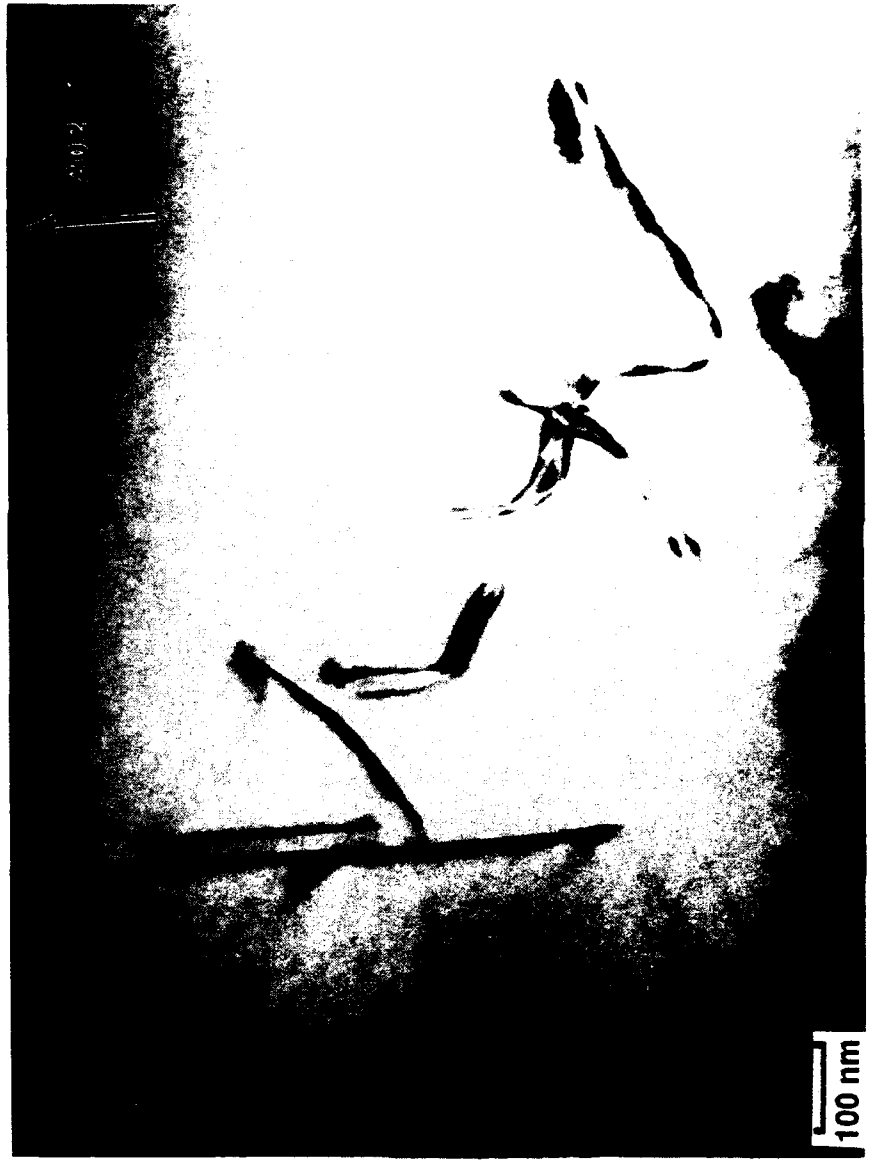


FIGURE 43. One bounding dislocation invisible.



FIGURE 44. The second bounding dislocation invisible.



FIGURE 45. Undissociated superdislocation invisible.

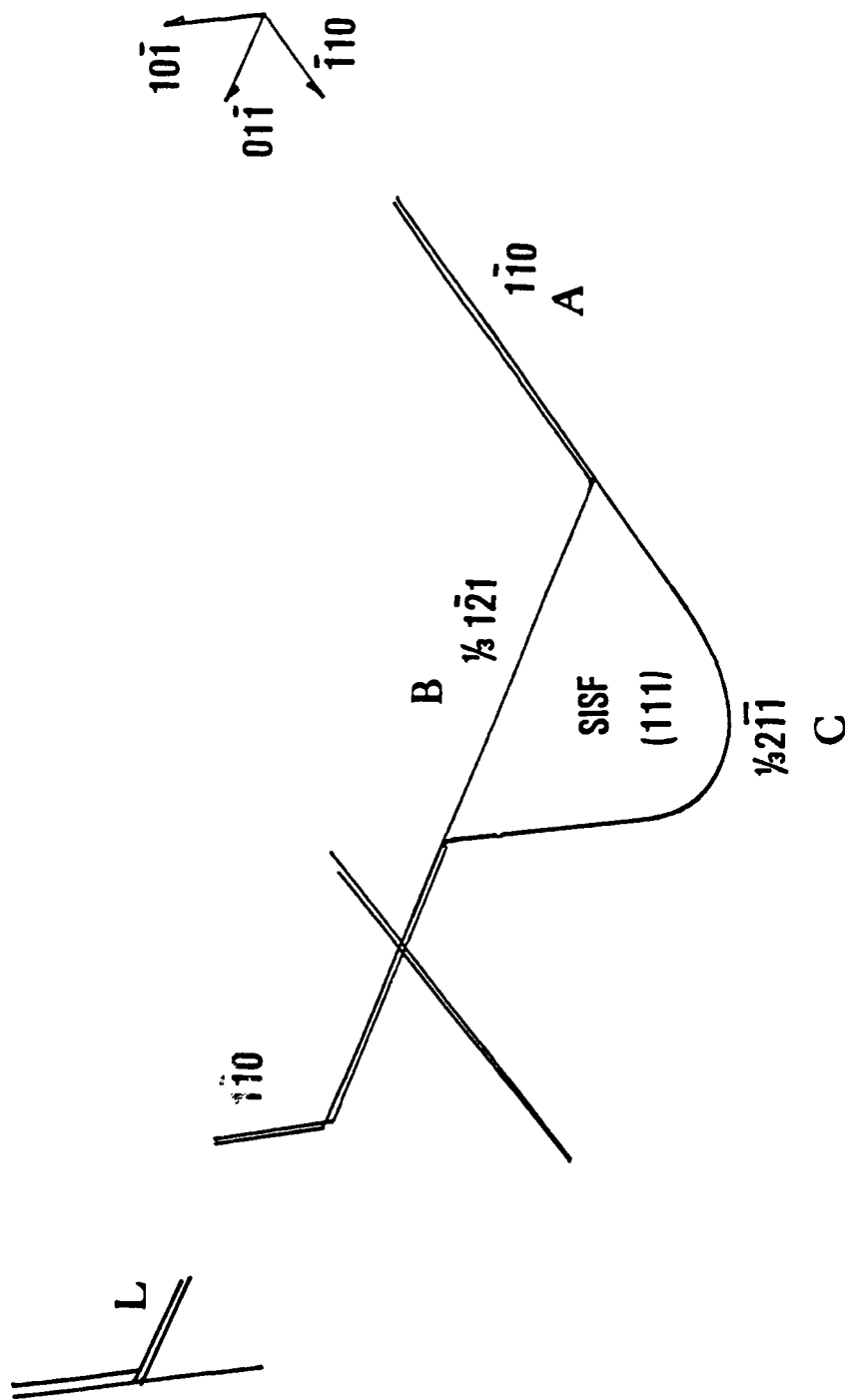


FIGURE 46. Schematic of fault 2 and lozenge (L).

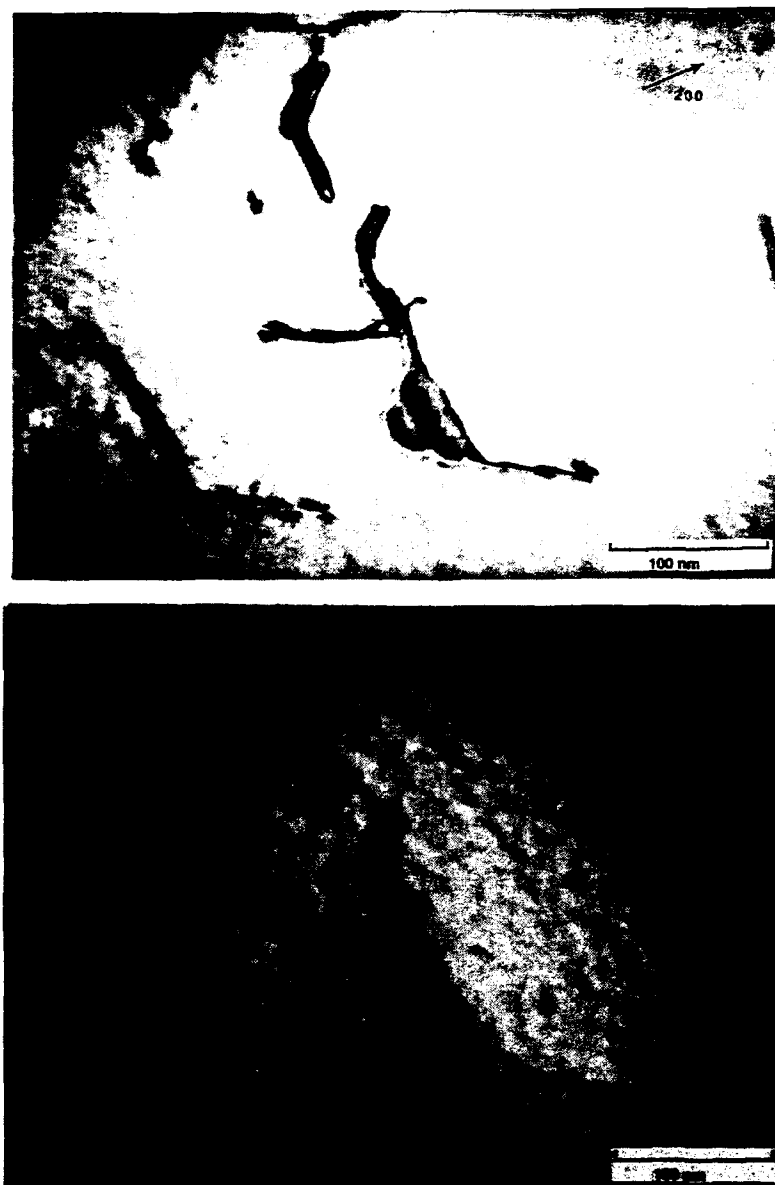


FIGURE 47. +g images of SF2.

TABLE 14

Summary of $\underline{g \cdot b}$ Analysis, Lozenge

	$1/3 100$	$1/3 \bar{1}00$	$1/3 011$	$1/3 0\bar{1}\bar{1}$	PROB. ¹ VISIBLE LINES	PROB. ² VISIBLE LINES	OBSERVED VISIBLE LINES
$1\bar{1}\bar{1}$	1/3	-1/3	0	0	0-2	2	2
200	1	-1	0	0	2	2	2 (4)
$11\bar{1}$	1/3	-1/3	0	0	0-2	2	2
$02\bar{2}$	0	0	0	0	0	0	0
020	0	0	2/3	-2/3	1-2	2	2
$\bar{2}20$	-2/3	2/3	2/3	-2/3	2-4	4	2 (3)
202	2/3	-2/3	2/3	-2/3	2-4	4	2
220	2/3	-2/3	2/3	-2/3	2-4	4	2
$20\bar{2}$	2/3	-2/3	-2/3	2/3	2-4	4	2 (4)
$\bar{2}02$	-2/3	2/3	2/3	-2/3	2-4	4	2 (3)

1. Lower number assumes image extinction for $\underline{g \cdot b} = \pm 1/3, -2/3$.
Higher number same as 2.

2. Assumes all $\underline{g \cdot b} \neq 0$ visible.



FIGURE 48. WB image of lozenge.

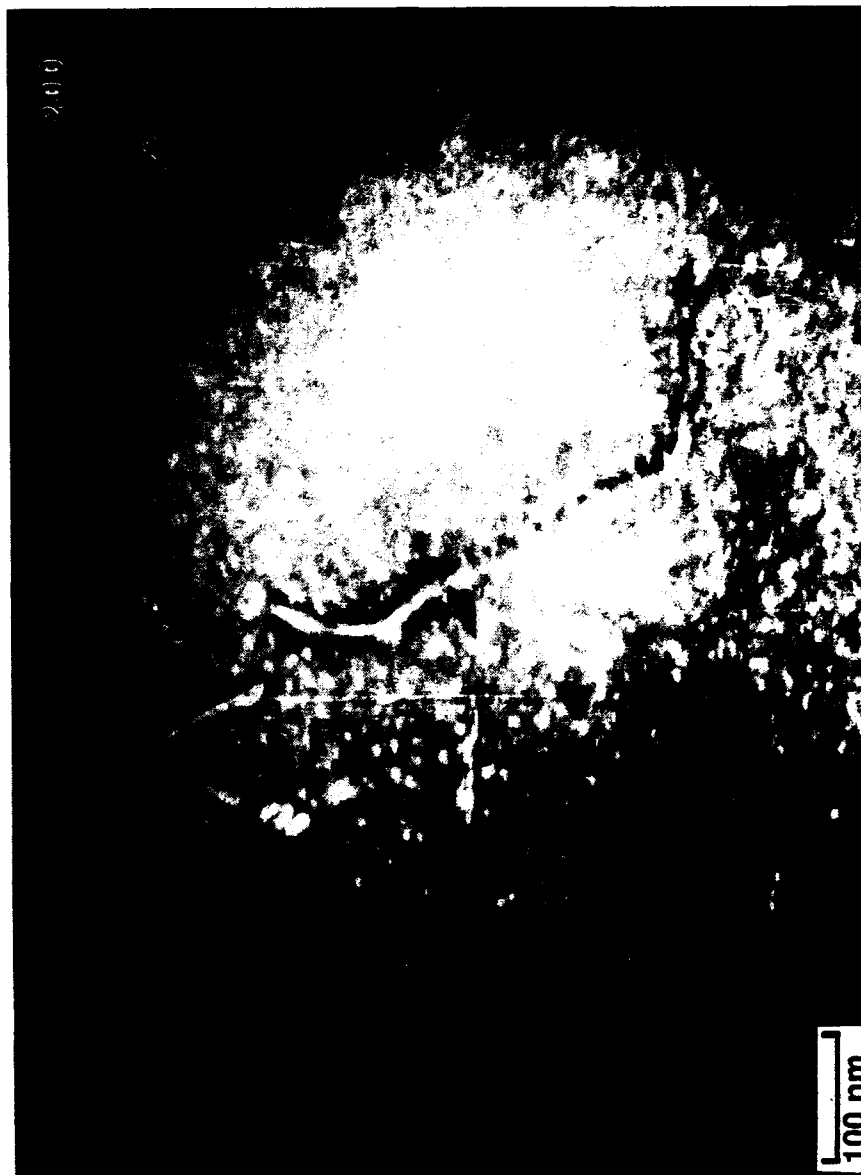


FIGURE 49. WB image of lozenge.

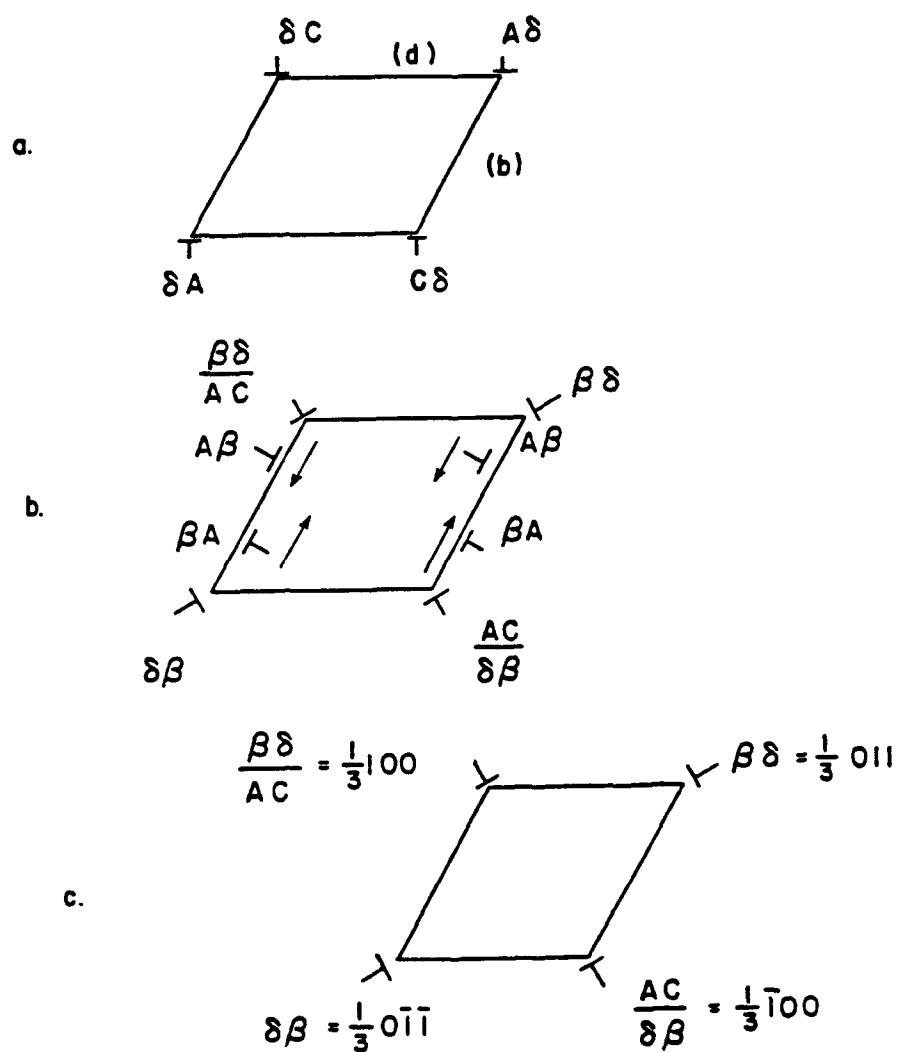


FIGURE 50. Lozenge dissociation of superdipole in Thompson notation.

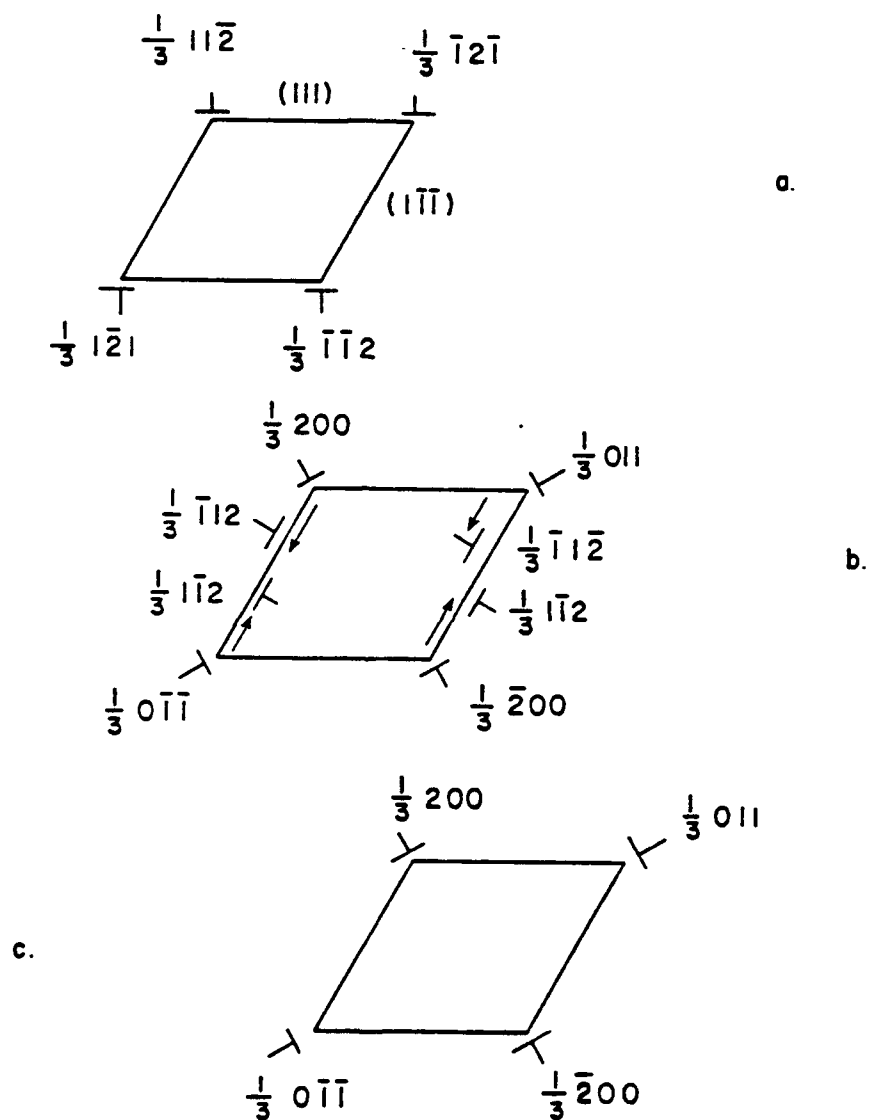


FIGURE 51. Lozenge dissociation of superdipole.

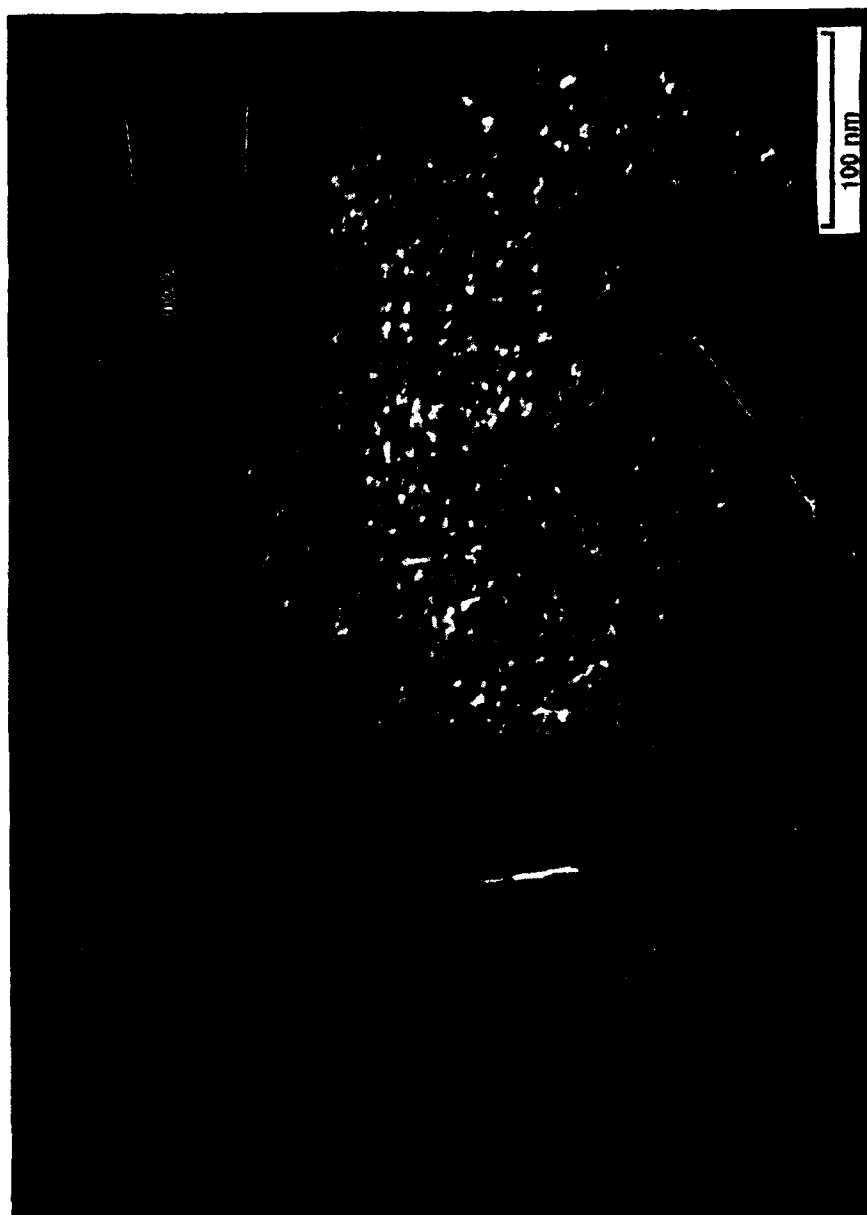


FIGURE 52. Faint dislocation - like contrast in some fundamental reflections (arrow).

appearance of APB tubes⁹³ but are visible in fundamental reflections. The second feature is the faint but visible residual fault contrast in the region of Fig. 53 that would be swept by the undissociated superdislocation segment if it were turned from one edge of the fault to the other. It suggests that the configuration was arrived at by the reverse of that process.

Again, the major features of the extended fault of Fig. 54 and the schematic of Fig. 55 (Ni-24.5Al, $\epsilon = 4\%$, $T = 23^\circ\text{C}$) are quite similar to the first two. The bounding dislocations are clearly visible in Fig. 56 and are out of contrast in turn in Figs. 57 and 58. The g.b analysis is summarized in Table 15. The undissociated superdislocation is $[\bar{1}\bar{1}0]$ in pure screw orientation. The tg pair of Fig. 59 again indicates that it is a single superdislocation. The superpartials bounding the fault are $1/3 [1\bar{2}1]$ and $1/3 [2\bar{1}\bar{1}]$. The fault and all dislocations lie in the (111) plane.

The most dramatic example of extended faults, and the most convincing indication of their potential importance, is that of the grain of Fig. 60. The foil is fortuitously oriented such that in many cases one of the bounding dislocations is present in the foil, and lies in the plane of the foil. The fault passes out of one surface. The bounding dislocations are clearly visible in Figs. 61 and 62. The g.b analysis shows that in the region near center of Figs. 60-62, bounding dislocations are of type $1/3 \langle 112 \rangle$ and the faults are $\langle 111 \rangle$. The numbers of loops and complex interactions indicate substantial motion of dislocations.

In summary, slightly extended stacking fault coupled dislocations are common features in many, but not all grains in binary alloys. Relatively isolated widely extended faults, while not ubiquitous, are certainly not unusual features. The faults analyzed here demonstrate a phenomenon which has not previously been reported. Each of the three configurations consists of a segment which is $\langle 110 \rangle$, apparently composed of $1/2 \langle 110 \rangle$ superpartials, in pure screw orientation, which is decomposed into an extended pair of $1/3 \langle 112 \rangle$ superpartials. Such configurations are clear evidence of conversion from APB coupled to SISF coupled superdislocations. Furthermore, the APB coupled dislocation involved in the reaction is in the commonly observed, presumed locked, screw orientation.

High densities of widely distended faults such as those of Fig. 60 appear to be less common, but indicate considerable mobility. It is possible that when the bounding dislocations lie well out of the plane of the foil and the line length grows short during foil preparation, that sufficient constraints are removed that the faults collapse. None of these features are observed in any composition containing B.

TABLE 15

Summary of $g \cdot b$ Analysis, SF3

\underline{g}	\underline{b}	A	A'	a	C	B	SF	1/2	1/3	1/3	1/3
								$\frac{1}{1}$	$\frac{1}{2}$	$\frac{2}{1}$	$\frac{1}{1}$
								0	1	$\frac{1}{1}$	1
		Number of images						$g \cdot b$			
$\bar{1}\bar{1}\bar{1}$		1	1	2	1	1	1	-1	-4/3	-2/3	-1/3
$1\bar{1}\bar{1}$		1	1	2	1	1	1				
200		1	1	2	1	2	1	1	-2/3	2/3	2/3
$\bar{2}00$		1	1	2	1	2	2	-1	2/3	-2/3	-2/3
$11\bar{1}$		0	0	0	1	1	1	0	-2/3	2/3	1/3
$\bar{1}\bar{1}1$		0	0	0	1	1	1	0	2/3	-2/3	1/3
$0\bar{2}\bar{2}$		1	*	1	1	0	0	1	2	0	0
$02\bar{2}$		1	*	1	1	w	0	-1	-2	0	0
$\bar{2}20$		1	1	2	1	1	0	-2	-2	-2	0
220		0	0	0	1	1	1	0	-2/3	2/3	4/3
$\bar{2}\bar{2}0$		0	0	0	1	1	1	0	2/3	-2/3	4/3
$20\bar{2}$		1	*	2	0	1	0	1	0	2/3	0

* One image, either A or A'



FIGURE 53. Faint residual fault contrast in region bounded by A, B, an imaginary extension of C and the foil surface.



FIGURE 54. Extended fault 3.

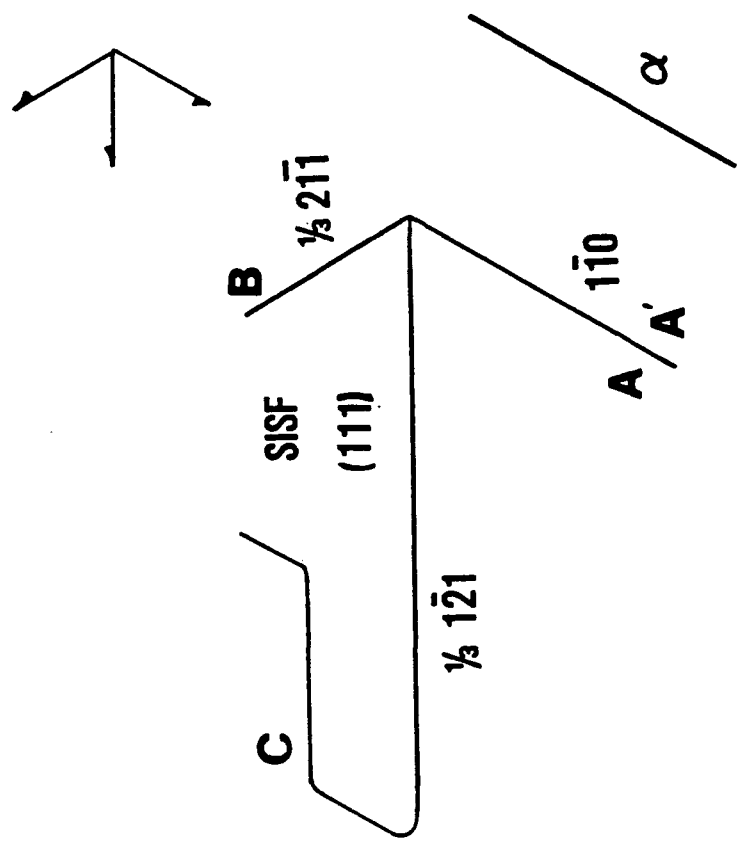


FIGURE 55. Schematic of extended fault 3.

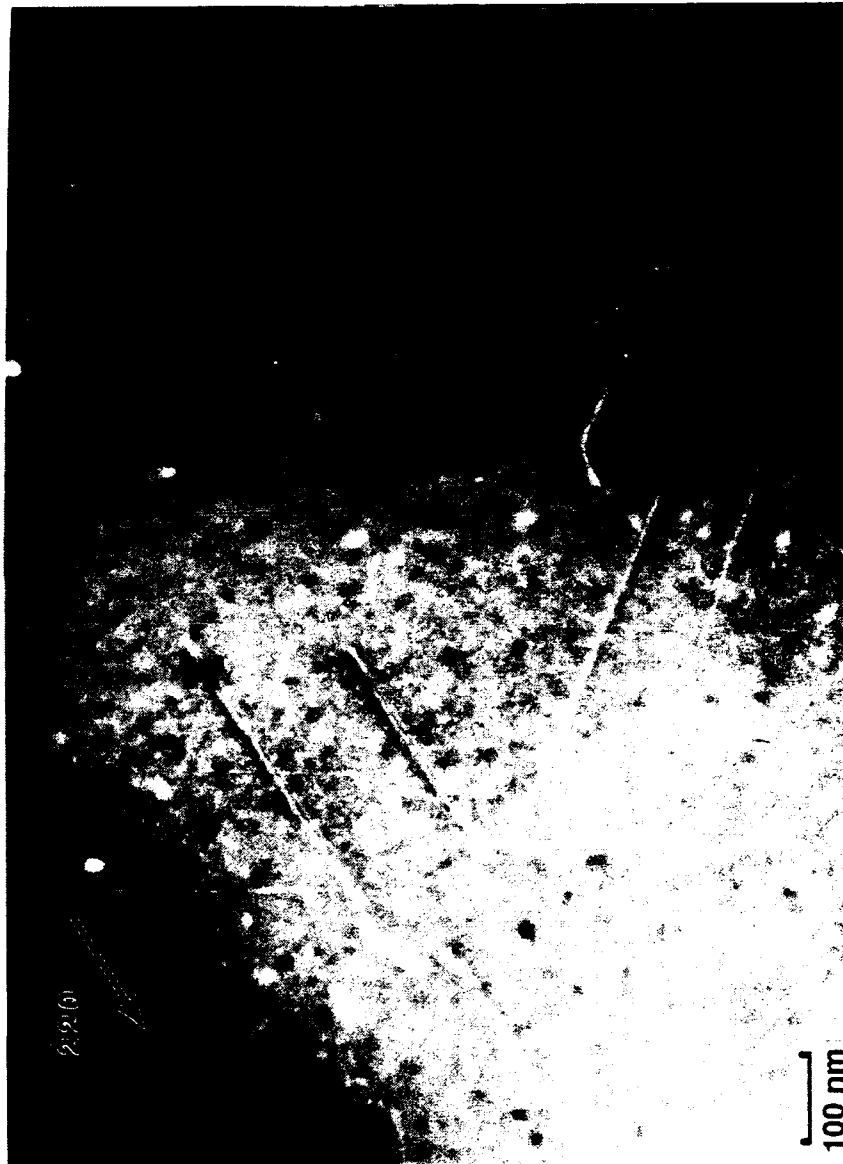


FIGURE 56. WB image, fault invisible.



FIGURE 57. One bounding dislocation invisible.



FIGURE 58. Second bounding dislocation invisible.

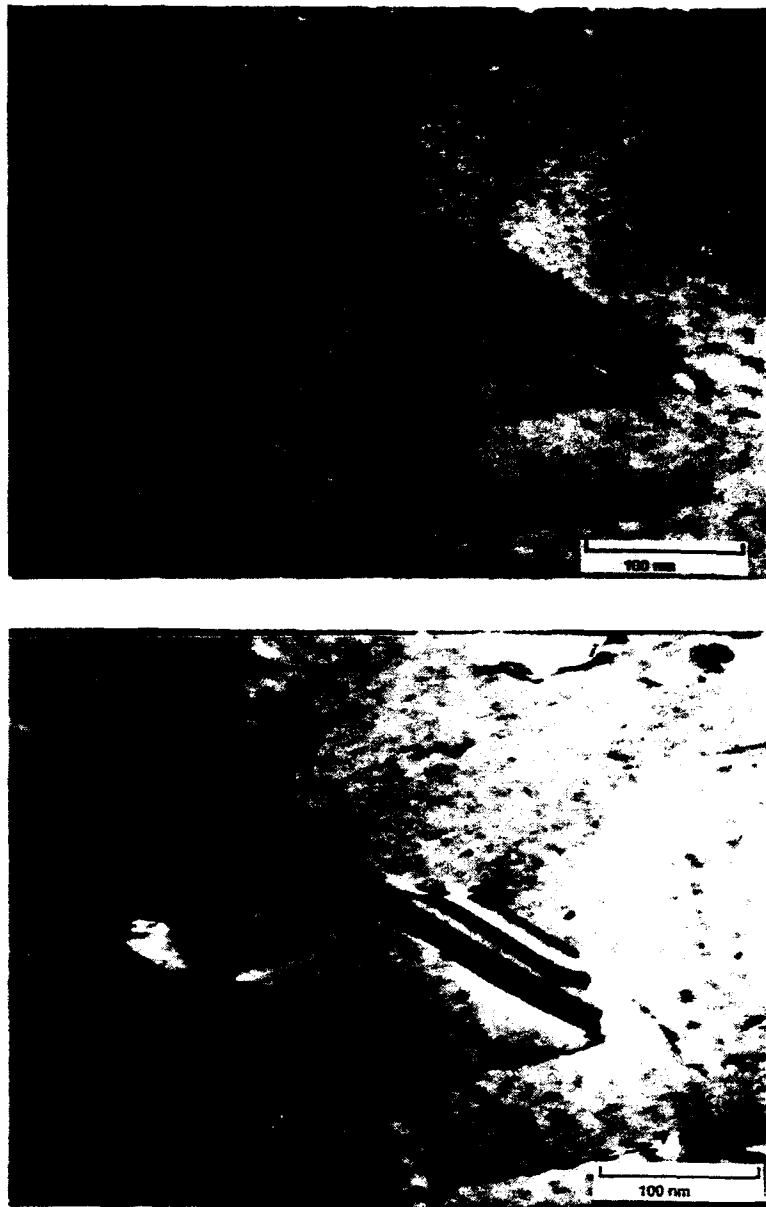


FIGURE 59. $\pm g$ images of SF3.



FIGURE 60. Region of high density of SISFs.



FIGURE 61. Faults and some dislocations invisible.



FIGURE 62. Faults and some dislocations invisible.

CHAPTER VI

DISCUSSION

6.1 Grain Boundary Structure

Briefly summarizing the results: the structures of two boundaries in Ni-24.5 at.% Al were determined. Both boundaries were found to be best described by the CSL solutions for ordered boundary structures. Due to the structures of both boundaries, however, the ordered and disordered solutions are similar and the solutions are not as definitive as they might be. In each case, the agreement between the CSL solutions and the line directions determined by experiment were excellent. In the $\Sigma 9$ case, the spacings are also in excellent agreement. For the $\Sigma 31$ boundary, one of the spacings is in good agreement while the other differs from experiment by a factor of three. In each case, however, the $g \cdot b$ analysis for the boundary dislocations was ambiguous. There is no evidence in either boundary of paired partial grain boundary dislocations.

The poor agreement of the $g \cdot b$ analyses with any likely boundary structure complicates the evaluation of the results with regard to confidence level. In both cases, however, the agreement of the geometrical analyses with experiment is good, which reinforces the implication that there is a systematic problem with Burgers vector

analyses of gbds in Ni_3Al . The strong elastic anisotropy of this material^{80,81} is a possible source for such an effect. The local strains (and image) due to a gbd will depend upon the elastic properties of its surroundings. In the case of a grain boundary in an anisotropic material, the elastic properties will be an infinitely variable function of misorientation and boundary plane. Considered later in this chapter is evidence that the composition of the boundary differs from that of the lattice. If such differences condense somewhat to gbd lines, image characteristics could also be affected by that phenomenon, particularly since the geometry of the adsorption would be affected by elastic anisotropy. With these considerations, the $\Sigma 9(\text{pc})$ and $\Sigma 31(\text{pc})$ solutions are considered the probable structures of the boundaries.

The results indicate then, that at least some grain boundaries have the ordered structure. The matter requires further investigation, however, since it seems possible that some boundaries could be of the ordered and others the disordered structures. In a compound with a very large ordering energy, such as Ni_3Al , it seems evident that some boundaries must be ordered. Consider the $\Sigma = 3$ first order twin. All the atoms in the boundary have the same near neighbor bonds by length and type as in the perfect crystal. The antiphase energy of such a boundary is exactly the APB energy, which is quite large (recall that Ni_3Al is ordered to melting). On the other hand, unless there is a great deal of relaxation and shuffling, a high- Σ boundary will have a large antiphase energy even if the boundary structure is

that of the ordered crystals. This is true because, irrespective of the ordering of the coincident sites, there is a large number of mismatches by type across the boundary between coincident sites. Furthermore, the coincident sites themselves become a negligible fraction of the boundary. If that is the case, and the antiphase energy of the boundary is approximately equal whether the structure is that of the ordered lattice or the disordered lattice, then the structure can be expected to be driven by strain-energy considerations. That is, the disordered structure can be expected. In this scenario then, high symmetry boundaries will be of the ordered structure and low symmetry boundaries will be of the disordered structure.

It is interesting to speculate on the consequences. A decrease in ordering energy would decrease the fraction of ordered boundaries. That is, the disordered structure would extend to lower σ 's. Presumably, slip transmittal and source operation will be more difficult in an ordered-structure boundary than in a disordered-structure boundary of the same type, therefore, the population of transparent (and mobile) boundaries will have changed. In summary, a change in ordering energy, through the addition of B perhaps, will change not only the properties of all boundaries, but will change the distribution of boundary types.

6.2 Surface Energies and Grain Boundary Population

It is evident that boron affects properties in addition to grain boundary cohesion. It was found to have dramatic effects upon the incidence of annealing twins, grain growth, and the occurrence of extended SISF's. SISF separated pairs of dislocations are common in binary alloys, and were never observed in alloys containing 0.5 and 1.0 at.% B. The dramatic decrease in annealing twins and stacking fault coupled dislocations with increasing B content indicates that B has a strong effect in increasing stacking fault energy. The accompanying increase in grain growth kinetics is somewhat more difficult to interpret. There are at least three possibilities: 1. B directly increases the mobility of some or all boundaries. 2. B biases the distribution of boundary types toward more mobile boundaries or, 3. B increases the driving force for grain growth. It is evident that the second is true to some degree, in view of the decrease in twin frequency. This effect is also consistent with the observation that B segregates to higher Σ boundaries more strongly than to $\Sigma 3$ twin boundaries.⁵⁸ If B generally lowers the energy of boundaries and the effect increases with increasing B, it follows that high Σ boundaries will be stabilized to a greater degree. The third possibility seems unlikely since if B decreases boundary energy, the driving force for grain growth will decrease. It seems likely then, that for whatever reason, the population of boundaries in a B containing specimen is more mobile.

This is an interesting observation because it seems apparent that grain boundary mobility and slip transmittal are related. They are both determined in large part by the capacity of the boundary to change orientation, absorb and emit dislocations, and generally alter its structure. If that is true then the population of boundary types in the B containing specimen might be more amenable to slip transmittal. Although this is clearly highly speculative, it seems possible that enhanced ductility could be, in part, a second order effect of the addition of B resulting from a change in the population of grain boundary types.

There is significant circumstantial evidence that B decreases APB energy. The calculations of Cahn and Kikuchi⁹⁵ predict that there is a pronounced maxima in APB energy at the stoichiometric composition and it is now evident from experimental, and other theoretical work that the boundary energy decreases with decreasing Al and that B aids this process.^{55,57-60} Furthermore, the calculations of Briant and Messmer⁴⁵ indicate that B increases Ni-Ni bond strength. The implication is that the ratio of AB to AA and BB bond strength is decreased, decreasing APB energy.

Regardless of the change in absolute magnitudes, the evidence suggests that the ratio of APB to SISF energy decreases with the addition of B, increasing the fraction of APB coupled dislocations. This is suggested also by Baker, et al. who report both SISF and APB coupled dislocations in alloys containing 0.19 and 0.38 at.% B and APB coupled only with 0.75 and 1.12 at.% B.⁹⁰

6.3 Possible Effects of Segregants Upon Slip Transmittal and Grain-Boundary Sources

Transmission of slip from one grain to the other and the role of grain boundaries as sources for lattice dislocations are clearly important aspects of the deformation of polycrystals. It is possible that these are indistinguishable -- that they are two terms for the same event, or that they differ only by the order of occurrence of a sequence of events which is impossible to determine after the fact. Although it is common to represent slip transmittal as a localized event with slip bands in either grain meeting at the boundary [Fig. 63(a)], in the author's experience, it is more common to observe a slip band in one grain but not the other. It seems likely that transmittal may occur by a process which consists of the absorption by the boundary of lattice dislocations from one grain via dissociation into gbd's, and the subsequent emission of lattice dislocations into the second grain by condensation of gbd's at another location [Fig. 63(b)]. Furthermore, the continued operation of a boundary source in one grain requires (or accommodates) deformation of adjoining grains and the boundary. In either case, it is apparent that the ability of the boundary to absorb gbd's either at the site in a step or through motion along the boundary is an important factor. The former might favor localized transmittal while the latter might facilitate "diffuse" transmittal. In the case of diffuse transmittal (and

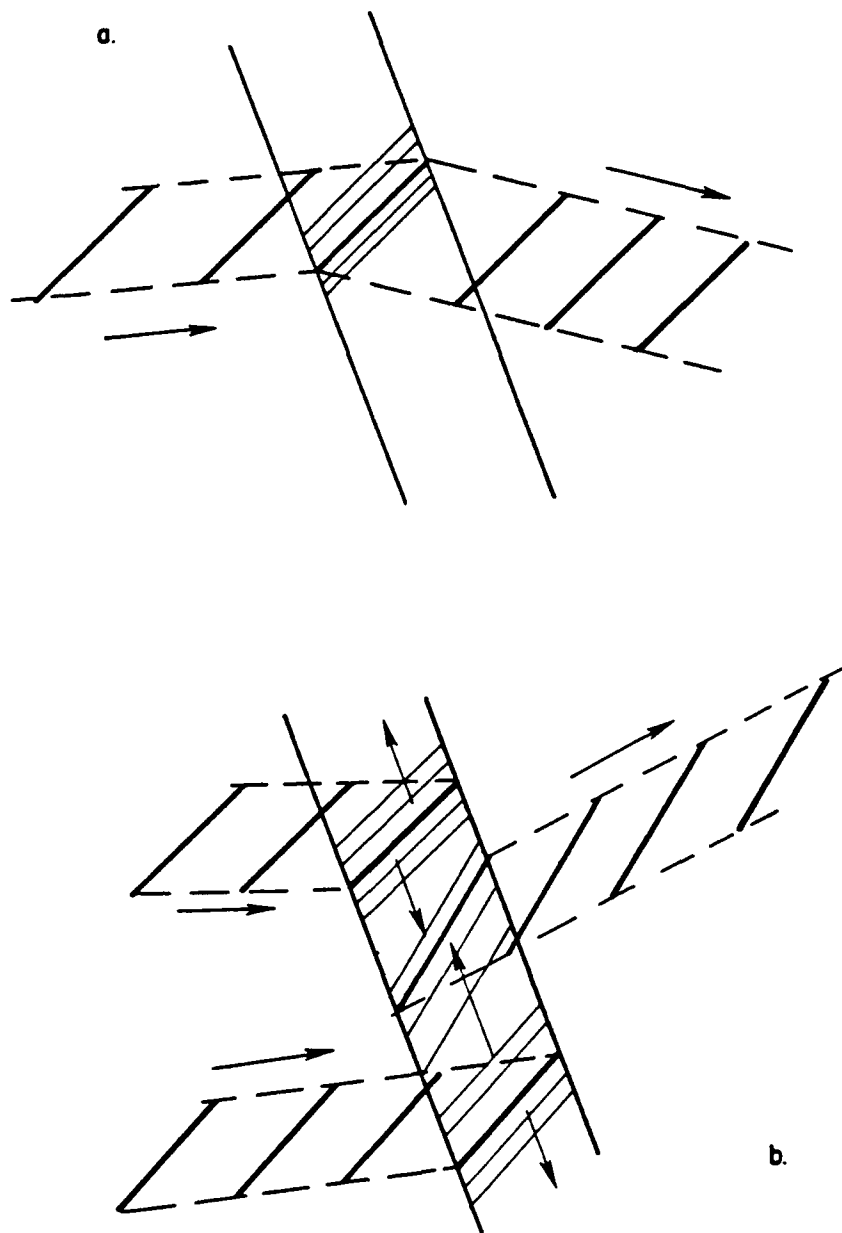


FIGURE 63. Slip transmittal. a) localized. b) diffuse.

possibly that of localized transmittal) absorption and emission are separate events.

It is assumed that emission occurs by the condensation of gbd's into a $1/2 \langle 110 \rangle$ superpartial which moves away from the boundary trailing an APB. The second superpartial is emitted by the same process and "repairs" the APB (Fig. 64). The alternative is that gbd's condense to form the total dislocation which dissociates after leaving the boundary. The latter might be expected if the boundary were composed of DSC vectors of the ordered lattice.

It is apparent that the energy of a boundary of any structure between crystals of an ordered material, will be changed by rearranging atoms by type. Like-atom and dislike-atom interaction energies are significantly different or the crystals would not be ordered. This is particularly evident in the case of low Σ boundaries with high fractions of coincidence sites. In higher Σ boundaries, it is probable that there is at least some contribution of order to the energy. The extreme case is that the boundary structure is characteristic of the ordered lattice. In any event, if order plays a role, then some structures will be favored over others simply due to the effects of ordering. Furthermore, even if the structure of the boundary is that of the disordered lattice, displacements of other than translation vectors of the ordered lattice will have an anti-phase related component of energy. Such a gbd would bound a region of lower AB order and higher energy -- a sort of grain boundary antiphase

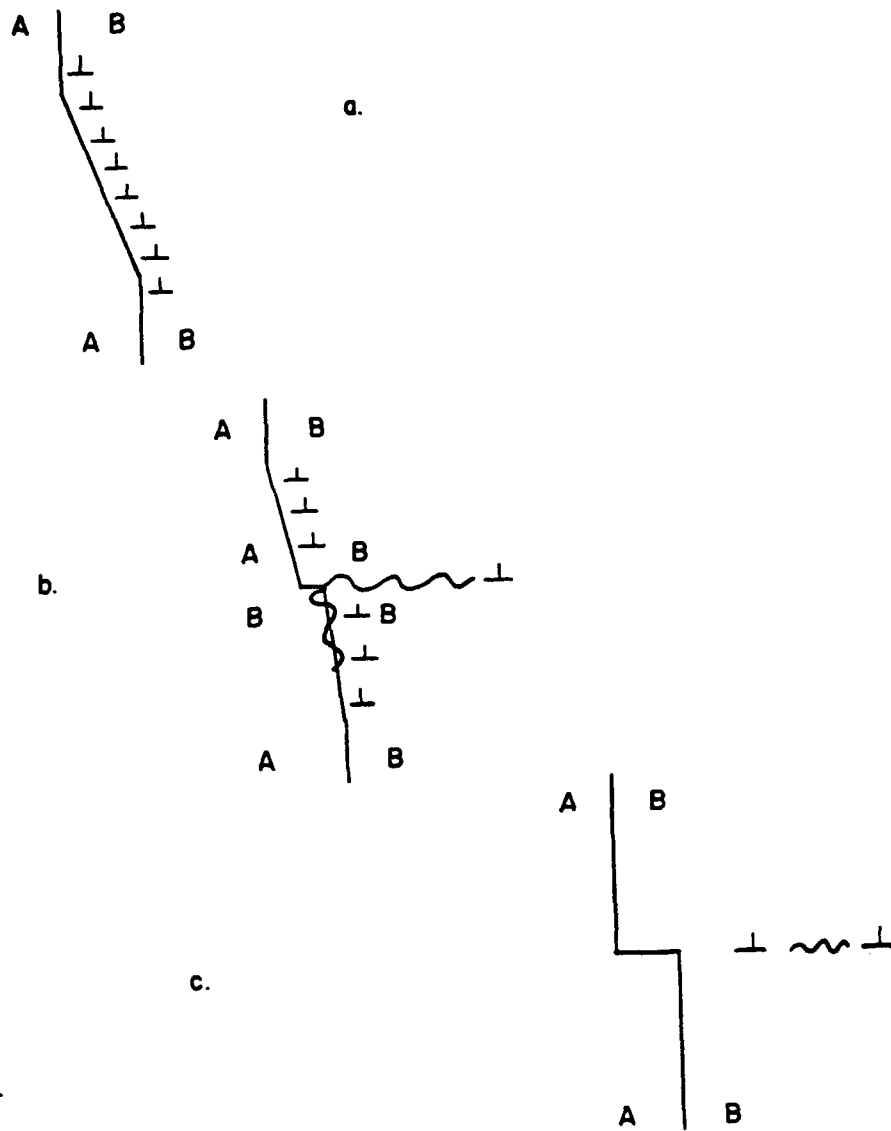


FIGURE 64. Emission of superdislocation.

region (gbapr). This term will be used without implication of a fully ordered boundary.

The gbd's which condense to form the first superpartial dislocation, which is not a translation vector of the ordered lattice or of an ordered boundary, do not themselves constitute a translation vector of an ordered boundary. Therefore, they must leave behind a region of lower AB order (gbapr) in the boundary. The set of gbd's which follow to form the second of the superpartial pair must repair the disorder in the boundary. For clarity, consider the reverse process: absorption of a superdislocation pair in a boundary. Upon absorption of the first superpartial, the boundary is intersected by an apb. If at the intersection AB order is preserved across the gb above the apb and BB anti-order is present across the apb, then BB anti-phase order must be present across the gb below the apb (Fig. 64). The actual location and extent of the misordered region is determined by the nature and location of the gbd's resulting from the absorption event. The absorption of the second superpartial eliminates the APB and probably the gbapr.

Analogous to the splitting of perfect dislocations into Shockley partials, the condensation of gbd's to form a superpartial exchanges a number of small Burgers vectors for one large one. Since the self-energy of a dislocation is proportional to the square of the Burgers vector, energy input is required, and therefore the gbd's mutually repel. They also bound an energetic fault, the gbapr, which results in an attractive force. The expected result then is an equilibrium

separation l_1 determined by the magnitudes of the Burgers vectors and the energy of the gbap, γ_{gbap} . In the schematic representation of Fig. 65, the gbd's are represented by the pair at the extremes of the group.

Similarly, the of gbd's which form the second superpartial sum to a dislocation identical to the first superpartial and repel it. The magnitude of the repulsion depends upon their proximity to the slip plane, l_1 . The formation of the apb causes an attractive force and there results an equilibrium spacing, l_2 , which is dependant upon the energy of the apb, γ_{apb} .

Lower γ_{apb} will allow the first superpartial to move farther away from the boundary and decrease the back-stress on the gbd's thereby decreasing the energy barrier to emission. Conversely, lower γ_{gbap} will increase the spacing between the gbd's, l_1 , and decrease the the distance of the first superpartial from the boundary, l_2 , thereby increasing the barrier to emission. The activation energy then is,

$$Q = Q(\gamma_{apb}, 1/\gamma_{gbap}) \quad 6.1$$

Since the gbd's can be expected to always dissociate to some degree, irrespective of the magnitude of γ_{gbap} , and that at low γ_{gbap} values other factors will control the degree of dissociation, there is not a clear choice of assumptions which will allow a meaningful calculation. It is apparent, however, that in most cases γ_{apb} will dominate. For a significant change in γ_{apb} , lower values will facilitate emission of

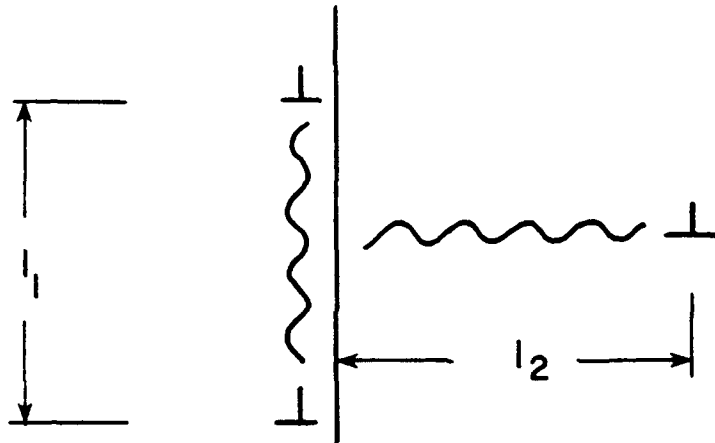


FIGURE 65. Emission of superdislocation.

dislocations. The relevant exception is a case in which γ_{gbpr} is affected far more strongly than γ_{apb} , for instance as the result of strong segregation to grain boundaries of a species which strongly affects the anti-phase surface energies. In such a case increasing anti-phase surface energies might decrease the barrier to emission.

Similar considerations apply to the SISF. Increasing γ_{sisf} can be expected to inhibit emission of $1/3 \langle 112 \rangle$ dislocations. If B in fact decreases APB energy and increases SISF energy, the barrier to emission of APB coupled dislocations will have decreased while the barrier to the emission of SISF coupled dislocations will have increased. This is consistent with the observations of Chapter V.

6.4 The Role of SISF Coupled Dislocations

Probably the most significant finding of the study on lattice dislocations is the observation of the conversion of $1/2 [110]$ superpartials to $1/3 [112]$ superpartials. An important aspect is that the APB coupled $\langle 110 \rangle$ superdislocation involved in the process is in the ubiquitous straight screw orientation. This observation is then proof of a connection between the two most prominent artifacts of deformation. Furthermore, it appears to be a relatively common event.

A related issue is the identification of APB and SISF coupled dislocations. When the stacking fault energy is sufficiently high and the spacing small enough that the strain fields overlap substantially, the strain field, and the image, will tend toward that of the total

dislocation, i.e., $\langle 110 \rangle$. It is probable that if the image does not resolve the pair (due to diffraction image limitations) the image is due to the total strain field and will represent the total dislocation. It follows that SISF and APB coupled pairs will be indistinguishable. Since this is often the case in bright field images, and it appears that commonly in the literature pairs are assumed to be APB coupled if there is no apparent SISF, it is possible that they are sometimes misidentified. In the present work, images such as the weak-beam micrograph of Fig. 45 in which the resolution is clearly sufficient to resolve the individual superpartials seem to preclude that possibility.

One possible mechanism for the formation of the observed configurations is that the SISF coupled superdislocation is a result of the Kear-Wilford (KW) locking mechanism. As in Fig. 66(a), the leading superpartial has cross-slipped and locked by dissociating on a different $\{111\}$ plane. Under sufficient stress, rather than creating APB, the $1/2 [\bar{1}01]$ superpartial dissociates into a $1/3 [\bar{2}11]$ superpartial and a $1/6 [1\bar{2}1]$ stair-rod [Fig. 66(b)]. Another possibility is that the formation of the $1/3 \langle 112 \rangle$ plays an active role in the locking mechanism as follows: The leading $1/2 [\bar{1}01]$ constricts, cross-slips onto $\{001\}$, then dissociates directly into the stair-rod and $1/3 [\bar{2}11]$. The $1/3 [\bar{2}11]$ is incapable of cross-slipping on $\{001\}$ and the stair-rod is a barrier to the cross-slip of the trailing superpartial.

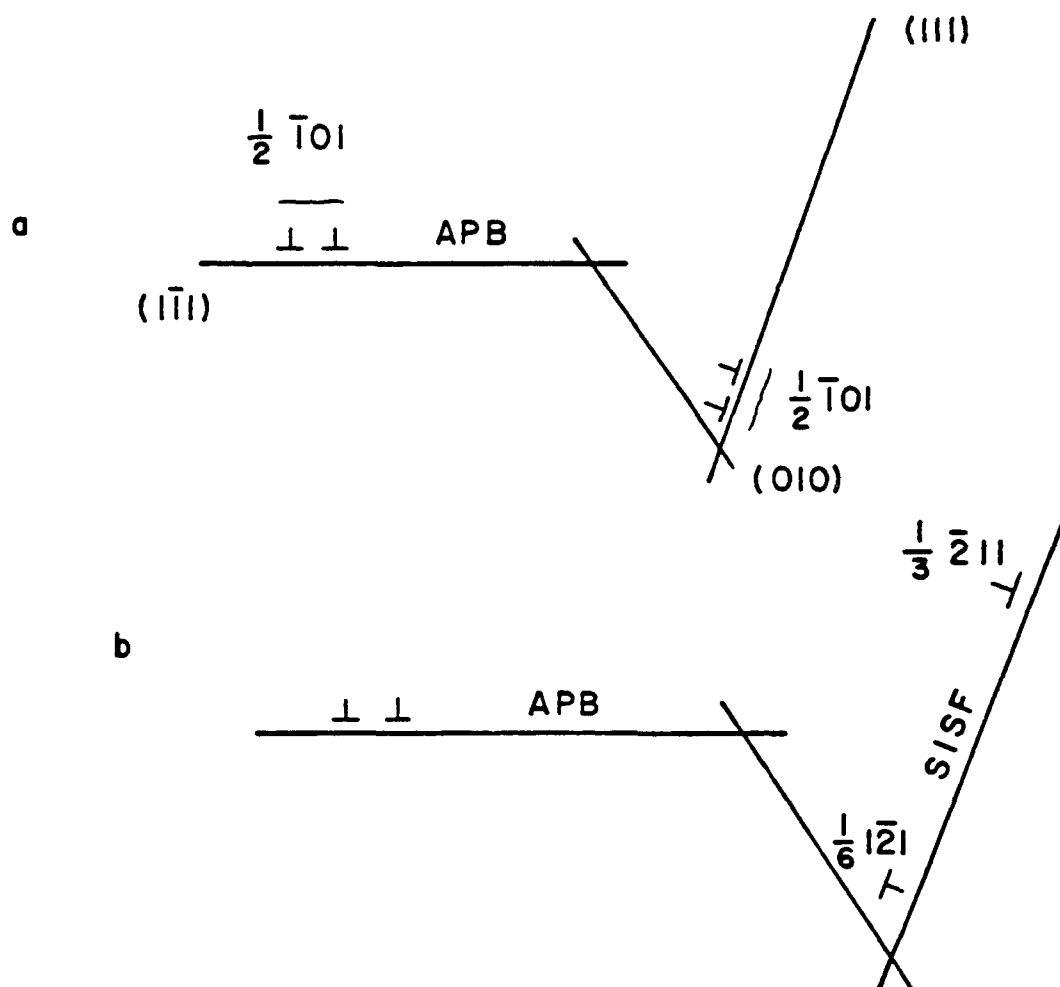


FIGURE 66. Kear-Wilks lock as source of SISF, $\frac{1}{3} (112)$ superdislocation.

The complex lozenge interaction was also found to result from the presence of SISF coupled pairs. The lozenge is the consequence of interaction of a superdislocation dipole composed of $1/3 \langle 112 \rangle$ partials and driven by a reduction in strain energy. Such an interaction constitutes a variety of Kear-Wiltsdorf type, cross-slip locking mechanism, but does not appear to be a common feature.

A thick region of foil provided evidence of profuse slip of $1/3 \langle 112 \rangle$ superpartials trailing SISF's. There is ample evidence of interaction and resulting debris. Since this specimen was unusual in this respect, the dislocation remnants may be an artifact of forging and not of general importance. However, it is evident that $1/3 \langle 112 \rangle$ dislocations are mobile under some circumstances.

The existence and role of SISF coupled dislocations has been largely ignored or discounted, and in fact, the contribution may be insignificant. Nonetheless, whether they are mobile, or simply artifacts of the motion of APB coupled dislocations, they are a prominent feature in binary alloys and are absent (in extended form, at least) in B containing alloys. That such a change in either dominant slip system or debris should have no effect seems remarkable.

Isolated examples of the tube-like features of Fig. 52 have also been observed by Veyssiere⁸³ who has noted the resemblance to APB tubes and has been perplexed by the fact that they image in fundamental reflections but not in superlattice reflections. APB tubes have also been reported in Ni_3Al , although without micrographs.⁹³ SISF tubes equivalent to the APB tube is the lozenge fault of Chapter

V and requires stair-rod dislocations at the plane intersections. Hirth has suggested that they are APB tubes and that the contrast is the result of a chemical effect, specifically the deviation in composition discussed earlier.⁹⁴

CHAPTER VII

CONCLUSIONS

The structures of both a Σ 9 and a Σ 31 boundary in Ni_3Al were found to consist of perfect grain boundary dislocations of the ordered L1_2 structure. There was no evidence of grouped partial grain boundary dislocations. This is taken to imply that boundary structures are ordered at least for $\Sigma \leq 31$. It is possible that higher Σ , lower symmetry boundaries are of different structure.

Boron was observed to have strong effects upon the population of boundary types, grain size, and grain growth. The combined effects of the alteration of boundary type distributions and the possible existence of ordered and disordered structure boundaries have the potential for strongly altering average boundary behavior. In addition, small amounts of B completely eliminate widely extended stacking faults. It is evident that B effects other than simply boundary cohesion are important.

Independent reaction of APB coupled $1/2$ $[110]$ pairs to $1/3$ $[112]$ SISF coupled pairs (or the reverse) has been conclusively demonstrated. The $1/2$ $[110]$ participants were in the commonly observed pure screw orientation which is attributed to a locking mechanism. It is probable that SISF coupled superdislocations play a far more

prominent role in deformation behavior than generally appreciated either through a direct role in, or as a consequence of the Kear-Wilsdorf lock.

REFERENCES

1. A. H. Cottrell, Relations of Properties to Microstructure, ASM, Am. Soc. Metals, Cleveland, OH (1954).
2. M. J. Marcinkowski, N. Brown, and R. M. Fisher, *Acta Metall.* 9, 129 (1961).
3. T. L. Johnston, R. G. Davies, and N. S. Stoloff, *Phil. Mag.* 12, 305 (1965).
4. B. H. Kear and M. F. Hornbecker, *Trans Am. Soc. Metals*, 59 155 (1966).
5. B. A. Kear, A. F. Giamei, S. M. Silcock, and R. K. Ham, *Scripta Metall.* 2, 287 (1968).
6. B. H. Kear, G. R. Leverant, and J. M. Oblak, *Trans. ASM*, 62, 639 (1969).
7. M. J. Marcinkowski and N. Brown, *Acta Metall.* 9, 764 (1961).
8. M. G. Mendiratta, S. K. Ehlers, D. K. Chatterjee, and H. A. Lipsitt, *Metall. Trans. A*, 18A, 283 (1987).
9. D. McLean, Grain Boundaries in Metals, Oxford University Press, London 1957.
10. S. Amelinckx and W. Dekeyser, *Sol. St. Phys*, 8, 325 (1959).
11. J. P. Hirth and J. Lothe, Theory of Dislocations, Wiley, NY 1982.
12. B. A. Bilby, R. Ballough, and E. Smith, *Proc. Roy. Soc.* A231, 263 (1955).
13. J. P. Hirth, *Metall. Trans.* 3, 3074 (1972).
14. J. P. Hirth, *Acta Metall.* 22, 1023 (1974).
15. A. R. Kinsman and H. I. Aaronson, *Acta Metall.* 7, 361 (1974).
16. W. Bollmann, Crystal Defects and Crystalline Interfaces, Springer-Verlag, Heidelberg 1970.
17. S. Ranganathan, *Acta Cryst.* 21, 197 (1966).
18. H. Grimmer, W. Bollmann, D. H. Warrington, *Acta Cryst.* A30, 197 (1974).

19. D. A. Smith and R. C. Pond, *Int. Met. Rev.* 205, 61 (1976).
20. R. Bonnet and E. Cousineau, *Acta Cryst.* A33, 850 (1977).
21. R. C. Pond and W. Bollmann, *Phil. Trans. R. London Sci. A*, 292 449 (1979).
22. A. Brokman and R. W. Balluffi, *Acta Metall.*, 29 1703 (1981).
23. H. Grimmer, *Acta Cryst.*, A40, 108 (1984).
24. W. A. T. Clark and D. A. Smith, *Phil. Mag. A*, 38, 376 (1978).
25. L. K. France and M. H. Loretto, *Proc. Royal Soc. A*, 307, 83 (1968).
26. R. C. Pond and D. A. Smith, *Phil. Mag.*, 36, 353 (1977).
27. W. A. T. Clark and D. A. Smith, *J. Mater. Sci.* 14, 776 (1979).
28. S. L. Sass, *J. Appl. Cryst.* 13, 109 (1980).
29. D. A. Smith, V. Vitek, and R. C. Pond, *Acta Metall.* 25, 475 (1977).
30. R. C. Pond and V. Vitek, *Proc. Roy. Soc. A* 357, 453 (1977).
31. V. Vitek, A. P. Sutton, Gui Jin Wang, and D. Schwartz, *Scripta Metall.* 17 183 (1983).
32. A. P. Sutton, D. A. Smith, and V. Vitek, *J. Microsc.* 116, 97 (1979).
33. D. A. Smith, V. Vitek, and R. C. Pond, *Acta Metall.* 25, 475 (1977).
34. A. P. Sutton, M.Sc. Thesis, Oxford University (1978).
35. A. P. Sutton, R. W. Balluffi, and V. Vitek, *Scripta Metall.* 15, 989 (1981).
36. Gui Jin Wang, A. P. Sutton, and V. Vitek, *Acta Metall.* 32, 1093 (1984).
37. V. Paidar, *Scripta Metall.* 20, 1227 (1986).
38. C. Lall, S. Chin, and D. P. Pope, *Metall. Trans. A*, 10A, 1323 (1979).

39. E. M. Grala, Mechanical Properties of Intermetallic Compounds, ed. J. H. Westbrook, John Wiley and Sons, Inc., NY, 1967, p. 491.
40. K. Aoki and O. Izumi, *Trans. Jap. Inst. Met.* 19, 203 (1978).
41. K. Aoki and O. Izumi, *Trans. Jap. Inst. Met.* 43, 1190 (1979).
42. C. T. Liu and C. L. White, *Proc. Symp. High Temperature Ordered Intermetallic Alloys*, 365 (1985).
43. R. J. Kerans, *Metall. Trans. A*, 15A, 1721 (1984).
44. I. Baker, E. M. Schulson, and J. A. Horton, *Acta Metall.* 35, 1533 (1987).
45. C. L. Briant and R. P. Messmer, *Phil. Mag.* B42, 569 (1980).
46. S. Wakayama, M. Hashimoto, Y. Ishida, R. Yamamoto, and U. Doyama, *Acta Metall.* 32, 21 (1984).
47. M. Hashimoto, Y. Ishida, S. Wakayama, R. Yamamoto, M. Doyama, and T. Fujiwara, *Acta Metall.* 32, 13 (1984).
48. M. Hashimoto, Y. Ishida, R. Yamamoto, and M. Doyama, *Acta Metall.* 32, 1 (1984).
49. T. Ogura, S. Hauada, T. Masumoto, and O. Sgami, *Met. Trans. A*, 16A, 441 (1985).
50. A. Choudhury, C. L. White, and C. R. Brooks, *Scripta Metall.* 20, 1061 (1986).
51. S. A. Horton and M. K. Miller, *Acta Metall.* 35, 133 (1987).
52. W. A. T. Clark and R. C. Pond, *Scripta Metall.*, 20, 1177 (1986).
53. Y. Ishida and M. McLean, *Phil. Mag.* 27, 1125 (1973).
54. T. Takasugi and O. Izumi, *Acta Metall.* 31, 1187 (1983).
55. S. P. Chen, A. F. Voter, and D. J. Srolovitz, *Mat. Res. Soc. Symp. Proc.* 81, 45 (1987).
56. A. H. King and M. H. Yoo, *Mater. Res. Soc. Symp.* 81, 99 (1987).
57. S. M. Foiles, *Mat. Res. Soc. Symp. Proc.* 81, 51 (1987).

58. M. K. Miller and J. A. Horton, *Scripta Metall.* 30, 789 (1986).
59. D. D. Sieloff, S. S. Brenner, and M. G. Burke, *Mat. Res. Soc. Symp. Proc.* 81, 87 (1987).
60. I. Baker and E. M. Schulson, *Phil. Mag. B*, 57, 379 (1988).
61. W. A. T. Clark, Ph.D. Thesis, Oxford University (1976).
62. H. Mykura, Grain Boundary Structure And Kinetics, *Am. Soc. Metals. Symp. Proc.* p. 445 (1979).
63. M. B. Boisen and G. V. Gibbs, Mathematical Crystallography, *Rev. in Minerology*, 15 (1985).
64. C. T. Young, J. H. Steele, and J. L. Lytton, *Metall. Trans.* 4, 2081 (1973).
65. P. Heilman, W. A. T. Clark, and D. A. Rigney, *Ultramicroscopy*, 9, 365 (1982).
66. D. P. Pope and S. S. Ezz, *Int. Metals Rev.* 29, 136 (1984).
67. P. H. Thornton, R. G. Davies, and T. L. Johnston, *Met. Trans. A*, 1A, 207 (1970).
68. S. M. Copley and B. H. Kear, *Trans TMS-AIME*, 239, 977 (1967).
69. S. Takeuchi and E. Kuramoto, *Acta Metall.* 21, 415 (1973).
70. Y. Umakoski, D. P. Pope, and V. Vitek, *Acta Metall.* 32, 449 (1984).
71. P. N. Flinn, *Trans. Metal. Soc. AIME*, 218, 145 (1960).
72. J. A. Horton and C. T. Liu, *Acta Metall.* 33, 1191 (1985).
73. B. H. Kear and H. G. F. Wilsdorf, *Trans. Met. Soc. AIME* 224, 382 (1962).
74. R. G. Davies and N. S. Stoloff, *Phil. Mag.* 12 297 (1965).
75. M. Yamaguchi, V. Paidar, D. P. Pope, and V. Vitek, *Phil. Mag.* 45, 867 (1982).
76. V. Paidar, M. Yamaguchi, D. P. Pope, and V. Vitek, *Phil. Mag.* 45, 883 (1982).

77. G. Tichy, V. Vitek, and D. P. Pope, *Phil. Mag. A*, 53, 467 (1986).
78. G. Tichy, V. Vitek, and D. P. Pope, *Phil. Mag. A*, 53 485 (1986).
79. V. Paidar, D. P. Pope, and V. Vitek, *Acta Metall*, 32, 435 (1984).
80. M. H. Yoo, *Scripta Metall.* 20, 915 (1986).
81. M. H. Yoo, *Mater. Res. Soc. Symp. Proc.* 81, 207 (1987)
82. P. Veyssiere, D. L. Gann, and S. Rabier, *Phil. Mag.* A49, 45 (1984).
83. P. Veyssiere, *Phil. Mag.* A50, 189 (1984).
84. V. Paidar, *Acta Metall.* 33 1803 (1985).
85. P. Veyssiere, J. A. Horton, M. H. Yoo, and C. T. Liu, *Phil. Mag. Lett.*, 57, 17 (1988).
86. H. R. Pak, T. Saburi, and S. Nenno, *Scripta Metall.* 10, 1981 (1976).
87. W. Yau, I. P. Jones, and R. E. Smallman, *Scripta Metall.* 21, 1511 (1987).
88. I. Baker and E. M. Schulson, *Phys. Status Solidi A*, 85, 481 (1984).
89. I. Baker and E. M. Schulson, *Phys. Status Solidi A*, 89, 163 (1985).
90. I. Baker, B. Huaug, and E. M. Schulson, *Acta Metall.* 36, 493 (1988).
91. W. Yan, I. P. Jones, and R. E. Smallman, *Scripta Metall.* 21, 1511, (1987).
92. J. P. Hirth and J. Lothe, *Theory of Dislocations*, Wiley, NY, 1982, p.344.
93. P. M. Hazeldine and P. B. Hirsch, *Mater. Res. Soc. Symp. Proc.* 81, 75 (1987).
94. J. W. Cahn and R. Kikuchi, *J. Phys. Chem. Solids*, 20, 94 (1961).
95. J. P. Hirth, Private Communication.